Phonon and electron excitations in diatom abstraction from metallic surfaces

Oihana Galparsoro Larraza

THÈSE EN COTUTELLE PRÉSENTÉE

POUR OBTENIR LE GRADE DE

DOCTEUR DE

L'UNIVERSITÉ DE BORDEAUX

ET DE L'UNIVERSITÉ DU PAYS BASQUE

ÉCOLE DOCTORALE UBX

ÉCOLE DOCTORALE DU PARTENAIRE

SPÉCIALITÉ : Chimie-Physique

Par Oihana GALPARSORO LARRAZA

PHONON AND ELECTRON EXCITATIONS IN DIATOM ABSTRACTION FROM METALLIC SURFACES

Sous la direction de Pascal LARREGARAY
et de Maite ALDUCIN

Soutenue le 14 de décembre

Membres du jury :

M. KROES, Geert-Jan	Professeur, Leiden University	Président
M. GAMALLO, Pablo	Professeur, Universidad de Barcelona	rapporteur
M. RUBAYO-SONEIRA, Jesus	Professeur, InSTEC	rapporteur
M. DIEZ-MUIÑO, Ricardo	Chercheur au CSIC, UPV/EHU	Examinateur
Mme. DIAZ, Cristina	Ramon y Cajal Research Fellow, Universidad Autonoma de Madrid	Examinateur
M. PONS, Bernard	Professeur, Université de Bordeaux	Examinateur
M. LARREGARAY, Pascal	Directeur de Recherche au CNRS, Université de Bordeaux	Directeur de thèse
Mme. ALDUCIN, Maite	Chercheur au CSIC, UPV/EHU	Directrice de thèse

Titre : *Excitations électroniques et phononiques au cours de réaction d'abstraction diatomiques de surfaces métalliques*

Résumé: La rationalisation des processus chimiques élémentaires aux surfaces est d'intérêt primordial pour de nombreux phénomènes naturels ou d'intérêt technologique. D'un point de vue fondamental, la façon dont l'énergie, concomitante à toute réaction chimique, est distribuée parmi les degrés de liberté des molécules formées et/ou transférée à la surface est loin d'être systématisée. Dans ce travail, des simulations, reposant sur la méthode des trajectoires quasi-classiques (QCT), sont réalisées pour examiner cette problématique lors de recombinaisons de molécules d'hydrogène (H2) et d'azote (N2) résultant de l'abstraction d'atomes adsorbés via collision par un atome provenant de la phase gazeuse sur des surfaces de Tungstène - W(100) et W(110) - à taux de couverture non nul. Ces processus sont ici étudiés pour leur intérêt en physique des interactions plasma-paroi. Des surfaces d'énergie potentielle, construites à partir de calculs de structure électronique basés sur la théorie de la fonctionnelle densité (DFT), sont utilisées pour simuler, dans le cadre de la mécanique classique - incluant les corrections semi-classiques pertinentes - les processus ultrarapides dit de "Eley-Rideal" et par "atomes-chauds" (sub-picoseconde). La mise en place de modèle effectifs, pour tenir compte de la dissipation de l'énergie aux phonons de la surface et aux excitations électroniques (paires électron-trou), permet de rationaliser la dynamique non-adiabatique de l'abstraction atomique aux surfaces métalliques.

Mots clés : Simulations de dynamique quasi-classique, recombinaison Eley-Rideal et « atomes chauds », Excitations électroniques et phononiques, azote, hydrogène, tungstène, interface gaz-solide.

Title : Phonon and electron excitations in diatom abstraction from metallic surfaces

Abstract: The rationalization of elementary processes at surfaces is of prime importance for numerous natural and technological areas. From a fundamental point of view, the way the energy concomitant to any chemical reaction is distributed among the desorbing molecules degrees-of-freedom and the surface is far from being fully pictured. In this work, quasiclassical molecular dynamics (QCT) simulations have been carried out to investigate this issue for the recombination of H2 and N2 resulting from atomic adsorbate abstraction by atom scattering off the W(100) and W(110) covered surfaces, these processes being of relevance in plasma-wall interactions. Potential energy surfaces, built from density functional (DFT) theory calculations, have been used to simulate, within the framework of classical dynamics (including semi-classical corrections), the subpicosecond Eley-Rideal and Hot-Atom processes. The implementation of effective models to account for energy dissipation to surface phonons and electron-hole pair excitations, have

allowed to rationalize the non-adidabatic dynamics of atom abstraction at metal surfaces.

Keywords : Quasiclassical dynamics simulations, Eley-Rideal and Hot-Atom recombination, energy dissipation, phonon and electron excitations, nitrogen, hydrogen, tungsten, gas-solid interface

---

Unité de recherche

Institut des Sciences Moléculaires – Université de Bordeaux CNRS UMR 5255

Bâtiment A12, 351 cours de la libération

33405 TALENCE cedex

FRANCE

Gertukoei, bihotz-bihotzez

Chapter I

Introduction

Heterogeneous elementary processes at the gas-solid interface are intensively studied [1] due to their important role in many domains. Nowadays, 90% of the industrial chemical processes involve a heterogeneous catalytic reaction [2,3], as for instance, petrol refining, synthesis of chemical products, fabrication of fibers and plastics or the treatment of combustion products in motor vehicles [4–6]. An important example is the synthesis of ammonia. In this reaction the dissociation of N_2 molecules is the limiting step. G. Ertl, who elucidate the mechanism for this dissociative reaction, was laureated with a Nobel price in Chemistry in 2007, due to the ensemble of studies he performed about chemical processes on solid surfaces. Besides, in order to understand reactions of interest for atmospheric chemistry [7] and in the interstellar media [8–10], to get a precise description of the heterogeneous reactive mechanisms at the molecular level is mandatory. The chemical reactivity at the gas-solid interface is also of interest for the atmospheric entry of spatial vehicles, as it can contribute up to 30% of the heat flux that goes through the wall of the vehicle [11, 12]. Moreover, the description of plasma-wall interactions is an important issue within the international project to design and build an experimental fusion reactor (ITER) [13], which will be (if as predicted, in 2025) the world's largest performed magnetic confinement plasma physics experiment. And more important, it will be the first fusion device to produce net energy.

The interaction of atoms and molecules with surfaces can be influenced by a large number of physical parameters such as surface temperature, the presence of adsorbed impurities, local defects, the energy available to the impinging molecule as well as the incident angle. Thus, a theoretical dynamical approach is required to catch the essential physics of the problem. As the issue is complex, acquiring knowledge for the interaction of atoms and small molecules with surfaces is fundamental to extrapolate to larger chemical systems. When an atom or a molecule impinges on a surface, different elementary processes can take place as a consequence of the interaction:

Scattering or Reflection

In this process, the impinging molecule is sent back to the vacuum by the repulsive force generated by the surface at short distances (Figure I.1). When the parallel momentum to the crystal surface of the scattered projectiles changes by discrete amounts, the process is denoted as *coherent* or *diffractive scattering*. Diffraction is observed when the wavelength associated to the particle is of the order of magnitude of the surface lattice parameter and the adsorbates are localized on the adsorption wells. This quantum effect makes the angular distribution of a molecular beam scattered from a surface to present a discrete peaks distribution. Otherwise, the process is denoted as *incoherent scattering*.

Diffraction patterns give information about the surface structure and lattice dynamics of a material. In fact, molecular (atomic) beam diffraction experiments have became a common surface analysis technique [14], like the Helium Atom Scattering (HAS) and H_2 (D_2) Thermal-Energy Molecule Scattering (TEMS), or the more recent Grazing Incidence Fast Atom Diffraction (GIFAD) and Grazing Incidence Fast Molecule Diffraction (GIFMD) techniques.

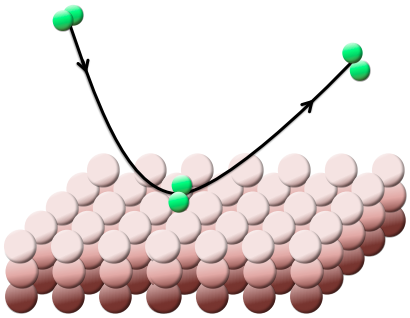

Figure I.1: *Reflection* process.

Adsorption

The impinging molecule equilibrates with the lattice and gets stuck on the surface (Figure I.2). If the electronic structure of the molecule is hardly perturbed upon *adsorption*, i.e., when there is a weak interaction between molecule-surface induced dipole moments, the process is denoted as *physisorption*. When the electronic structure of both, the molecule and the surface, is strongly perturbed the process is denoted as *chemisorption*. For instance, while N_2 chemisorbs on Ni(110), it is only found to physisorb on Pt(111) [15]. In some cases, molecules physisorb on their own chemisorbed layers [16], like CO_2 does on MgO(100) surface [17]. When it comes to molecules, two kind of chemisorption can be distinguished. If fragmentation occurs, it is denoted as *dissociative chemisorption*,

and otherwise as *molecular chemisorption*. *Dissociative chemisorption* is an important elementary process since it is a determining step in many synthesis processes for example in ammonia synthesis ($^3/_2H_2 + {}^1/_2N_2 \rightarrow NH_3$) or CO oxidation ($CO + {}^1/_2O_2 \rightarrow CO_2$). As a consequence, it has been widely studied, in particular for simple molecules such as H_2, N_2 and O_2 [18–34].

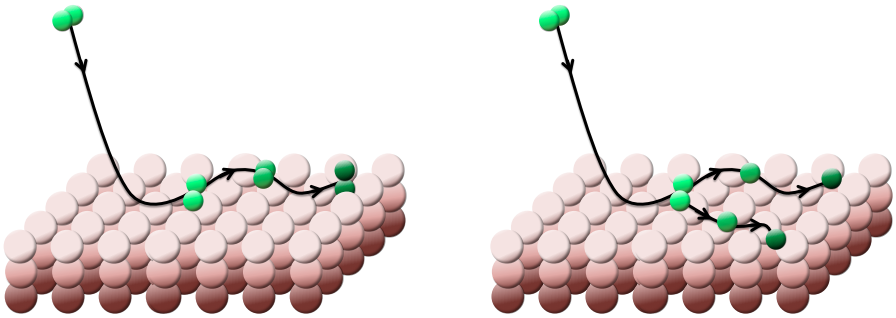

Figure I.2: *Adsorption* processes. Left: *Physisorption* or *molecular chemisorption*. Right: *Dissociative chemisorption*.

An efficient *adsorption* process will cover the surfaces with adsorbates. The coverage importantly affects all gas-surface elementary processes. Therefore, a good knowledge of surface coverage, as well as of its characteristics (adsorbates arrangement, adsorption energies and vibrational modes), is essential. Nowadays many experimental techniques are accessible that allow a very precise characterisation of surfaces [35]. Apart from HAS and TEMS, Low Energy Electron Diffraction (LEED) and neutron diffraction allow to determine the structure of surfaces and adsorbates arrangements. Using photoelectron spectroscopies (UV spectroscopy and X ray spectroscopy) and Auger electron spectroscopy surface composition and chemical state (molecular or atomic) of the incoming molecule on the surface or adsorbate coverage can be known. Thanks to Energy Electron Loss Spectroscopy (EELS), vibrational modes of the adsorbates can be known. Moreover, using the Atomic Force Microscopy (AFM) and the Scanning Tunneling Microscopy (STM) the topology of the surface (AFM and STM) and the electronic structure of the surface (STM) can be measured. The electronic structure can be also be measured by Angle-resolved photoemission spectroscopy (ARPES). To know adsorption energies Temperature Programmed Desorption (TDP) technique can be applied.

Absorption

The molecule or atom penetrates into the subsurface and equilibrates into the metal bulk (Figure I.3). Many studies have focussed on simple molecules absorption on metal surfaces [36–40]. In particular, many efforts have been dedicated at understanding hy-

drogen absorption on metal surfaces [37] due to its importance in metal embrittlement, hydrogen purification and hydrogen storage [41]. In general H occupation of the surface is energetically favored, and at relatively low coverage (0.25 ML), the existence of subsurface H is not expected [37]. However, subsurface atoms play an active role in several chemical reactions. For instance, hydrogenation reactions on Ni and on Pd nanoparticles [42, 43] imply the presence of subsurface atoms. In CO oxidation on Rh(111), subsurface O acts as a reservoir for replenishing reagent as it is consumed [44].

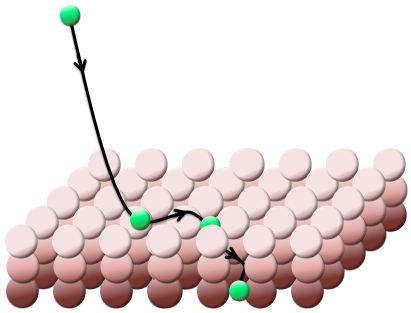

Figure I.3: *Absorption* process.

Abstraction or Recombination:

Adsorbed atoms are removed from the surface by combining with atoms coming from the gas phase (Figure I.4). Surface *recombination* proceeds through either *Langmuir-Hinshelwood (LH)* [45], *Eley-Rideal (ER)* [46] or *Hot-Atom (HA)* [47] *recombination*. The two formers can be considered as a limit mechanisms. *LH* mechanism occurs when chemisorbed species recombine after thermal diffusion. *ER* mechanism occurs when an atom from the gas phase hits the surface and is scattered within a single collision as a molecule, i.e., bound to a previously adsorbed atom. The *HA* mechanism can be considered as the intermediate process between *ER* and *LH*. First, the gas-atom/molecule gets trapped on the surface due to energy exchange with the surface and/or the adsorbates or by energy transfer from normal to parallel motion. This trapped atom on the surface but not equilibrated with it, is denoted as an *hot atom*. While the *hot atom* travels on the surface it experiences further energy exchanges. Finally, it may collide with an adsorbate and recombine.

In the last decades, numerous theoretical [48–68, 68–80] and experimental studies [81–97] have considered *recombination* on metals. Very different behaviors have been observed depending on the recombining species and the metal surface. As atom chemisorption energy is usually large on such materials, thermal *recombination* via the *LH* reaction is ineffective at low temperature. Rather, recombinations may proceed

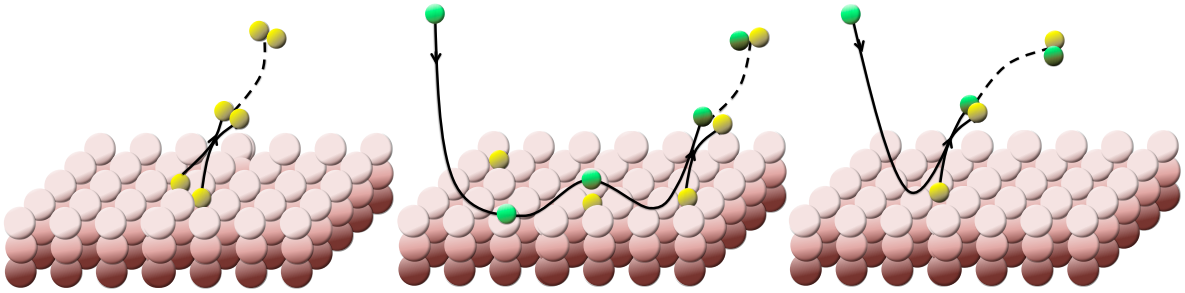

Figure I.4: *Recombination* processes: *LH* (left), *HA* (middle) and *ER* (right) mechanisms.

via *ER* or *HA abstraction*. The *recombination* of light projectiles (H,D) [48, 49, 58, 68, 69, 74, 81, 82, 84, 86, 90, 94] was suggested to mainly proceed via *HA recombination*, in which the incoming gas-phase species experiences few collisions with the surface prior recombining with the adsorbate. Conversely, the *ER abstraction* is thought to be less efficient. However, this assertion should be considered with care as recent theoretical studies evidenced that *ER* and *HA* mechanisms may compete in the *recombination* of H_2 from H-covered W(110), as a result of dissipation of energy to other adsorbates during the hyperthermal diffusion of the *hot atoms* [78]. Thus, though the single-collision *ER* reaction cross sections are generally small, with some exceptions such as N_2 formation on Ag(111) [70, 92], or H *recombination* with adsorbed Cl on Au(111) [68], they might be a non negligible contribution to the total *abstraction* cross sections.

The molecular beams (MB) technique [1, 98] is one of the most useful experimental tools to study the dynamics and kinetics of gas-surface processes. A MB is a spatially well-defined, directed and collision-free flow of molecules. The beam source is generated by a supersonic expansion of a gas flowing through an orifice (nozzle) to a chamber at lower pressure. Numerous MB setups of different complexity have been described [98]. For dynamical studies, the distribution of energy over the different external and internal degrees of freedom (DOF) can be controlled. A wide range of translational energies can be covered by changing the temperature of the nozzle or by mixing the gas of interest with a gas of different mass (seeding gas). The desired vibrational and rotational states can be selected by laser irradiation [99–101] or focusing of pre-existing states by electric fields. Besides, polar reagents approach geometry can be also controlled by a external electric field, such as a strong homogeneous electric field [102] or an inhomogeneous field created by a hexapole [103]. If the reaction of interest involves several reactants, these can either be introduced via the background gas or by crossing several beams on the sample surface. Detection of gas phase molecules is realized by means of quadrupole mass spectrometry, bolometric detection or laser spectroscopy. Alternatively, time-resolved surface spectroscopies can be applied in order to obtain information on adsorbed species.

Information on the rovibrational states population of the formed products can be gained by resonance enhanced multiphoton ionization (REMPI) spectroscopy [104] or by analyzing the released infrared emission (infrared chemiluminescence) [105]. Furthermore, Laser Induced Fluorescence (LIF) [106] and Femtosecond Transition-state Spectroscopy (FTS) [107] allow to detect transition states of the reactions. Bond breaking and bond forming processes are thus detected. Depending on the setup, the incidence angle, the kinetic energy, the vibrational or rotational energy distribution or the orientation of the incident molecules can be varied and the sticking probability, the angular distribution, the velocity distribution or the vibrational or rotational energy distribution of desorbing or scattered species can be detected [98].

In the past years, unprecedented accuracy has been achieved in the theoretical description of dynamics of elementary processes at metal surfaces thanks to the development of initio electronic structure calculations based on density functional theory (DFT) and the improvement in computational capabilities. Although more exact treatments are possible, most of the developed models are based on the Born-Oppenheimer approximation (BOA) [108] so that the electrons do not undergo transitions between stationary states [109]. Among them, two broad categories can be distinguished. Some methods rely on an analytic or numerical continuous representation of the molecule-surface interaction potential, i.e., the potential energy surface (PES), like classical dynamics and quantum dynamics simulations. The PES makes easy to calculate molecule-surface interactions when integrating the dynamics equations, so that relatively large systems and/or long time scales (ps) can be simulated. As a disadvantage, the results are limited by the quality and functional form of the analytic potential function or the numerical interpolation method. The representation of PESs has been a central issue since the beginning of the theoretical investigation of reaction dynamics [1]. Moreover, accurate fitting or interpolation becomes a very complex task as the number of nuclear DOFs of freedom increases (>6). In quantum dynamics, the time-dependent Schrödinger equation is propagated for the nuclei, thus quantum effects such as tunneling and zero-point energy (ZPE) are properly introduced in contrast with classical dynamics. However, due to the exponential growth of the number of DOF with the number of particles, a full quantum description is limited to only a few DOF in the problem. In contrast, classical simulations can include the full dimensionality of the surface and molecule if one is able to construct the full dimensional PES. Furthermore, ZPEs may be classically introduced, so that quasiclassical dynamics (QCT) is carried out.The second category methods are the so called *Ab-Initio* Molecular Dynamics (AIMD) in which the adiabatic forces acting on each atom are determined during the simulation (*on the fly*) by means of the Feynman-Hellmann theorem. Not needing to specify an analytic potential allows to include all the dimensionality straightforwardly but with a computational cost. Within

these methods simulations of long timescales, and/or great amount of trajectories are not yet practical. As a consequence, the required averaging over many different initial conditions in order to ensure reasonable statistics may not be affordable within the most accurate methods. Depending on the characteristics of the process of interest (probability, number of involved atoms, timescale) a compromise needs to be found between the accuracy and computational cost of the approach.

Comparison of these theoretical approaches with experimental measurements has proven their reliability for many gas-surface systems [110]. Furthermore, molecular dynamics calculations have proven to be a powerful tool to understand gas-surface reaction dynamics. The potential of molecular dynamics simulations was for instance demonstrated when studying non-activated (barrierless) adsorption processes. The initial decrease of the sticking probability with kinetic energy observed in these systems was shown to be due to a dynamical mechanism, the steeringing effect [111, 112], previously underestimated. The importance of taking the appropriate multidimensionality of the interaction dynamics into account has been widely demonstrated [1, 113, 114].

However, the validity of the BOA might break down when non-adiabatic couplings take place upon gas-surface scattering. In fact, non-adiabaticity of gas-surface interactions have been evidenced in a number of experiments [115–123]. The BOA may break down when the process involves spin state changes, electron transfer or electronic (de)excitation of the projectile. In that case, for correctly representing these processes diabatic or multiple PESs are necessary, together with couplings connecting them, since the gas-surface interactions are highly affected by these electronic structure changes. When non-adiabaticity is due to energy exchange between the internal DOFs of the projectile and the surface electrons (electron-hole pair excitations), although they may dramatically affect the processes due to the fact that the energy losses might difficult overcoming barriers or favor steering effects, the interaction potential is not importantly affected, i.e., the minimum energy PES properly represents the forces on the electronically excited system. In the last years, different *ab initio* theories have been developed to deal with $e-h$ pair excitations in molecular processes on metal surfaces [1]. Among them, a good compromise between accuracy of results and simplicity of implementation is offered by the local density friction approximation (LDFA) [124], as shown in ref [125]. Within this model, the energy dissipation in adsorption [126–128], scattering [129–131] and dissociation [124, 131–133] processes on metal surfaces have been analyzed. Moreover, the description of such processes using an high-dimensional *ab initio* PES and accounting for both $e-h$ pair and phonon excitations processes has been achieved by combining LDFA and the generalized Langevin oscillator model (GLO) [134] to incorporate energy exchange with the lattice phonons [135].

From the mentioned gas-surface elementary processes, we focus on *recombination* via *ER* and *HA* mechanisms. While coupling to phonons has been studied within the framework of *recombination*, coupling to $e-h$ pair excitations has been neglected so far, despite they have been suggested to determine the *HA abstraction* kinetics [136]. Within this context, the main objective of this thesis is precisely to study for the first time the role of $e-h$ pair excitation in these two mechanisms. To do so, we investigate H and N *abstraction* from the W(100) and W(110) surfaces. The choice of adsorbate is motivated by the knowledge acquired on other elementary processes, for which non-adiabatic effects have recently been studied theoretically [126, 128, 137–139]. While studying the *adsorption* of different species, the relaxation of the *hot* H *atoms* formed upon dissociation of H_2 on Pd(100) is shown to be completely dominated by $e-h$ pair excitations. For heavier chemical elements such as O_2, N and N_2, in contrast, phonons dominate the initial stage of the *adsorption* process but still a substantial excitation of $e-h$ pairs is active during the long time scales that involve the final accommodation of the adsorbates on the well. Therefore, our choice of systems will allow us to gain a rather broad view of non-adiabaticity on *recombination* processes. Since the energy loss channels determine the hyperthermal diffusion time of the *hot atoms*, they will importantly affect the *HA* reactivity if efficient. In an *ER* reaction, in contrast, the hyperthermal diffusion is not relevant, but the high amount of energy released in the reaction may substantially excite electrons and, consequently, be transferred to the metal. In the case of HCl formation on Au(111) [85], for instance, part of the energy loss was suggested to proceed via $e-h$ pair excitations [69]. Regarding the selection of the metal substrate, tungsten is precisely the armor material of choice for the plasma-facing components of the ITER divertor [13], which must control the exhaust of waste gas and impurities from the reactor and withstands the highest surface heat loads. Within this area, it is essential to study the interaction between H atoms and molecules on tungsten surfaces and the energy flow to the metal within a large range of energies of the order of electron volts and more [140]. Since for practical applications polycrystalline metals are used, an important aspect of gas surface reactions is the influence of crystallographic anisotropy. Moreover, the differences in the electronic structures of the different crystal faces may also influence the energy exchange with electronic excitations. The study of the two low index crystal faces, which are indeed the most abundant in the polycrystalline W metal, facilitates to evaluate these aspects. Besides, the *ER* process is of special interest as it is usually very exothermic, and therefore, it provides highly excited molecules [141–143] of potential interest for negative ions productions [144]. The theoretical approaches employed in this thesis allow us to follow and analyze the dynamics of the *recombination* process in great detail. Particularly, the usual low probabilities of the *recombination* processes suggest the use of QCT relying on PESs. This approach has been widely used

and proved to be reliable in qualitative terms for these elementary processes. The thesis is organised as follows:

Chapter II, III and IV detail the theoretical model employed, i.e., QCT simulations. These method requires three steps:

(a) First, several *ab initio* potential energy values of the atom/molecule-surface interaction are determined by first-principles. In Chapter II, the methods applied for the calculation of the electronic structure, i.e., the BOA and DFT, are presented.

(b) Second, a fit or interpolation of these total energies is performed to get a continuous representation of the atom/molecule-surface interaction, that is, the PES. The methods used for the construction of the PESs investigated in this work are described in Chapter III: the Flexible - Periodic - London - Eyring - Polanyi - Sato (FPLEPS) function and the Corrugation Reducing Procedure (CRP).

(c) Third, classical equations of motion for the nuclei are integrated. In Chapter IV the equation of motion and the integration procedure are presented. In addition, the theoretical models used for electronic and phonon excitations are described.

Chapter V, VI, VII and VIII present the particular results obtained within the different investigations carried out.

(d) In Chapter V the dissipation of energy to metal surfaces upon *ER recombination* is investigated. The *ER abstraction* of (i) light H atoms on both W(100) and W(110) crystallographic planes, and (ii) that of heavier N atoms in the same surfaces are studied. The combination of LDFA and GLO model allow us to study the competition of the two main energy loss channels and their influence on the *recombination* dynamics.

(e) In Chapter VI, the stereodynamics of diatom formation through *ER* reactions is investigated. The systems studied in the previous chapter are analyzed under several projectile incidences. The different gas-surface potential interaction and consequent *ER* dynamics allow us to gain a rather wide vision about different stereodynamical behaviors on *ER* reactions. In addition, the influence of energy dissipation to the metal is also described.

(f) In Chapter VII, the role of $e-h$ pair excitations in *HA recombination* is investigated. To do so, H *abstraction* from the W(110) surface at different H-coverages is

analyzed. This allows to study the competition between electronic excitations and projectile-adsorbates collisions in drawing out energy from the projectile, which determines the lifetime of the *hot atoms*.

(g) In Chapter VIII, the role of $e-h$ pair excitations in *HA recombination* is re-investigated, but on the W(100) crystal face instead of on the W(110). Comparing with previous results, the influence of the tungsten crystallographic plane on the H *abstraction* dynamics is analyzed. Similarly, this allows us to study the dependence of the energy losses on the surface crystal face.

Chapter IX summarizes the most relevant results.

Chapter II

Modelling molecule-surface interactions

Ab initio dynamics calculations of chemical processes require a theoretical method to describe the interaction between the involved chemicals. When it comes to molecule-surface interactions, unfortunately, the complete description of the total number of nuclei and electrons is computationally too costly to be feasible. In the case of crystal surfaces, the most viable alternative is the use of the BOA and DFT. In this chapter the theoretical methods used to describe the molecule-surface interaction will be described.

II.1 Born-Oppenheimer approximation

In gas-surface systems many atoms are involved, thus, let us start considering a system of N nuclei and N_e electrons, and simplifying the problem not considering the spin. The system is described by the coordinates of the nuclei $(\mathbf{R}_1, ..., \mathbf{R}_N \equiv \mathbf{R})$ and electrons $(\mathbf{r}_1, ..., \mathbf{r}_{N_e} \equiv \mathbf{r})$, as well as their respective masses $(M_1, ..., M_N)$ and (m_e). Then, we may write the non-relativistic Hamiltonian as a sum of five terms

$$H = T_{\mathrm{N}}(\mathbf{R}) + T_{\mathrm{e}}(\mathbf{r}) + V_{\mathrm{ee}}(\mathbf{r}) + V_{\mathrm{NN}}(\mathbf{R}) + V_{\mathrm{eN}}(\mathbf{r}, \mathbf{R}), \tag{II.1}$$

where T_N is the kinetic energy of the nuclei, T_e the kinetic energy of the electrons, V_{ee} the Coulomb electron-electron interaction, V_{eN} the Coulomb electron-nucleus interaction and V_{NN} the interaction among the nuclei. In atomic units ($m_e = \hbar = e = 1$) the components of the Hamiltonian are

$$T_{\mathrm{N}}(\mathbf{R}) = -\sum_{I=1}^{N} \frac{\nabla_I^2}{2M_I}\,, \tag{II.2}$$

$$T_{\mathrm{e}}(\mathbf{r}) = -\sum_{i=1}^{N_e} \frac{\nabla_i^2}{2}\,, \tag{II.3}$$

$$V_{\mathrm{ee}}(\mathbf{r}) = \sum_{i>j} \frac{1}{|\mathbf{r}_i - \mathbf{r}_j|}\,, \tag{II.4}$$

$$V_{\mathrm{NN}}(\mathbf{R}) = \sum_{I>J} \frac{Z_I Z_J}{|\mathbf{R}_I - \mathbf{R}_J|}\,, \tag{II.5}$$

$$V_{\mathrm{eN}}(\mathbf{r},\mathbf{R}) = -\sum_{i,I} \frac{Z_I}{|\mathbf{R}_I - \mathbf{r}_i|}\,. \tag{II.6}$$

The last four terms can be gathered in what we will designate as electronic Hamiltonian,

$$H_e(\mathbf{r},\mathbf{R}) = T_{\mathrm{e}}(\mathbf{r}) + V_{\mathrm{ee}}(\mathbf{r}) + V_{\mathrm{NN}}(\mathbf{R}) + V_{\mathrm{eN}}(\mathbf{r},\mathbf{R})\,. \tag{II.7}$$

A stationary state is described by a wave function of the system $\Psi(\mathbf{r},\mathbf{R})$ that satisfies the many-body time-independent Schrödinger equation,

$$H\Psi(\mathbf{r},\mathbf{R}) = \left[T_{\mathrm{N}}(\mathbf{R}) + H_e(\mathbf{r},\mathbf{R})\right]\Psi(\mathbf{r},\mathbf{R}) = E\Psi(\mathbf{r},\mathbf{R})\,. \tag{II.8}$$

This is obviously an insoluble problem and approximations must be made. Let us start considering $\{\phi_q\}$, a complete orthonormal basis of eigenfunctions of the electronic Hamiltonian H_e for a given set of nuclear positions $\mathbf{R}$. Then, the total wave function can be expanded in this basis of eigenfunctions,

$$\Psi(\mathbf{r},\mathbf{R}) = \sum_q \phi_q(\mathbf{r},\mathbf{R})\chi_q(\mathbf{R})\,. \tag{II.9}$$

Reinserting Eq. (II.1), (II.7) and (II.9) in the original Schrödinger equation, Eq. (II.8), we obtain:

$$\left[T_{\mathrm{N}}(\mathbf{R}) + H_e(\mathbf{r},\mathbf{R}) - E\right]\sum_q \phi_q(\mathbf{r},\mathbf{R})\chi_q(\mathbf{R}) = 0\,. \tag{II.10}$$

Projecting over $\langle\phi_s|$ leads to the following relation, in which we have adopted the Dirac notation to simplify the writing:

$$\sum_q \langle\phi_s|(T_{\mathrm{N}} + H_{\mathrm{e}} - E)|\phi_q\rangle\chi_q = 0\,. \tag{II.11}$$

Finally, making use of the orthonormality condition of $\{\phi_q\}$ ($\langle\phi_s|\phi_q\rangle = \delta_{sq}$) the latter

expression becomes

$$\sum_q \langle\phi_s|T_{\mathrm{N}}(|\phi_q\rangle\chi_q) + E_{\mathrm{e}}(\mathbf{R})\chi_s - E\chi_s = 0\,, \tag{II.12}$$

where $E_{\mathrm{e}}(\mathbf{R}) = \langle\phi_s|H_{\mathrm{e}}|\phi_s\rangle$ is the potential energy of the electronic state ϕ_s for a given set of nuclear positions $\mathbf{R}$.

Considering Eq. (II.2) the expansion of the terms with the nuclear kinetic energy operator leads to

$$\begin{aligned} T_{\mathrm{N}}(|\phi_q\rangle\chi_q) &= -\sum_{I=1}^{N}\frac{1}{2M_I}\nabla_I^2(|\phi_q\rangle\chi_q) \\ &= -\sum_{I=1}^{N}\frac{1}{2M_I}(\nabla_I^2|\phi_q\rangle\chi_q + 2\nabla_I|\phi_q\rangle\nabla_I\chi_q + |\phi_q\rangle\nabla_I^2\chi_q)\,. \end{aligned} \tag{II.13}$$

The BOA consists in neglecting the terms $\langle\phi_s|\nabla_I^2|\phi_q\rangle$ and $\langle\phi_s|\nabla_I|\phi_q\rangle$. M. Born and R. J. Oppenheimer [145] argued that as nuclei are much slower than the electrons due to the enormous mass difference between them ($m_p \approx 1836\, m_e$), the electronic state of the system is automatically adapted to the movement of the nuclei.

This leads to the possibility of rewriting Eq. (II.8) as separate electronic and nuclear Schrödinger equations (SE), i.e., the motion of the electrons is uncoupled from the motion of the nuclei:

$$H_{\mathrm{e}}(\mathbf{r},\mathbf{R})\ \phi_s(\mathbf{r},\mathbf{R}) = E_{\mathrm{e}}(\mathbf{R})\ \phi_s(\mathbf{r},\mathbf{R})\,, \tag{II.14}$$

$$[T_{\mathrm{n}} + E_{\mathrm{e}}(\mathbf{R})]\,\chi_s(\mathbf{R}) = E\ \chi_s(\mathbf{R})\,. \tag{II.15}$$

$E_{\mathrm{e}}(\mathbf{R})$ is known as the PES of the electronic state ϕ_s. As Equation II.15 shows, it represents an effective potential created by the electrons in the ϕ_s state, which determines the movement of the nucleus. Within the BOA, the theoretical description of a dynamic process includes two stages: first, the electronic Hamiltonian H_e is solved, and second, nuclear dynamics are performed on that PES.

Since it is only an approximation, its validity has to be checked carefully. In gas-surface scattering, electronically non-adiabatic processes might indeed be occurring, and it is not easy to give a general statement on whether the dynamics in any particular system is well described or not with the electronically adiabatic approximation. The usual argument for the validity of the Born-Oppenheimer approximation is the smallness of the atomic velocities as compared with the electronic velocities. If in addition the stationary

electronic states are well-separated in energy, electronic transitions are expected to be negligible. For metals, the situation is more complicated due to the quasi-continuum of electronic states. Since the effective potentials and the coupling between the electronic states can still not be computed rigorously, one is left with more or less hand-waving arguments. On the one hand, electronic excitations at metal surfaces are very short-lived and as a consequence electronic excitations are effectively quenched. On the other hand, molecular electronic levels become rather broad upon the interaction with surfaces. The lifetimes of these broad levels are short, leading again to an effective quenching of electronic excitations [113].

II.2 Density Functional Theory

Within the BOA it is possible to DFT to calculate the electronic ground state of the atom/molecule-surface system and the corresponding PES. Modern DFT is based on two theorems of Hohenberg and Kohn (HK) [146] and on the Kohn-Sham (KS) equations, which will be briefly described in this Section.

1. **The Hohenberg-Kohn Theorems**

   The first HK theorem states that the external potential is uniquely determined, except for a constant shift of the energy, by the ground-state electronic density, so it is possible to use the density as a basic variable. This is a great improvement over wave function based methods because the DOF are reduced from $3N_e$ to 3. Conversely, the ground-state density is uniquely determined by the external potential, within an additive constant. Accordingly, the electronic energy can be written as a functional of the density $\rho(r)$,

   $$E[\rho(\mathbf{r})] = T_e[\rho(\mathbf{r})] + V_{ee}[\rho(\mathbf{r})] + V_{eN}[\rho(\mathbf{r})] = F_{HK}[\rho(\mathbf{r})] + V_{eN}[\rho(\mathbf{r})]. \quad \text{(II.16)}$$

   The Hohenberg-Kohn functional $F_{HK}[\rho(\mathbf{r})]$ contains the $T_e[\rho(\mathbf{r})]$ and $V_{ee}[\rho(\mathbf{r})]$ terms, which are universal for a given Coulomb interaction and do not depend on the external potential. The electron-electron term can be written as

   $$V_{ee}[\rho(\mathbf{r})] = E_H[\rho(\mathbf{r})] + G_{XC}[\rho(\mathbf{r})], \quad \text{(II.17)}$$

   where E_H is the Hartree energy, the "classical" electrostatic repulsion, and G_{XC} contains the exchange and the correlation. Exchange and correlation are two terms intimately connected: while the electronic correlation refers to the interaction between nonindependent electrons, the exchange energy of interacting electrons

depends on the spin state and on the fact that when two electrons are exchanged the wave function must change sign (Pauli principle).

The second HK theorem uses the variational principle to show that the density that minimises the total energy is the exact ground-state density, $\rho(\mathbf{r})$,

$$E_{tot} = min\ E[\rho(\mathbf{r})]\,. \tag{II.18}$$

Thus, if the energy functional was known, the variational principle could be used to determine the exact ground state density. Unfortunately, the exact analytical form of the $F_{HK}[\rho(\mathbf{r})]$ functional is unknown. This problem is tackled in an efficient way in the KS equations, as shown next.

2. **The Kohn-Sham Equations**

Kohn and Sham developed a practical method to calculate the ground state density. For this purpose they consider a fictitious reference system of N_e non-interacting electrons subject to an effective (fictitious) potential whose density $\hat{\rho}(\mathbf{r})$ is the same as the density of the interacting system $\rho(\mathbf{r})$,

$$\hat{\rho}(\mathbf{r}) = \sum_{i=1}^{\mathrm{Ne}} \langle\hat{\phi}_i|\hat{\phi}_i\rangle = \rho(\mathbf{r})\,. \tag{II.19}$$

The wave function associated to the non-interacting particles is a Slater-Determinant, constructed from a set of the so-called Kohn-Sham orbitals $\hat{\phi}_i$. In this way, the overall SE is separated in individual ones with an effective potential [147],

$$\left[-\frac{1}{2}\nabla^2 + v_{eff}(\mathbf{r})\right]\hat{\phi}_i = \epsilon_i\hat{\phi}_i\,, \tag{II.20}$$

where the effective potential is

$$v_{eff}(\mathbf{r}) = v_{ext}(\mathbf{r}) + \int \frac{n(\mathbf{r}')}{|\mathbf{r}-\mathbf{r}'|}d^3\mathbf{r}' + v_{xc}(\mathbf{r})\,. \tag{II.21}$$

Within this formalism, the kinetic energy contribution becomes $T_S = \langle\hat{\phi}_i| - \frac{1}{2}\nabla^2|\hat{\phi}_i\rangle$, i.e., the kinetic energy of a system of non-interacting electrons moving in an effective potential $v_{eff}(\mathbf{r})$ [148]. Thus an unknown component $T_C[\rho(\mathbf{r})]$ that contains the corrections resulting from the electronic interaction must be added. The $T_C[\rho(\mathbf{r})]$ component is combined with the additional contribution of the electron-electron interaction G_{XC} into one exchange-correlation energy functional $E_{XC}[\rho(\mathbf{r})]$, that includes all the many-body effects not captured by both

T_S and E_H,

$$E_{XC}\left[\rho(\mathbf{r})\right] = T_e\left[\rho(\mathbf{r})\right] - T_S\left[\rho(\mathbf{r})\right] + V_{ee}\left[\rho(\mathbf{r})\right] - E_H\left[\rho(\mathbf{r})\right]. \tag{II.22}$$

The functional derivative of $E_{XC}\left[\rho(\mathbf{r})\right]$ respect to the density is the definition of the exchange-correlation potential $v_{XC}\left[\rho(\mathbf{r})\right]$,

$$v_{XC}\left[\rho(\mathbf{r})\right] = \frac{\delta E_{XC}\left[\rho(\mathbf{r})\right]}{\delta\rho(\mathbf{r})}. \tag{II.23}$$

3. **Exchange-Correlation Functionals**

The first two terms in Eq. (II.21), the external and electrostatic potential, are well known, but the last term v_{xc} is still undefined, so it is necessary to use an approximation. The simplest approximation is the local-density approximation (LDA), that assumes that the exchange-correlation energy depends only on the local value of the density,

$$E_{xc}[\rho(\mathbf{r})] = \int \rho(\mathbf{r})\epsilon_{xc}[\rho(\mathbf{r})]d\mathbf{r}. \tag{II.24}$$

The LDA has been for a long time the most widely used approximation to $E_{xc}[\rho(\mathbf{r})]$. However, the LDA typically overestimates binding energies and underestimates bond lengths and lattice constants [149]. Thus, more complex functionals that include the gradient of the electronic density have been developed, yielding the generalised gradient approximation (GGA) functionals,

$$E_{xc}[\rho(\mathbf{r})] = \int \rho(\mathbf{r})\epsilon_{xc}[\rho(\mathbf{r}), \nabla\rho(\mathbf{r})]d\mathbf{r}. \tag{II.25}$$

The PESs studied in the present thesis were constructed employing the traditionally most common GGA functionals used in gas-surface dynamics simulations: the Perdew-Wang 1991 (PW91) [150] and the Revised Perdew-Burke-Ernzerhof (RPBE) [151].

II.3 Modelling the system

Depending on the code, DFT calculations use different basis sets. Very often plain waves are used to represent electronic wave functions, which are eigenfunctions of the free-electron SE, and therefore, the natural basis to describe bands in the nearly-free-

electron approximation. Computationally, this expansion is particularly useful to deal with periodic crystals because it provides simple and fast algorithms [152].

In the present thesis, self-consistent KS equations (Eq. II.20) are applied. As Bloch's theorem [153] states for crystal solids, the solution to this equation are the so-called Bloch functions $\phi_k(\mathbf{r})$, which are product of a plane wave and a function with the periodicity of the lattice,

$$\phi_k(\mathbf{r}) = e^{i\mathbf{k}\,\mathbf{r}}\, u_k(\mathbf{r}), \tag{II.26}$$

$$u_k(\mathbf{r}) = u_k(\mathbf{r} + \mathbf{R}), \tag{II.27}$$

where k is a wavevector within the first Brillouin zone and $\mathbf{R}$ is any vector of the Bravais lattice defined by $\mathbf{R} = n_1\mathbf{a}_1 + n_2\mathbf{a}_2 + n_3\mathbf{a}_3$ (where $\mathbf{a}_1$, $\mathbf{a}_2$ and $\mathbf{a}_3$ are the linearly independent three dimensional primitive vectors of the Bravais lattice).

Since $u_k(\mathbf{r})$ is a periodic function, we may expand it in terms of a Fourier series:

$$u_i(\mathbf{r}) = \sum_{\mathbf{G}} c_{i,\mathbf{G}} e^{i\mathbf{G}\cdot\mathbf{r}}, \tag{II.28}$$

where the $\mathbf{G}$ are reciprocal lattice vectors defined through $\mathbf{G}\cdot\mathbf{R} = 2\pi m$, m is an integer, $\mathbf{R}$ is a real space lattice vector and the $c_{i,\mathbf{G}}$ are plane wave expansion coefficients. The electron wave functions may therefore be written as a linear combination of plane waves:

$$\psi_{j,\mathbf{k}}(\mathbf{r}) = \sum_{\mathbf{G}} c_{j,\mathbf{k}+\mathbf{G}} e^{i(\mathbf{k}+\mathbf{G})\cdot\mathbf{r}}. \tag{II.29}$$

The series in Eq. (II.29) should be infinite, but in practice, the series are truncated in order to be handled computationally. To achieve a finite basis set, only plane waves with an associated kinetic energy $\frac{1}{2}|\mathbf{k}+\mathbf{G}|^2$ lower than a cut-off energy E_{cut} are considered. The kinetic energy cut-off is defined through

$$E_{cut} = \frac{1}{2}|\mathbf{k}+\mathbf{G}|^2, \tag{II.30}$$

and thus this fixes the highest reciprocal lattice vector $\mathbf{G}$ used in the plane wave expansion, resulting in a finite basis set.

Although the KS equations have been shown to be tractable using plane waves to expand the electron wave functions, all-electron calculation including both core and valence electrons are still prohibitively expensive when a plane wave basis set is employed. This is due to the tightly bound core orbitals, and the highly oscillatory nature of the

valence electrons, which demand a high value of E_{cut} to accurately describe the electronic wave functions [154].

To overcome this problem, it is possible to partition the electrons between core and valence states, because the majority of physical properties of solids depend on the valence electrons. The core electrons, on the other hand, are almost environment independent. Within the pseudopotential approximation [155–157], the core electrons and ionic potential are removed, which are replaced by a pseudopotential that acts on a set of pseudowave functions. The associated pseudowave function reproduces the true valence wave function outside a certain cut-off radius r_c, whereas inside, the nodal structure is suppressed, thus reducing the required E_{cut}.

Unfortunately, the problem of calculating an infinite number of electronic states in an infinite space has been transformed to one of computing a finite number of eigenstates at an infinite number of **k**–points in a single unit cell. However, in the limit of large volume, the **k**–points become a dense continuum. In this case, electronic wave functions in **k**–points that are close together can be roughly considered the same. Thus, the wave function in a region of the **k**–space can be represented by the wave functions on a single **k**–point,

$$\frac{1}{V_{BZ}} = \int_{BZ} d\mathbf{k} \approx \frac{1}{(2\pi)^2} \sum_{\mathbf{k}} \omega_{\mathbf{k}} \,. \tag{II.31}$$

Hence, only **k**–points from the irreducible Brillouin zone weighted by a symmetry factor $\omega_{\mathbf{k}}$ need to be calculated. In this thesis, the Monkhorst-Pack-grid [158] scheme is used, which is a standard **k**–point selection scheme that generates a regular grid in **k**–space.

From the simulations point of view, using periodic boundary conditions for a molecule-surface system is not a straight forward task. When it comes to surfaces, the system is only periodic in two dimensions, but not in the perpendicular direction to the surface (z). Thus, the three-dimensional periodicity assumed so far is broken in one direction. In this direction, the system goes from its bulk structure to vacuum. In the interface the bulk structure is distorted due to the lack of z translational symmetry. To reliably represent such a system, the most usual strategy followed is to create a suitable 3D supercell that can be repeated periodically in 3D-space. This is shown schematically in Figure II.1. This model is known as the supercell approach. It consist in using a set of finite atomic planes (crystal slab) alternated with a slab of empty space. The form and the size of the supercell depend on the physical system being studied. On the one hand, the number of surface layers to be modelled must be large enough to ensure that the bulk behaviour is recovered inside the crystal slab. On the other hand, the size of the vacuum slab must ensure that the surface behaviour is unaffected by the presence of the periodic replica of the crystal slab. Moreover, when the surface is modelled interacting

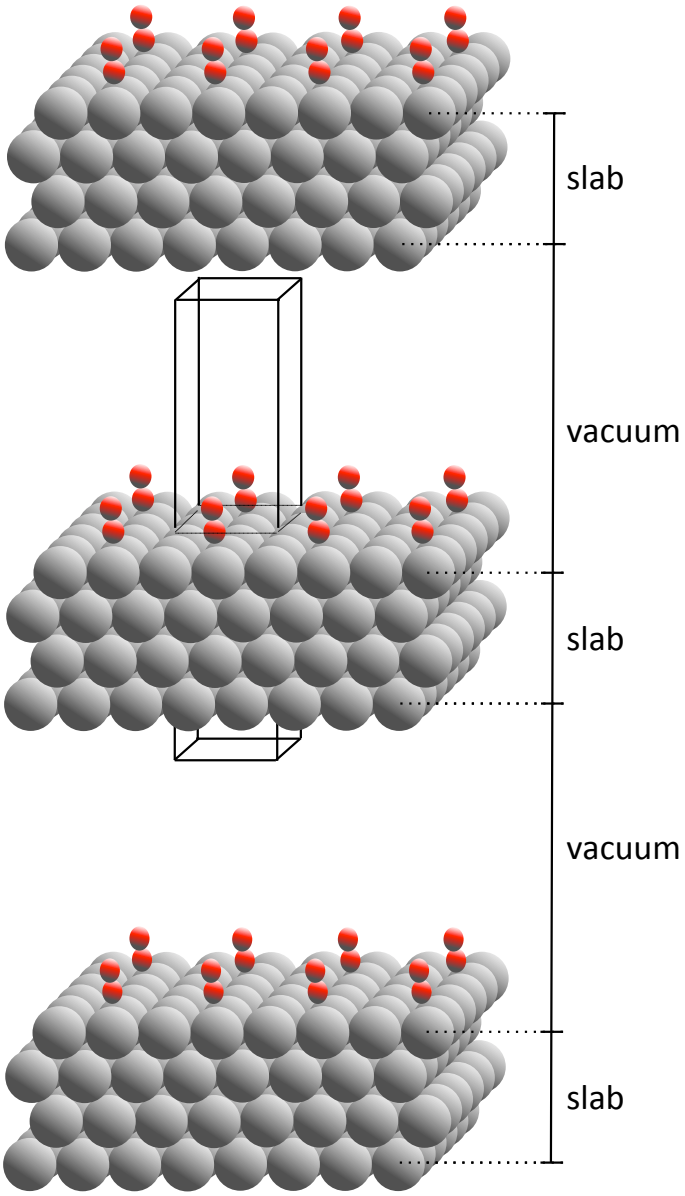

Figure II.1: Schematic representation of a 3×3 supercell of a primitive surface unit cell with an diatomic molecule modelled by a slab of four layers which are separated by vacuum along the z direction. The supercell is indicated by the solid black lines.

with some other molecule, the 2D unit cell should be big enough to make negligible the spurious interaction between the periodic images of the molecule. Thus, in order to minimise the computational cost, a supercell as small as possible ensuring an accurate representation of the system is used. Applying this model we can use standard periodic calculations codes without any modifications to obtain the desired electronic data.

Chapter III

Construction of a Potential Energy Surface

Once the interaction energies for several points of the desired configurational space are calculated, the PES must be built to provide a continuous representation of the molecule-surface interaction. This task might be achieved by fitting the total energies data to an analytical continuous representation or by interpolating it to a numerical continuous representation. When studying *ER recombination* within the single adsorbate limit, PESs fitted to the FPLEPS [159–161] function have been used. The study of both *ER* and *HA recombination* on covered surfaces has been carried out with PESs constructed following the CRP [162] method, in which the data is interpolated. These two methods are briefly presented on this Chapter.

III.1 Flexible - Periodic - London - Eyring - Polanyi - Sato function

The FPLEPS [159–161] model has its origin in the London - Eyring - Polanyi (LEP) potential, one of the first PES models for chemical reactions. The LEP potential is an analytical expression for a three-atom system [163], based on a valence bond treatment [164]. In order to improve the first formulation, an adjustable parameter (Sato parameter) substituting the overlap integrals [165, 166] was introduced. The consequent London - Eyring - Polanyi - Sato (LEPS) function has been widely used for triatomic reactions in the gas-phase [167, 168].

In order to adapt the LEPS potential to the gas-surface studies, an expression for the diatom-surface interaction was developed, the so called Periodic - London - Eyring -

Polanyi - Sato function (PLEPS) [18, 169]. This expression is based in a four-electron valence bond treatment.

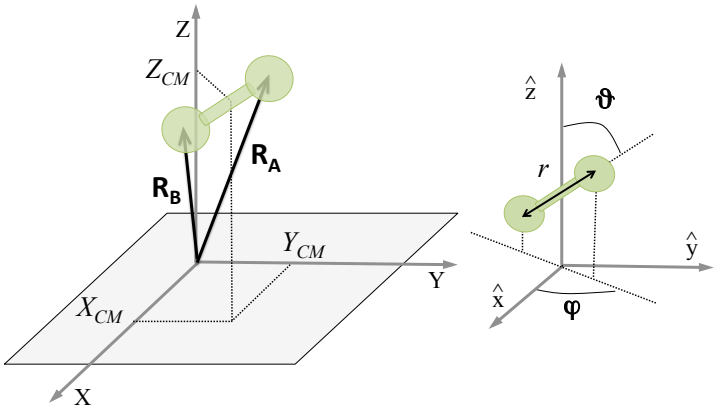

Figure III.1: Coordinate system used in the construction of the PESs.

In the 90s, the PLEPS function has been extensively used to describe the dynamics of dissociative molecular adsorption and that of *ER* recombination [1]. Unfortunately, the PLEPS potential, which is advantageous because of its simplicity, is not flexible enough to describe the intricate structure of high-dimensional PESs [159, 170, 171]. In order to overcome this shortcoming, the FPLEPS model was developed [12, 29, 172, 173]. Within the FPLEPS model, the generic form of the 6D potential $V^{6D}(\mathbf{R_A}, \mathbf{R_B})$for a molecule AB interacting with a solid surface M (Figure III.1) is defined as [76]:

$$\begin{aligned} V^{6D}(\mathbf{R_A}, \mathbf{R_B}) \;=\; & U_{AM}(\mathbf{R_A}) + U_{BM}(\mathbf{R_B}) + U_{AB}(|\mathbf{R_A} - \mathbf{R_B}|) \\ & -[Q^2_{AB}(|\mathbf{R_A} - \mathbf{R_B}|) + (Q_{AM}(\mathbf{R_A}) + Q_{BM}(\mathbf{R_B}))^2 \\ & -Q_{AB}(|\mathbf{R_A} - \mathbf{R_B}|)(Q_{AM}(\mathbf{R_A}) + Q_{BM}(\mathbf{R_B}))]^{\frac{1}{2}} \\ & +A_g \exp\left[-\frac{(Z_{CM} - Z^0_g)^2}{\sigma^2_g}\right], \end{aligned} \tag{III.1}$$

where U_i and Q_i are the Coulomb and exchange integrals for the two body terms respectively (i stands for AB, AM, BM), Z_{CM} is the altitude of the center of mass (CM) of the molecule, A_g, Z^0_g and σ_g are the parameters of the Gaussian function introduced in the FPLEPS to improve the description of the potential in the entrance valley, A_g is the amplitude, Z^0_g is the position of the maximum/minimum and σ_g is a parameter controlling the width of the Gaussian function. The bonding and anti-bonding states of the two body terms are approximated by Morse and anti-Morse functions. In this way,

U_i and Q_i read:

$$U_i = \frac{D_i}{4(1+\Delta_i)}[(3+\Delta_i)e^{(-2\alpha_i(d_i-d_i^{eq}))} - (2+6\Delta_i)e^{(-\alpha_i(d_i-d_i^{eq}))}] \quad \text{(III.2)}$$

$$Q_i = \frac{D_i}{4(1+\Delta_i)}[(1+3\Delta_i)e^{(-2\alpha_i(d_i-d_i^{eq}))} - (6+2\Delta_i)e^{(-\alpha_i(d_i-d_i^{eq}))}] \quad \text{(III.3)}$$

with $d_i = |\mathbf{R_B} - \mathbf{R_A}|$ for $i = AB$ and $d_i = Z_A$ (Z_B) for $i = AM$ (BM). D_i, α_i and d_i^{eq} are the Morse parameters, determined by a least square fitting of DFT points. For AM and BM interactions, such parameters are expanded in Fourier series adapted to the symmetry of the crystal. The Sato parameters Δ_{AM} ($= \Delta_{BM}$) and Δ_{AB} describe the strong interaction region of the PES. The Gaussian function and Sato parameters depend not only on the orientation of the molecule with respect to the surface, which is defined by the two angles ϑ and φ (see Figure III.1), but also on the lateral position of the CM of the molecule (X_{CM}, Y_{CM}) over the surface. The Gaussian function and Sato parameters were introduced in the FPLEPS model in order to represent the angular and surface-site (X_{CM}, Y_{CM}) corrugation. Such parameters are computed by a least-square fitting of the two-dimensional DFT 2D (Z_{CM},r) cuts, where r is the interatomic distance ($r = |\mathbf{R_A} - \mathbf{R_B}|$), on high symmetry sites. The angular interpolation over (ϑ,φ) is performed using a symmetry adapted expansion of trigonometric functions and a Fourier series is employed to describe the (X_{CM}, Y_{CM}) dependence of the molecular parameters (Gaussian and Sato parameters). A more detailed description of the FPLEPS model can be found in Refs. [12, 29, 172–174].

III.2 Corrugation Reducing Procedure

Since it was proposed by Busnengo *et al.* in 2000, the CRP method [162] has become a standard method to accurately represent the interaction of diatomic molecules on different metal surfaces [20,21,23,175,176] . This interpolation method takes into account that the strongest variations of the 6D PES mainly arise from the interaction between the atoms of the molecule and the surface when the molecule is close to it. Then, if the 3D atom-surface interactions V_i^{3D} are subtracted from the full PES V^{6D}, a smooth function remains (called interpolation function), which can be interpolated with higher accuracy than the corrugated full 6D-PES. Thus, the interpolation function I^{6D} can be written as

$$I^{6D}(X_{CM}, Y_{CM}, Z_{CM}, r, \vartheta, \varphi) = V^{6D}(X_{CM}, Y_{CM}, Z_{CM}, r, \vartheta, \varphi) - \sum_i V_i^{3D}(X_i, Y_i, Z_i)\,, \quad \text{(III.4)}$$

where the coordinates (X_{CM}, Y_{CM}, Z_{CM}, r, ϑ, φ) represent the six DOF of the molecule over the surface, being X_{CM} and Y_{CM} the Cartesian coordinates of the molecular CM with respect to the unit cell, Z_{CM} the distance between the CM of the molecule and the surface, r the molecular internuclear distance and ϑ and φ the molecular polar and azimuthal angles with respect to the surface, respectively. The variables X_i, Y_i and Z_i are the Cartesian coordinates of the ith atom of the molecule. This coordinate system is defined in Figure III.1.

The 3D PES for each atom of the molecule V_i^{3D} is also very corrugated. Thus, as done for V^{6D}, corrugation can be further reduced as follows:

$$I^{3D}(\mathbf{R}_i) = V^{3D}(\mathbf{R}_i) - \sum_{s=1}^{n} V^{1D}(|\mathbf{R}_i - \mathbf{R}_s|)\,, \tag{III.5}$$

where V^{1D} is a pair potential describing the interaction between one isolated atom and the sth surface atom, located each one at positions $\mathbf{R}_i$ =(X_i, Y_i, Z_i) and $\mathbf{R}_s$ = (X_s, Y_s, Z_s), respectively. The sum runs over all slab atoms n with non-zero contribution (i.e., nearest neighbors). This V^{1D} term is normally defined as the atom-surface interaction on a top site [24].

The CRP interpolation scheme for a 6D PES involves three main steps [1]:

1. The construction of the 1D atom-surface potential V^{1D} over a top site.
2. The construction of the 3D atomic potentials V^{3D}.
3. The construction of the 6D molecular potential V^{6D}.

For the CRP PESs used in the present work, atomic interpolation over Z_i is performed using cubic spline functions, while the interpolation over (X_i, Y_i) is carried out through Fourier series adapted to the lattice symmetry. I^{6D} is performed by using the internal coordinates. First, a numerical bidimensional spline interpolation is performed from (r, Z_{CM}) *ab initio* cuts. Second, the interpolation over (ϑ, φ) is carried out using trigonometric functions that fulfill the required symmetries as basis functions. Finally, the interpolation over (X_{CM}, Y_{CM}) is resolved using cubic splines.

The main advantage of CRP is the high accuracy of the interpolation due to the reducing of the corrugation. Moreover, the PES accuracy can be systematically improved by adding more *ab initio* data. In this way, interpolation errors lower than 100 meV can be achieved for the PES regions of importance for the dynamics [21, 76, 177, 178]. Conversely, the method cannot be extended directly to describe polyatomic molecules interaction with surfaces and the DOF of the solid.

III.3 Comparison of the Flexible - Periodic - London - Eyring - Polanyi - Sato and the Corrugation Reducing Procedure models

The study of non-adiabaticity and stereodynamics of H_2 and N_2 *ER recombinations* on W(100) and W(110) surfaces has been performed within the single adsorbate limit. To do so, four DFT-PESs fitted to the FPLEPS [159–161] function have been used. The study of H_2 *ER* and *HA recombinations* on H-covered W(100) and (W110) surfaces has been carried out with two DFT-PESs constructed following the CRP [162] scheme. Both, FPLEPS and CRP PESs have been extensively used for the study of gas surface elementary reactions. While the CRP PESs are more accurate than the FPLEPS ones, the construction of the FPLEPS PESs requires much less DFT data. For N_2 *dissociative adsorption* on W(100) [24, 161], for H_2 *recombination* on W(110) [76], and for H_2 recombination on W(100) (Chapter VIII) PESs constructed by the two models and the resulting classical dynamics calculations have been compared. Although differences are identified between the two PES representations due to the lower accuracy of the FPLEPS PESs, a semi-quantitative agreement is obtained when comparing classical dynamics calculations on the two PES models. Therefore, both PES models capture the main physical ingredients of the processes.

III.4 Multiadsorbate potential energy surfaces

In order to account for finite coverage effects in atom-adsorbate *recombination* processes multiadsorbate PESs need to be built. In principle, three-body and higher order interactions between adsorbates should be calculated. Nevertheless, in practice, for relatively low coverages, three or more atoms interactions may be disregarded as adsorbates are hardly sufficiently close together to make these interactions important. Thus, it might be sufficient to expand the interaction potential up to two-body terms. [179] This can be done with both FPLEPS and CRP PESs because in both cases the surface-atom and atom-atom interactions can be separated. In the present work, when studying *recombination* on covered surfaces, CRP PESs have been employed, whose expansion of the two body terms reads [78]:

$$V(\{\mathbf{R}_i\}) = \sum_{i=1}^{N} V^{3D}(\mathbf{R}_i) + \sum_{i=1}^{N}\sum_{j>i}^{N} I^{6D}(\mathbf{R}_i, \mathbf{R}_j)\,, \tag{III.6}$$

where $\mathbf{R}_i$ is the position vector of atom i, $V^{3D}(\mathbf{R}_i)$ is the 3D atom-surface interaction potential, and $I^{6D}(\mathbf{R}_i, \mathbf{R}_j)$ is the 6D diatomic interpolation function.

Chapter IV

Classical molecular dynamics

Although useful information can be extracted from a static analysis of the PESs (minimum energy reaction paths, minimum energy barriers of the reactive processes, the depth of the possible adsorption sites...), molecular dynamics calculations are indispensable to understand the elementary processes undergoing on the surfaces. In this respect, realistic dynamical simulations confirmed the importance of taking the appropriate multidimensionality of the interaction dynamics into account [1,113,114]. Unfortunately, the appropriate dimensionality in large systems makes a quantum mechanical description of the nuclear motion computationally not feasible. Alternatively, for atoms heavier than hydrogen or deuterium the quantum effects in the dynamics are in general negligible, and therefore, the description of the nuclear motion can be treated in a classical approximation [113, 180]. In fact, even in the hydrogen dynamics on metal surfaces, many integrated quantities such as the sticking probability have been semi-quantitatively or even quantitatively determined by classical dynamics [32, 181, 182]. In order to rationalise non-adiabatic effects, models that incorporate energy exchange with both lattice vibrations and electronic excitations keeping the accuracy of a multidimensional ab initio PES for the gas-metal interaction are used [129].

In the following sections, first, the classical equations of motion in the adiabatic case and within the frozen surface approximation will be presented. Subsequently, non-adiabaticity will be introduced in two forms, one as low-energy electronic excitations, the other as energy dissipation and exchange with the lattice. Finally, the calculation of several observables relevant to the recombination processes studied in this thesis will be described.

IV.1 Adiabatic classical dynamics

In order to analyze the dynamics of gas-surface interactions, the motion of the atoms must be modeled. Although this should be done for all the atoms in the system, in order to reduce the computational cost, only the movement of the reactive atoms might be considered. In that case, one assumes the frozen surface approximation, as it is done in the present work. In principle the motion of atoms/molecules should be treated quantically, thus the time-dependent nuclear Schrödinger equation should be solved in order to obtain the nuclear wave functions. According to the Ehrenfest's theorem, the time evolution of the mean values of the position ($\mathbf{R}_i$) and momentum ($\mathbf{P}_i$) operators can be described as

$$\begin{aligned} i\frac{d\langle \mathbf{R}_i\rangle}{dt} &= \langle [H, \mathbf{R}_i]\rangle = i\frac{\langle \mathbf{P}_i\rangle}{M_i}\,, \\ i\frac{d\langle \mathbf{P}_i\rangle}{dt} &= \langle [H, \mathbf{P}_i]\rangle = -i\big\langle \nabla_i V^{6D}(\mathbf{R}_i, \mathbf{R}_j)\big\rangle\,. \end{aligned} \tag{IV.1}$$

These two equations lead to the Newtonian equation of motion,

$$\frac{d^2\langle \mathbf{R}_i\rangle}{dt^2} = -\frac{1}{M_i}\big\langle \nabla_i V^{6D}\big\rangle\,, \tag{IV.2}$$

if the wavelength associated with the moving atom is small compared with the size of the interaction region. Then, the wave packet is well-localized. In such a case, it can be approximated by a Dirac δ-function whose center is placed at the classical position. This is in general the case in atom-atom scatterings. The wavelength of an atom of mass M and velocity v is [183]

$$\lambda = \frac{h}{Mv}\,. \tag{IV.3}$$

For the light H atom, classical conditions hold provided the translational energy of the atom is greater than 0.29 eV if we consider as a criterium the Borh radius. For atoms heavier than hydrogen or deuterium quantum effects in the dynamics are often negligible [113]. Even in the hydrogen adsorption/desorption dynamics, many integrated quantities that corresponds to an average over all possible initial molecular configuration can be semi-quantitatively or even quantitatively determined by classical dynamics [180].

To perform classical dynamics calculations for each atom, the Newton equations of motion,

$$\frac{d^2\mathbf{R}_i}{dt^2} = -\frac{1}{M_i}\nabla_i V^{6D}(\mathbf{R}_i, \mathbf{R}_j)\,, \tag{IV.4}$$

or the equivalent Hamilton equations,

$$\frac{d\mathbf{R}_i}{dt} = \frac{\partial H}{\partial \mathbf{P}_i} \quad \text{and} \quad \frac{d\mathbf{P}_i}{dt} = -\frac{\partial H}{\partial \mathbf{R}_i}\,, \tag{IV.5}$$

which are indeed the ones used in the present work, need to be solved.

There are many numerical integrators that can be used for this task. In the present work the Beeman algorithm [184] has been applied because of its high efficiency and accuracy. This fixed integration step algorithm is closely related to the Verlet algorithm, and as it, comes from a Taylor series expansion of position and velocity expressions. The Beeman algorithm produces identical positions as the Verlet algorithm, but uses a different formula for the velocities. Within the Beeman method, the position vector $\mathbf{R}_i$ and vector velocity $\mathbf{v}_i$ at time $t + \Delta t$ read:

$$\mathbf{R}_i(t+\Delta t) = \mathbf{R}_i(t) + \mathbf{v}_i(t)\Delta t + \frac{1}{6}[\mathbf{a}_i(t+\Delta t) + 2\mathbf{a}_i(t)]\Delta t^2 + O(\Delta t^4)\,, \tag{IV.6}$$

$$\mathbf{v}_i(t+\Delta t) = \frac{1}{\Delta t}\left[\mathbf{R}_i(t+\Delta t) - \mathbf{R}_i(t) + \frac{1}{6}[2\mathbf{a}_i(t+\Delta t) + \mathbf{a}_i(t)]\Delta t^2\right] + O(\Delta t^4)\,, \tag{IV.7}$$

where $\mathbf{a}$ is the acceleration vector. The advantage of this algorithm with respect to the Verlet algorithm is that it provides a more accurate expression for the velocities and better energy conservation. The disadvantage is that the more complex expressions make the calculation more expensive.

IV.2 Energy Dissipation Channels in gas-surface interactions

In gas-surfaces interactions, the whole substrate can serve as an efficient energy sink. There are two main channels for energy dissipation, phonon and electron-hole ($e-h$) pair excitations. The BOA assumes that there will not be any electronic excitation in the system. Phonon excitations in the molecule-surface interactions can be classically approximated by allowing the surface atoms movement, but it requires the consideration of large systems, which is computationally rather demanding. In most of the present state-of-the-art simulations, the frozen surface approximation is applied to reduce the dimensionality of the problem and thus the computational cost. Although such descriptions of reactive and non-reactive processes at surfaces have proven to be very successful to study a wide variety of systems, there is ample experimental evidence showing that

both $e-h$ pair [185] and phonon excitations do arise in gas-surface interactions [180]. Whether such energy transfers are relevant for each particular process under study is still a question that has to be answered for each specific problem.

Keeping the accuracy of a multidimensional DFT-PES for the gas-metal interaction, the energy exchange to both lattice vibrations and electronic excitations can be incorporated by combining the LDFA for electronic excitations and the GLO for phonon excitations/deexcitations as was first done in Ref. [129] to study the scattering properties of nitrogen atoms and molecules from metal surfaces. These two models, which are briefly described in this chapter, will be employed in order to study energy dissipation to the metal and the consequent effect on the dynamics.

IV.2.1 Local density friction approximation

The ample experimental evidence of electronic excitations associated to gas-surface reactions [115–123, 186] has motivated the development of many models to introduce electronic non-adiabaticity in gas-surface reactions [124, 187–192]. Among them, it is the concept of electronic friction [193–196], which can be incorporated into classical molecular dynamics simulations [124,128,129,138,197,198] with low computational cost. Particularly, the LDFA [124] offers a good compromise between accuracy and simplicity [125, 198]. This approach has already served to investigate dissipation in gas-metal elementary processes [125–129,131,137,138,193,195,198,199]. In the following the main ingredients of the model are briefly described.

The LDFA assumes that the $e-h$ pair excitations created by a moving atom interacting with a metal surface are equal to the ones created by the atom moving in a free electron gas (FEG) with the same density of that of the metal at the position of the atom. Thus, the problem to be solved is that of an atom moving in an homogeneous FEG. For such a system, the slow motion of the projectile represents such a strong perturbation for the FEG that a perturbative treatment within linear response theory is not justified. Instead, a nonlinear description of the screening that treats the interaction to all orders in the atomic charge is required.

To calculate the perturbation created in the electron gas by the moving projectile, and the subsequent energy loss, one may try to obtain the induced density as a function of time through the time-dependent Kohn-Sham scheme of the time-dependent density functional theory (TDDFT). However, based on the concept of the shift of the Fermi sphere developed by Schönhammer [200,201], Salin *et al.* [202] demonstrated that in the adiabatic limit and for the low projectile velocities, the exact time-dependent density can be obtained in a static Kohn-Sham DFT calculation of the coupled system. In this

way, the energy dissipation rate in an interacting electron gas is reduced to a simple integral involving one-electron force matrix elements between scattering states of non-interacting electrons [201]. Unfortunately, there exist practical problems to evaluate it because one needs to know the exact dynamic non-spherically symmetric projectile-electron potential and the component parallel to the velocity of the transport cross section, which is a vectorial quantity when the potential is not spherical. In fact, the only exact calculations within DFT performed for arbitrary velocities using this scheme, have been for protons and antiprotons [202]. Fortunately, for thermal and hyperthermal projectiles whose velocity is low as compared with the typical Fermi velocities in metals, the relevant physics of the projectile-electron gas interaction occurs via scattering at the Fermi surface. As a result, one obtains that the effect of electronic excitations is a mere friction force proportional to the projectile velocity v [193],

$$F_{diss} = n_0 \mathrm{v} k_F \sigma_{tr}(k_F) = \eta(n_0)\mathrm{v}\,, \tag{IV.8}$$

where $\sigma_{tr}(k_F)$ is the transport cross section or cross section for momentum transfer and n_0 is the electron gas density with the corresponding Fermi momentum k_F. One can interpret the dissipative force described by Eq. IV.8 as the result of the momentum transfer per unit time to a uniform current of independent electrons (n_0v) scattered by a fixed impurity potential, that is, the gas atom. Thus, $e-h$ pair excitations act like a friction force with a friction coefficient that reads $\eta = n_0 k_F \sigma_{tr}(k_F)$. If $\eta(n_0)$ is known, $e-h$ pair excitations can be introduced as a friction force in the classical equations of motion with low computational cost.

At this stage, the problem to be solved is the calculation of the $\sigma_{tr}(k_F)$, which depends on the scattering phase shift $\delta_l(k_F)$ at the Fermi level for the scattering of an electron off a spherically symmetric potential [193]:

$$\sigma_{tr}(k_F) = \frac{4\pi}{k_F^2} \sum_{l=0}^{\infty} (l+1)\, sin^2\left[\delta_l(k_F) - \delta_{l+1}(k_F)\right]\,. \tag{IV.9}$$

The assignment of the scattering potential is crucial for the calculation of the scattering phase shifts. The potential can be calculated self-consistently using DFT for an impurity embedded in an electron gas [203]. In this way, the model includes non-linear effects both in the medium response to the atomic potential (non-linear screening) and in the calculation of the relevant cross-section for the energy loss process. As mentioned above, this is necessary in order to correctly represent the strong perturbation caused by the slowly moving atomic particle.

The last step is to introduce F_{diss} in the classical equations of motion, which is done

for each recombining atom. Equations (IV.8) and (IV.9) show clearly that the dissipative force in the ideal case of an atom moving within an homogenous FEG depends on the electronic density of the electron gas. In the present work, in which we follow the LDFA, the friction coefficient applied to each recombining atom is that of the same atom moving in a homogeneous FEG with electronic density equal to that of the bare surface at the point $\mathbf{R}_i$ at which the atom i is located. The surface electronic density $n(\mathbf{R}_i)$ is calculated with DFT and within the same conditions as the PES. For implementation in the molecular dynamics simulation an analytical fitting expression that provides the friction coefficient as a function of the electronic density is used. Note that correlation effects between the two centers of the molecule are not considered. However, they have been shown to be minor corrections to the atomic value in the case of the H_2 molecule [204]. In this way, the classical equation of motion for each recombining atom reads,

$$M_i \frac{d^2\mathbf{R}_i}{dt^2} = -\nabla_i V(\mathbf{R}_i, \mathbf{R}_j) - \eta(\mathbf{R}_i)\frac{d\mathbf{R}_i}{dt}\,, \tag{IV.10}$$

where the first term in the right-hand side is the adiabatic force obtained from the 6D PES $V(\mathbf{R}_i, \mathbf{R}_j)$ and the second term is the electronic friction force that accounts for the low-energy $e-h$ pair excitations. Note that the indexes i and j refer to the recombining atoms.

IV.2.2 Generalized Langevin Oscillator model

In order to model the surface temperature and to take into account energy dissipation into phonons, several theoretical approaches have been developed [134, 205, 206]. In this thesis, we employ the GLO [134, 135, 207–209] model, which is a simple model that makes possible to account for energy exchange and dissipation between the incident atom or molecule and the surface, while keeping the accuracy of the 6D PES.

In GLO the emphasis is put in the local region of the surface that plays a major role in the dynamical process (the local region of the surface that will actually interact with the gas atom or molecule). The model makes a distinction between primary lattice atoms and secondary lattice atoms. The formers are the small number of atoms that directly interact with the gas and the latters refer to the remaining atoms in the surface and the bulk that provide a heat bath. A schematic representation of the GLO model is shown in Figure IV.1.

The motion of the gas-atom and adsorbate that is dictated by the adiabatic force depends instantaneously on their positions $\mathbf{R}_i$ and $\mathbf{R}_j$ with respect to the position $\mathbf{R}_s$

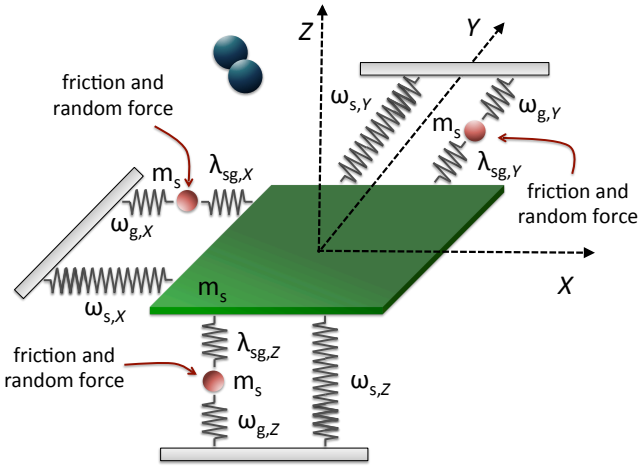

Figure IV.1: Schematic representation of the GLO model. The figure has been taken from Ref. [135].

of the moving surface:

$$\frac{d^2\mathbf{R}_i}{dt^2} = -\frac{1}{M_i}\nabla_i V^{6D}(\mathbf{R}_i - \mathbf{R}_s, \mathbf{R}_j - \mathbf{R}_s)\,. \tag{IV.11}$$

The motion of the surface is represented in terms of a 3D harmonic oscillator with coordinates $\mathbf{R}_s$ and associated 3×3 frequency matrix $\hat{\omega}_s$,

$$\frac{d^2\mathbf{R}_s}{dt^2} = -\frac{1}{m_s}\nabla_s V^{6D}(\mathbf{R}_i - \mathbf{R}_s, \mathbf{R}_j - \mathbf{R}_s) - \hat{\omega}_s^2\mathbf{R}_s + \hat{\lambda}_{gs}\mathbf{R}_g\,. \tag{IV.12}$$

This surface oscillator is coupled through the coupling matrix $\hat{\lambda}_{gs}$ to the so-called ghost oscillator, which is a second 3D harmonic oscillator with coordinates $\mathbf{R}_g$ and associated 3×3 frequency matrix $\hat{\omega}_g$ ruled by the following equation of motion,

$$\frac{d^2\mathbf{R}_g}{dt^2} = -\hat{\omega}_g^2\mathbf{R}_g + \hat{\lambda}_{gs}\mathbf{R}_s - \hat{\gamma}_g\frac{d\mathbf{R}_g}{dt} + \frac{1}{m_s}\mathbf{F}_r(t)\,. \tag{IV.13}$$

Equation IV.13 shows that the ghost oscillator is also subjected to a friction force with damping matrix $\hat{\gamma}_g$ and to a random force $\mathbf{F}_r(t)$. The latter is a Gaussian white noise source with variance $(2k_BT_s\gamma_g/(m_s\Delta t))^{\frac{1}{2}}$, where Δt is the time integration step, k_B is the Boltzmann constant and T_s the surface temperature. According to the second fluctuation-dissipation theorem, these two terms balance and the temperature in the primary zone remains constant. Therefore, the ghost oscillator is acting as a thermal bath that keeps the surface at the temperature T_s: the friction force represents the energy dissipated from the surface to the bulk, while the random force assures the energy flow

from the bulk to the surface due to the thermal vibrations of the lattice.

In both oscillators, the mass is taken equal to the mass of one surface atom, m_s, because in a first approximation the collision event happens between the atom or molecule and a surface atom. The frequency matrices $\hat{\omega}_s$ and $\hat{\omega}_g$ associated to the surface and ghost oscillators are taken equal and diagonal. Therefore, the elements of the frequency matrices and the coupling matrix are reduced to

$$(\hat{\omega}_s^2)_{\alpha\alpha} = (\hat{\omega}_g^2)_{\alpha\alpha} = 2\omega_\alpha^2 \quad \text{and} \quad (\hat{\lambda}_{gs})_{\alpha\alpha} = \omega_\alpha^2 \,, \tag{IV.14}$$

where ω_α denotes the oscillator frequencies for motion along the direction $\alpha = x, y, z$. The values are obtained from experimental or computed data as the surface phonon frequencies close to the Brillouin zone edges of the metal surface. The diagonal damping matrix $\hat{\gamma}_g$ is calculated from the Debye frequency ω_D as proposed in Ref. [207],

$$\hat{\gamma}_g = \frac{\pi}{6}\omega_D \mathbf{I} \,, \tag{IV.15}$$

where $\mathbf{I}$ is the identity matrix.

The complete description of the GLO model can be found in Refs. [134, 207]. In particular, we use the implementation made by H. F. Busnengo and co-workers [135,210].

IV.3 Computation of Observables

IV.3.1 Initial State of the Adsorbed Atoms

All the simulations are performed within quasiclassical initial conditions in which the zero point energy of the adsorbates is included in the initial conditions of the trajectories. The semiclassical rule of quantification establishes that the vibrational actions integrals for the good action variables are equal to $(v + 1/2)h$ [59, 211, 212]. The good actions correspond to the normal modes of the vibrating system, and thus, one should first calculate them. However, for simplicity, one can adopt the X, Y, and Z mode decomposition, which is shown to give very similar results [76, 77]. In this case, the following expression is applied to each cartesian coordinate:

$$\oint P_{R_i} dR_i = 2\pi(v + \tfrac{1}{2}) \,, \tag{IV.16}$$

where R_i is the coordinate (X, Y or Z), P_{R_i} the conjugate momentum of it and v the vibrational quantum number. The vibrational action is obtained by a numerical calculation within the atom-surface potential. In each coordinate, we find numerically the energy for which Eq. IV.16 is satisfied for $v = 0$, which corresponds to the component of the ZPE on that coordinate.

Within the molecular dynamics calculation, the adsorbates are given initial energies and random initial vibrational phases corresponding to the quasi-classical ZPE of each mode within the harmonic approximation, as done in previous works [48, 49, 60]. Each DOF (X, Y and Z) is picked randomly in the interval between the classical turning points. The knowledge of the position determines the momentum absolute value for each coordinate and its direction is then chosen randomly.

IV.3.2 Exit Channels

When an atom impinges a surface in which atoms are adsorbed, many different events are possible. In order to analyze the different processes, they must be identified within the code. In this work, two different initial conditions are studied. On the one hand, *ER* reaction is studied within the zero coverage limit (single adsorbate), which correspond to very low coverage conditions. On the other hand, total *abstraction* is investigated for finite coverages. Due to the different characteristics and objectives of those simulations, the possible events are differently identified.

When studying the *ER* reactivity, in the so-called zero coverage limit, where a single adsorbate is considered on the periodic surface (Chapter V and VI) the exit channels definition is inspired from the one employed by Martinazzo *et al.* in Ref. [58]. The dynamics of the trajectories is divided in two steps:

1. $t \leq t_0$: Trajectories are integrated up to the projectile's first rebound ($t = t_0$), which is defined as a sign change in the z linear momentum. At this moment, two different situations are considered depending on the interatomic distance r between the two atoms:

   - If the interatomic distance $r > r_{max}$, we consider that the projectile has become a *hot atom*. By evaluating the energy of this *hot atom*, the trajectory is identified as *meta hot atom (meta ha)* formation if the energetics allows it to leave the surface, i.e., its has a positive energy ($E_p > 0$). Otherwise ($E_p < 0$), the *hot atom* will not be able to escape the surface as long as it does not react with an adsorbate, therefore, we define it as a *bound ha*. In practice, for N_2 (H_2) a value of r_{max}=4 Å (5.3 Å) was employed.

- If $r \leq r_{max}$ the integration of the trajectory continues.

2. $t > t_0$: After the projectile's first rebound, in each integrating step the conditions described below are checked. If fulfilled, the corresponding exit channel is identified and the integration of the equations of motion finishes.

   - *Absorption*: the z coordinate of any N (H) atom gets lower than -0.5 Å (-1.4 Å). Therefore, we can distinguish two types of *absorption*, projectile's *absorption* and target's *absorption*.
   - *Reflection*: any of the atoms reaches the initial altitude of the projectile within one rebound. Therefore, we can distinguished two types of *reflection* as well, projectile's *reflection* and target's *reflection*.
   - *Hot atom*: the interatomic distance is larger than r_{max}. As well as in the first step, the energy of the projectile is checked in order to decide wether is a *bound ha* or a *meta ha* trajectory.
   - *Abstraction*: both atoms reach the initial altitude of the projectile with a positive diatom CM momentum along the surface normal (z-axis) and an interatomic distance $r < 2.2$ Å ($r < 2.5$ Å) in H_2 (N_2) *recombination*. The *ER* process occurs when the formed molecule moves definitively toward the vacuum before the second rebound of the projectile.

When studying *ER* and *HA* processes on covered surfaces (Chapter VII and VIII), the different processes are identified as follows:

1. *Absorption*: one atom enters the W(110) (W(100)) surface below $Z < -4.4$ Å (-3.9 Å) or after 1 ps of integration time the altitude of the projectile is $Z < 0$ Å. In the former case, if the atom was initially on the gas phase the trajectory is classified as projectile's *absorption* and if it was adsorbed as target's *absorption*.

2. *Reflection*: any of the atoms reaches the initial altitude of the projectile. Therefore, we can distinguished two types of *reflection* as well, projetile's *reflection* and target's *reflection*.

3. *Abstraction*: two atoms reach the initial altitude of the projectile with a positive diatom CM momentum along the surface normal (z-axis) and an interatomic distance $r < 2.2$ Å. Among the total *abstraction* channel, *ER abstraction* occurs when the projectile and target atom recombine with no rebound of the CM of the molecule after the collision between projectile and surface. Otherwise, the *abstraction* is counted as *primary HA*. Whenever the *abstraction* takes place involving two targets, it is classified as *secondary HA*.

4. *Adsorption*: after 1 ps of integration time no other exit channel is identified and the Z altitude of the projectile is $Z > 0$ Å.

The different exit channels will be quantified via cross sections or probabilities. For a given exit channel ex, the cross section σ_{ex} is defined by

$$\sigma_{ex} = \int\int_D P_{ex}(X_p, Y_p)\, dX_p dY_p\,, \tag{IV.17}$$

where the two-dimensional opacity function $P_{ex}(X_p, Y_p)$ is the probability of the exit channel for a given set of X_p and Y_p, which defines the initial position of the projectile. The integration area D is the total sampling area. In practice, the sampling area can be reduced due to symmetry. In these cases, the total sampling area D is obtained by multiplying the sampled area by a factor A accounting for the total area per adsorbate. Within the *zero coverage limit* we have focussed on *ER* reaction, which is by definition confined in a given sampling area. Thus, the *ER* cross section converges when increasing the sampling area. In the finite covered surface the coverage symmetry must be respected, thus the irreducible area or any multiple of it must be chosen. The sampling areas employed and corresponding factors A will be specified for each calculation in the corresponding Chapter.

IV.3.3 Rovibrational Quantum State of the Formed Molecules

Once the simulations are performed, it is meaningful to characterize the final rovibrational state of the formed diatomic molecules. The rotational action j_c is semiclassically calculated from the classical angular momentum L in the following way,

$$L^2 = j_c(j_c + 1)\,, \tag{IV.18}$$

from which we obtain

$$j_c = \frac{1}{2}\left[\sqrt{1 + 4L^2} - 1\right]. \tag{IV.19}$$

The vibrational action v_c is deduced from the semiclassical quantification of the action integral [59, 213] in the following way by,

$$\oint p_r dr = 2\pi(v_c + \tfrac{1}{2})\,, \tag{IV.20}$$

$$v_c = \frac{\oint p_r dr}{2\pi} - \frac{1}{2}\,. \tag{IV.21}$$

The vibrational action is obtained by a numerical calculation using the asymptotic po-

tential. Since the dynamics is simulated within the quasiclassical formalism, the obtained results for v_c and j_c are real numbers. Two different models have been use in this work in order to associate them to the quantum vibrational and rotational numbers, v and j. Here, we use the *standard binning method* (SB) to discretize the rotational number, which consists in rounding the j_c values to their nearest integers. To discretize the vibrational number, we use the *Gaussian weighting method* (GW) [214], in which each final trajectory result is weighted by a Gaussian-like coefficient such that the closer the vibrational action v_c to the vibrational quantum number v, the larger the coefficient is.

Chapter V

Eley-Rideal abstraction of Nitrogen and Hydrogen from tungsten surfaces in the single adsorbate limit: Energy dissipation effects

Energy transfer to the metal electrons, upon interaction/scattering of atoms and molecules, have been evidenced in a number of experiments, *e.g.*, in electric current measurements in Schottky diodes [115–118] or metal-insulator-metal (MIM) diodes [119–121] during exothermic reactions such as adsorption, *abstraction*, dissociation and chemisorption; in the detection of particle emission such as electrons (exoelectron emission) [186] or photons (surface chemiluminescence) [122] in exothermic reactions; in measurements of very short vibrational lifetimes of adsorbed molecules [215]; in vibrational excitations measurements in the scattering of NO (HCl) molecules on Ag(111), Cu(100) and Au(111) [123]; in vibrational relaxation measurements in the scattering of vibrationally excited NO molecules on Au(110) [123]; and in translational energy loss spectra derived from time-of flight measurements in H scattering from Au(111) [216]. Thus, the ensuing question to answer is whether such energy transfers are relevant for each particular process under study.

ER *abstraction* process has been theoretically scrutinized, but mainly under the adiabatic approximation [48, 59, 68, 70, 71, 75, 76], or only taking into account energy dissipation to the lattice phonons [51, 72, 73, 77, 217–221]. As previously mentioned in the introduction, this process is of special interest as it is usually very exothermic and, therefore, provides highly excited molecules [84, 85, 90]. The high amount of energy released in the reaction may substantially excite electrons and, consequently, be transferred to

the metal. For instance, experimental energy distribution of the formed HCl molecules from Cl *abstraction* from Au(111) [85] are not consistent with phonons excitations due to the large mass mismatch between H and Au. Besides, a theoretical study has shown that about half of the energy was released to the adsorbates [69], but part of the remaining energy loss was suggested to proceed via $e-h$ pair excitations. When it comes to low coverage conditions, projectile–adsorbate collisions are unlikely, and therefore, energy dissipation is expected to proceed mainly via electronic excitations and/or surface phonon excitations.

Within the zero coverage limit, we here investigate the energy dissipation due to both $e-h$ pair and phonon excitations in four systems with very distinct *ER* dynamics: (i) The *abstraction* of light H atoms on both W(100) and W(110) crystallographic planes, where phonons excitations are expected to be negligible [76, 77] and (ii) that of heavier N atoms in the same surfaces, where the surface motion effects are significant [71–73].

The Chapter is structured as follows. Methodology and details of the calculations are presented in Section V.1. In Section V.2, the effects of the energy dissipation on *ER* reactivity and on the final energy distribution of the formed molecules are analyzed. Finally, we conclude in section V.3.

V.1 Methodology and calculations details

The normal incidence scattering of atomic hydrogen and nitrogen off respectively H- and N-preadsorbed W(100) and W(110) surfaces is investigated within the zero coverage limit (single adsorbate), using QCT, which takes into account the ZPE of the adsorbates. Global ground-state PESs for two atoms interacting with an infinite and periodic surface have been previously constructed from DFT calculations fitted by the FPLEPS [159–161] model (see Chapter III). Details on the DFT calculations and the fitting procedure can be found in Refs. [77, 222] for H+H/W(100) and H+H/W(110), in Refs. [24, 160, 161, 175] for N+N/W(100), and in Refs. [20, 21, 160, 175] for N+N/W(110). The W(100) surface is known to undergo a structural phase transition below 200 K. In this work, only the unreconstructed (1×1) structure, which is observed at temperatures higher than 200 K [223, 224], is considered. In order to rationalize non-adiabatic effects in the *ER* *abstraction* process, molecular dynamics simulations have been performed within four different schemes:

1. BOSS: neither energy exchange with the surface phonons nor electronic excitations are accounted for.

2. LDFA: the BOSS model including the effect of $e-h$ pair excitations within the

		ZPE (meV)			adsorption site (Å)		
system	Q_A (eV)	x-	y-	z-	X	Y	Z
H/W(100)	3.07	55	33	67	1.585	0.0	1.2
H/W(110)	3.07	55	55	68	1.585	0.634	1.096
N/W(100)	7.37	11	11	29	1.5874	1.5874	0.65
N/W(110)	6.86	28	12	38	1.5874	0.0	1.155

Table V.1: Values of the adsorption energy (Q_A), ZPE along the x-, y-, z-axes, and cartesian coordinates of the most favorable adsorption sites for the H/W(100), H/W(110), N/W(100), and N/W(110) systems. The origin of the coordinate system is located on a W surface atom.

LDFA.

3. GLO: the Born-Oppenheimer moving surface approximation, which introduces energy exchange with the metal phonons through GLO.

4. LDFA-GLO: both phonons and $e-h$ pair excitations are accounted through GLO and LDFA, respectively. The combination of these two schemes allows to analyze the competition between the two energy loss channels and their possible coupling.

The initial conditions for the QCT simulations are described in the following. The adsorbed atom (target) is initially at the most favorable adsorption site with velocity and position consistent with the ZPE, which is calculated through a X, Y, and Z mode decomposition as explained in Chapter IV. The obtained/calculated ZPE values are shown in table V.1, which are in reasonable agreement with experiments [225–229].

In order to conserve the ZPE of the target before collision, the friction force starts to act when target's energy exceeds the ZPE. The friction force is then applied until the end of the trajectory. It was checked that this choice makes negligible differences with respect to turning the friction force on only when the target's energy exceeds the ZPE and turning it off when the target's energy goes below the ZPE. Similarly, turning on the frictional dynamics from $t = 0$ for the adsorbate has been found to affect marginally the results. The impinging H (N) atom starts at Z_p = 7.0 Å (8.0 Å), i.e., in the asymptotic region of the potential, with normal incidence and initial collision energies E_i that vary within the range 0.25-5.0 eV. Taking advantage of the symmetry of each system, the (X_p,Y_p) initial coordinates of the projectiles are randomly sampled in the green areas indicated in Figure V.1. Therefore, the factor A accounting for the total area per adsorbate is: $A = 4$ for H+H/W(100), $A = 2$ for H+H/W(110), $A = 8$ for N+N/W(100) and $A = 4$ for N+N/W(110). These areas differ from the ones used in previous works [71, 72, 76] because it was found that few *ER recombination* events occur for trajectories starting outside of the sampling surface area used in those works. Nevertheless, despite some quantitative differences between the present and the previous

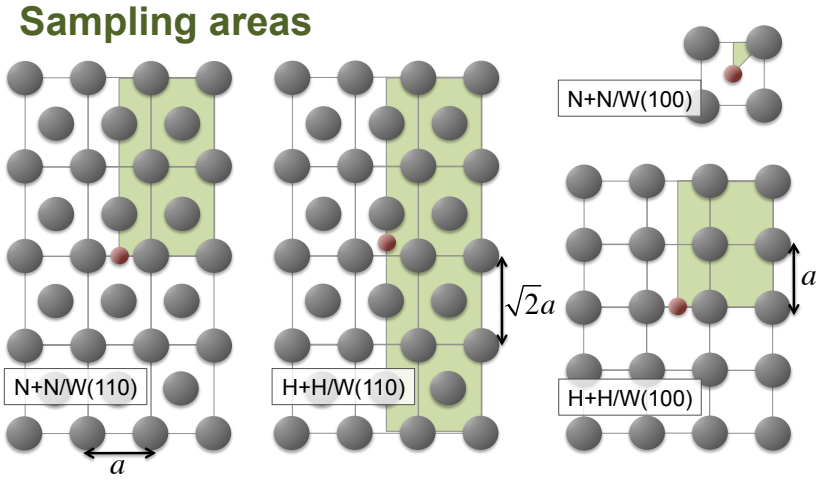

Figure V.1: Sampling of initial conditions. The target atom is in red and the green area represents the sampling area of the (X_p,Y_p) initial position of the projectile.

BOSS and GLO results, all the conclusions achieved in Refs. [71, 72, 76] remain.

For each collision energy, the number of computed trajectories was 368 000 for H+H/W(100), 864 000 for H+H/W(110), 90 000 for N+N/W(100), and 900 000 for N+N/W(110). The possible exit channels of the simulations within the single adsorbate limit are defined in detail in Chapter IV. Among them, the recombination or *abstraction* processes are considered to take place whenever both atoms reach the initial altitude of the projectile with a positive diatom CM momentum along the surface normal (z-axis) and an interatomic distance $r < 2.2$ Å ($r < 2.5$ Å) in H_2 (N_2) *recombination*. The *ER* process occurs when the formed molecule moves definitively towards the vacuum before the second rebound of the projectile.

V.2 Results

All the results shown in this section for the GLO and LDFA-GLO simulations were obtained for a surface temperature of 300 K. Simulations performed at 1500 K lead to similar results and are not shown. The computed *ER* cross sections σ_{ER} as a function of the projectile collision energy E_i are displayed in Figures V.2 and V.3 for N_2 and H_2 *recombination*, respectively. Except for N+N/W(110), the qualitative behavior of σ_{ER} with E_i is almost unchanged by including the energy dissipation channels. The largest

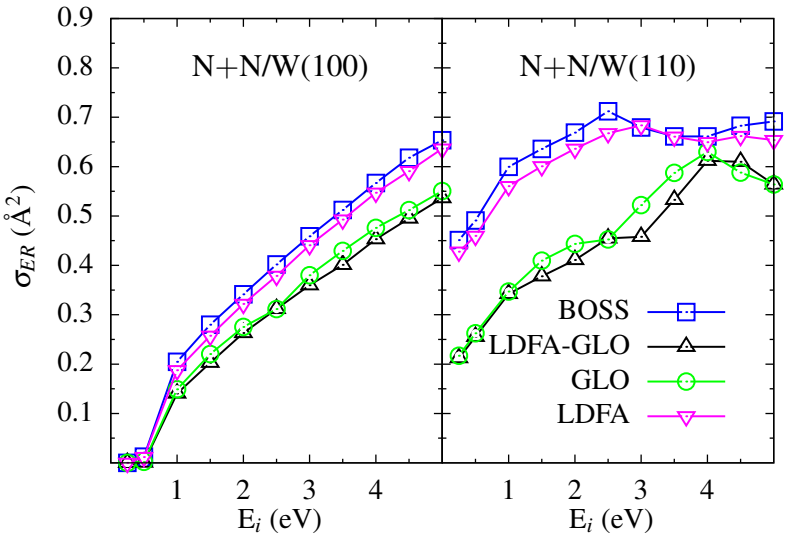

Figure V.2: *ER recombination* cross sections σ_{ER} as a function of the projectile's collision energy E_i for the BOSS (blue squares), LDFA (pink down-triangles), GLO (green circles) and LDFA-GLO (black up-triangles) simulations.

quantitative differences with respect to the BOSS results are found for N_2 *recombination*. Figure V.2 shows that surface motion is responsible for reductions in the N_2 σ_{ER} of 10-50%, while electronic friction only causes a marginal decrease of less than 7%. In the case of H_2 recombination (Figure V.3), we observe just the opposite, i.e., the main changes with respect to the BOSS σ_{ER} are due to $e-h$ pair excitations (compare either LDFA to BOSS or GLO to LDFA-GLO), while as also shown in ref [76] the role of phonons can be disregarded. More precisely, including electronic friction decreases the BOSS cross sections for the H+H/W(100) in the range of 5-21% at low energies (E_i <1.0 eV), whereas at higher energies it increases in the range of 8-22%. For H+H/W(110), the effect of $e-h$ pair excitations is only observed at low energies (E_i < 1.5 eV) with reductions in the range of 16-39%.

As a general trend Figures V.2 and V.3 reveal that the *ER* reactivity decreases with electronic friction in the range where σ_{ER} increases with E_i and increases when σ_{ER} decreases with E_i. Therefore, the effect of $e-h$ pair excitations on σ_{ER} is equivalent to shift the $\sigma_{ER}(E_i)$ curves calculated within the BOSS approximation towards smaller initial collision energies. This suggest that the role of $e-h$ pair excitation on σ_{ER} is related to the reduction of the collision energy.

The effect of the $e-h$ pair excitations for N_2 dissociation on W(110) [124,131] and on W(100) [131], as well as for H_2 dissociation on Cu(110) [124] can be also basically related to the reduction of the collision energy. For the latter system, for which the dissociation is ruled by a late activation barrier located at short distances from the surface [23], a slight reduction of the (dissociative) sticking coefficient S_0 is predicted when electronic friction

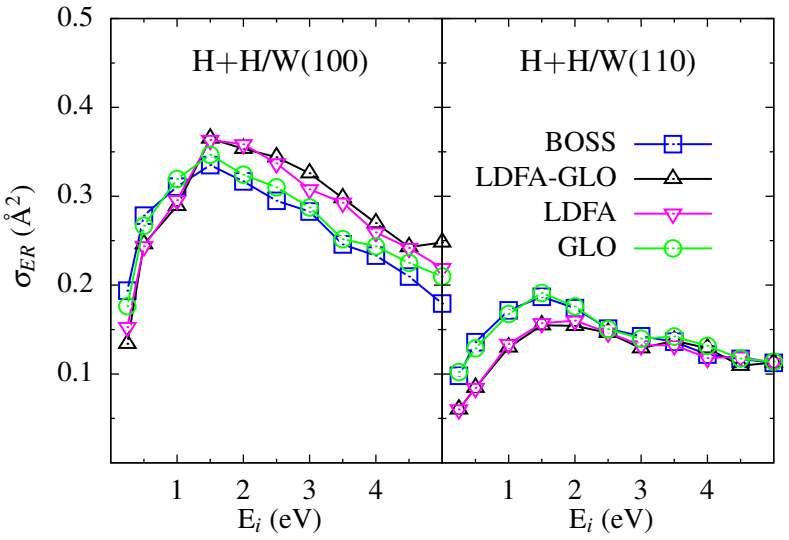

Figure V.3: Same as Figure V.2 but for H+H/W(100) and H+H/W(110).

is accounted for. This effect stems from the reduction of collision energy, which prevents a non negligible portion of the molecules to overcome the late activation barriers. In contrast, for N_2 dissociation on both tungsten surfaces, electronic friction causes in general a weak increase of S_0. The reason is that N_2 dissociation is dominated in both surfaces by early potential energy barriers lying in regions of low electronic densities. Therefore, inclusion of electronic friction hardly affects the initial collision energy before reaching the early barrier. However, once the molecules overcome such early barriers and get close to the surface, $e-h$ pair excitations contribute to enhance the dynamic trapping towards the dissociation path by slowing the molecules down.

In order to understand better the effect of each energy dissipation channel in σ_{ER}, the average dissipated energy $\langle \Delta E \rangle$ as a function of E_i obtained from the LDFA, GLO, and LDFA-GLO simulations have been analyzed. In the latter case, the contribution coming solely from $e-h$ pair excitations ΔE_{eh} is calculated for each trajectory as

$$\Delta E_{eh} = \sum_{i,n} \eta(\mathbf{R}_i) \left(\frac{d\mathbf{R}_i}{dt} \right)^2 \Delta t_n \,, \tag{V.1}$$

where the subscript i refers to the projectile and target atoms and Δt_n is the time interval at the n^{th} integration step. After averaging ΔE_{eh} over all *ER* trajectories, the average energy lost into phonons $\langle \Delta E_{ph} \rangle$ is obtained by subtracting $\langle \Delta E_{eh} \rangle$ to the total LDFA-GLO average energy loss $\langle \Delta E \rangle$.

The results for N and H *abstraction* are displayed in Figures V.4 and V.5, respectively. Comparing both figures, we observe that the energy loss due to phonon excitations is one order of magnitude higher for N_2 than for H_2 *recombination*. This is due to the

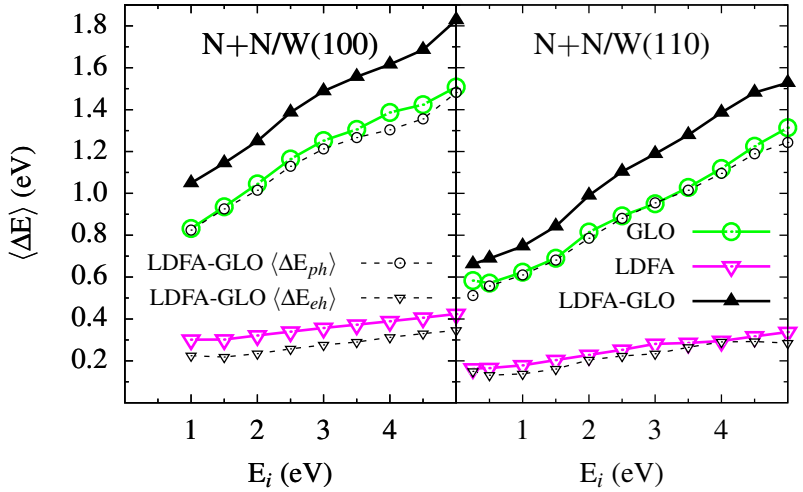

Figure V.4: Average energy loss $\langle \Delta E \rangle$ as a function of the projectile's collision energy E_i for the LDFA (pink down-triangles), GLO (green circles) and LDFA-GLO (black up-triangles) simulations. For the LDFA-GLO calculations, the average energy loss into phonons $\langle \Delta E_{ph} \rangle$ (black circles and dashed lines) and into $e-h$ pair excitations $\langle \Delta E_{eh} \rangle$ (black down-triangles and dashed lines) are also shown.

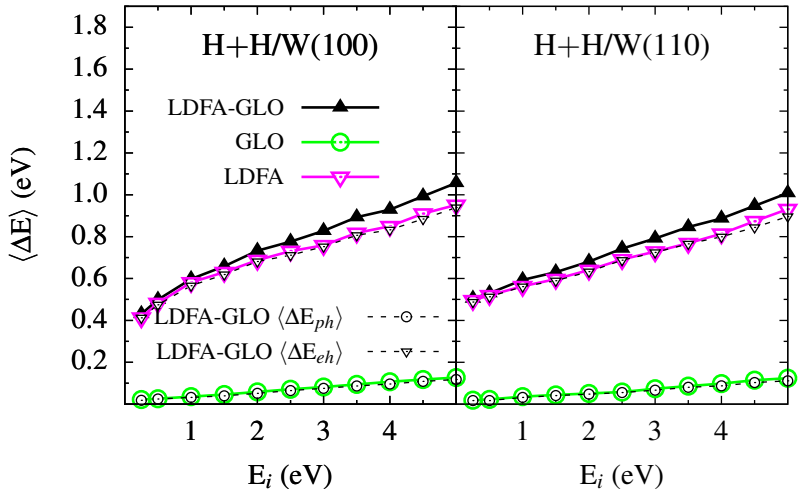

Figure V.5: Same as Figure V.5 but for H+H/W(100) and H+H/W(110).

smaller mass mismatch between N and W than between H and W. In contrast, energy dissipation due to $e-h$ pair excitations is about three times larger for H_2 recombination than for N_2 *recombination*, despite the friction coefficients at equal electron density are significantly higher for N than for H [124, 193]. There are two main factors contributing to this somewhat counterintuitive result. As shown in Table V.2, H atoms get closer to the surface and, therefore, probe regions of higher electronic density than N atoms. In addition, for similar collision energies the friction force and, hence, the electronic energy loss is larger for H than for N due to the corresponding higher velocity of the former.

E_i	H+H/W(100)	H+H/W(110)	N+N/W(100)	N+N/W(110)
1.0 eV	0.26 Å	0.58 Å	0.61 Å	1.26 Å
4.0 eV	0.24 Å	0.46 Å	0.66 Å	1.29 Å

Table V.2: Rebound altitude of the projectile for the BOSS model when E_i =1.0 eV (4.0 eV).

Focusing on the H_2 *recombination*, Figure V.5 shows that almost all the energy loss is due to $e-h$ pair excitations. An identical conclusion was recently reported for the relaxation of the *hot* H *atoms* formed from H_2 dissociation on Pd(100) [126,128,137,138].

In the case of N_2 *recombination*, however, phonons is the predominant energy loss channel as evidenced in Figure V.4. Surprisingly, though σ_{ER} experiences a higher reduction in N+N/W(110) when including the energy dissipation channels, the energy losses on N+N/W(110) are smaller than in N+N/W(100). At low E_i, on N+N/W(110) σ_{ER} is reduced in 50% when accounting for phonon excitations, whereas on N+N/W(100) a reduction of less than 25% is observed. The initial (X_p,Y_p) position of N atoms giving *ER* reaction on W(110) for the BOSS and LDFA-GLO models for E_i=1.0 eV (left panels on Fig. V.6) shows that *ER* projectiles starting at high impact parameters are highly reduced when including the energy loss channels. On N+N/W(100) (right panels on Fig. V.6), on the other hand, due to the deep adsorption site there is no reaction with projectiles of large initial impact parameter b.

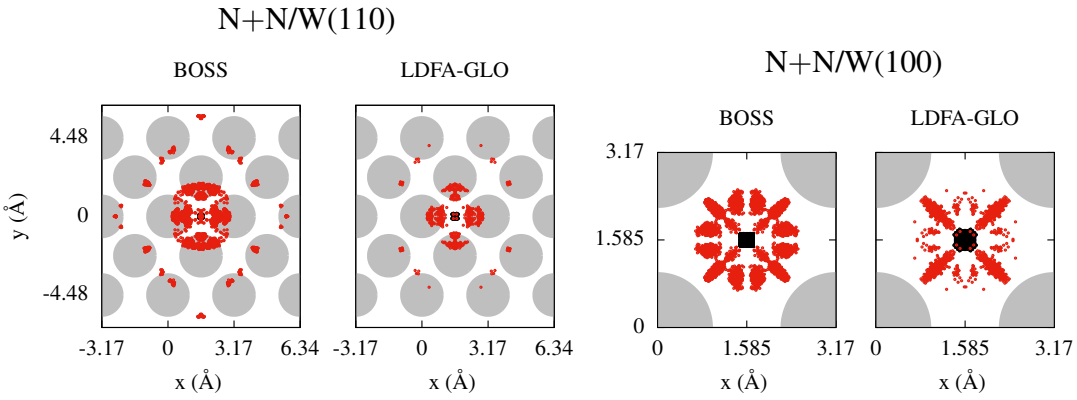

Figure V.6: (X_p,Y_p) initial positions of the projectiles leading to *ER recombination* on N+N/W(110) (left panels) and N+N/W(100) (right panels) at E_i=1.0 eV for BOSS and LDFA-GLO simulations.

An interesting feature of the energy losses in N_2 recombination that can be observed in Figure V.4 is the existence of an apparent coupling between the two dissipation mechanisms, which is not observed for H_2 *recombination*. Comparing the LDFA $\langle\Delta E\rangle$, on the one side, and the GLO $\langle\Delta E\rangle$, on the other side, to the LDFA-GLO results, we observe that the energy dissipated into either $e-h$ pairs ($\langle\Delta E_{eh}\rangle$) and into phonons ($\langle\Delta E_{ph}\rangle$) is

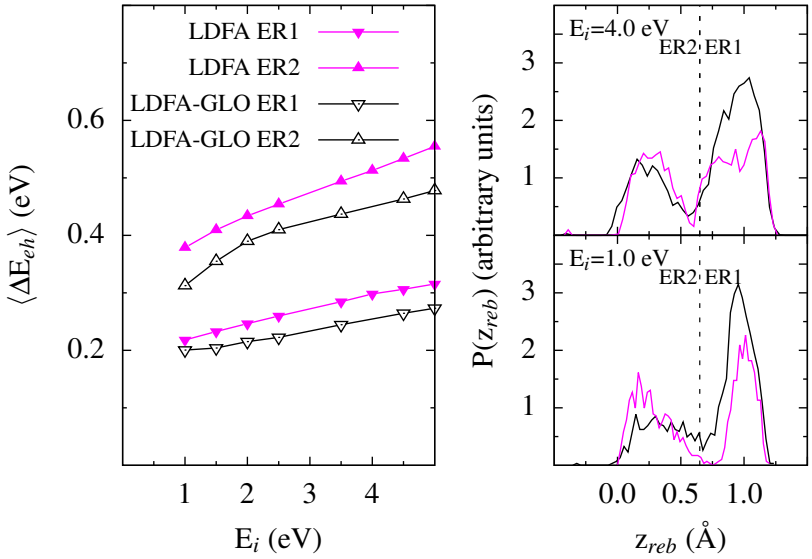

Figure V.7: Right panel: Average energy loss due to $e-h$ pairs $\langle \Delta E_{eh} \rangle$ of molecules formed via ER1 (up-triangles) and ER2 (down-triangles) as a function of the initial collision energy of the projectile E_i for the LDFA (pink) and LDFA-GLO (black) simulations. Left panel: Distribution of the projectile rebound altitude obtained from LDFA (pink) and LDFA-GLO (black) calculations.

smaller in the LDFA-GLO simulations that account for both dissipation channels. In relative terms, the largest effect is observed in the electronic dissipation channel, for which there is a reduction of ~ 0.1 eV on N+N/W(100) and ~ 40 meV on N+N/W(110) respect to the average energy loss obtained with the LDFA simulations. The existence of such a coupling between the two energy dissipation mechanisms contrasts with what it is observed not only for H_2 *recombination*, but, importantly, for other processes involving N projectiles. For instance, the competition between electron and phonon excitations in the scattering of nitrogen atoms and molecules off tungsten and silver surfaces was analyzed in ref [129]. As in the present work, it was found that dissipation to surface vibrations was the predominant dissipation channel, but at variance with our findings, the contribution of phonon and $e-h$ pair excitations to the total energy loss were shown to be basically additive.

In order to understand the reasons causing the coupling between the two dissipation channels, we analyze in more detail the differences between the LDFA and LDFA-GLO simulations for the N+N/W(100) system, for which the consequences of the coupling between the energy loss channels are clearly more pronounced. Quintas *et al.* [71] identified two distinct *ER abstraction* mechanisms for N_2 *recombination* on W(100), namely, one denoted ER1, which is characterized by a projectile rebound altitude $Z_{\rm reb}$ higher than 0.65 Å, and another denoted ER2, for which $Z_{\rm reb} < 0.65$ Å. Important to us, the authors found by comparing the BOSS and the GLO results that the ratio between

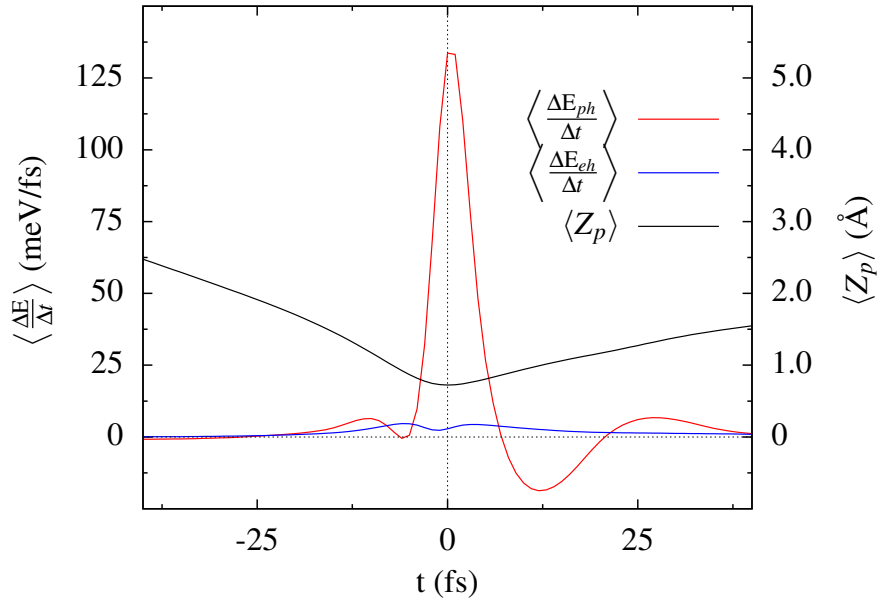

Figure V.8: Average energy loss rate of 300 *ER* trajectories due to phonons ($\left\langle \frac{\Delta E_{ph}}{\Delta t} \right\rangle$, in red) and to $e-h$ pairs ($\left\langle \frac{\Delta E_{eh}}{\Delta t} \right\rangle$, in blue). The right y-axis indicates the values of the average Z-coordinate of the projectile $\langle Z_p \rangle$ (in black).

ER1 and ER2 changes when surface motion is included. Here we find something similar when comparing the LDFA and LDFA-GLO results. The distributions of the projectile rebound altitudes for *ER* reactive trajectories are displayed in the right panels of Figure V.7 at two representative collision energies E_i = 1.0 eV and 4.0 eV. The weight of ER1 increases from 49% in LDFA to 79% in LDFA-GLO for E_i=1.0 eV (from 57% to 71% for E_i=4.0 eV). This modification will certainly contribute to a reduction in the electronic energy loss, since the molecules formed via ER1 probe surface regions of smaller electronic density than molecules formed via ER2. Nevertheless, this is not the only ingredient that causes the differences between the LDFA and the LDFA-GLO electronic energy losses. The left panel of Figure V.7 shows the average energy loss due to $e-h$ pair excitations for each mechanism within the LDFA and LDFA-GLO simulations. This figure highlights that there is already a decrease in the electronic energy loss of approx. 40 meV in each mechanism when surface motion is included. Interestingly, the reduction is similar to the one found for the N+N/W(110) system. In this case, we find that the Z_{reb}-distribution of the *ER* recombinations remains unchanged when including surface motion (not shown). Therefore, the electronic energy loss decreases more on W(100) than on W(110) because in addition there is a change in the Z_{reb}-distributions

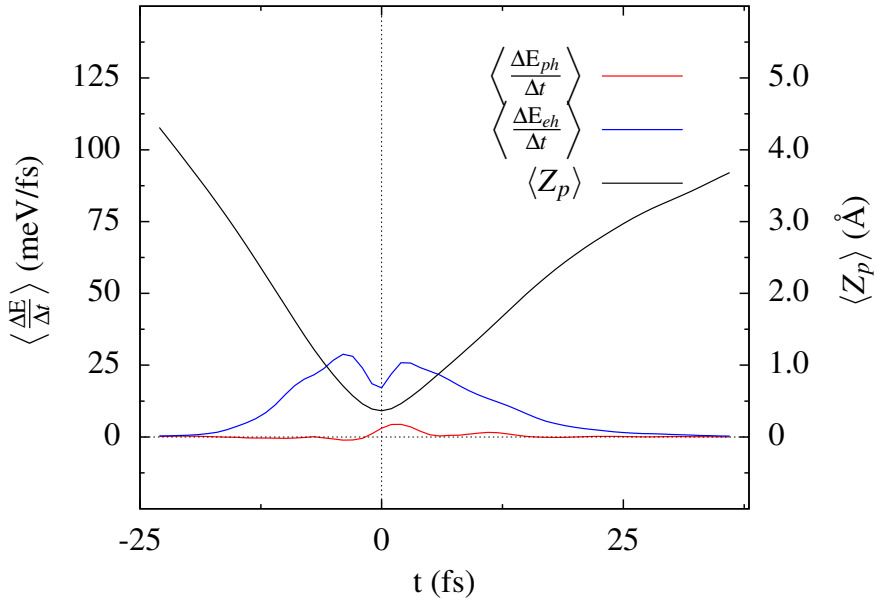

Figure V.9: Same as Figure V.8 but for H+H/W(100).

of the former. Still, the question that remains is why there is a systematic reduction in the electronic energy loss when energy exchange with the lattice is allowed.

With this purpose, we have analyzed the time evolution of each energy loss process along the *ER* trajectories. Figure V.8 displays the average energy loss rate to phonons $\left\langle \frac{\Delta E_{ph}}{\Delta t} \right\rangle$ and to metal electrons $\left\langle \frac{\Delta E_{eh}}{\Delta t} \right\rangle$ as a function of time for the N+N/W(100) system and $E_i = 1.5$ eV. For each *ER* trajectory, the energy loss rates are calculated by evaluating at each integration step Δt the contribution of each energy loss channel following the scheme explained above (see Equation (V.1) and text). The results of Figure V.8 are averaged over 300 trajectories, after setting in each case the time origin ($t = 0$) at the instant of the projectile's rebound. As shown in the figure, most of the energy dissipated into the surface lattice occurs at the classical turning point (see the large symmetric peak centered at $t \approx 0$ fs that amounts about 0.76 eV). Afterwards, the forming molecule gains and loses energy, but the energy exchange in these cases is considerably smaller. For instance, the energy gain centered at $t \approx 10$ fs is about 0.15 eV. At first sight, the electronic energy loss rate, which vanishes at the classical turning point with the z-component of the projectile's velocity, is rather symmetric around this point. The latter suggests that the surface electron density and the N atoms velocities are rather similar along the incoming ($t < 0$) and outgoing ($t > 0$) parts of the trajectory. The same analysis but for H+H/W(100) (Figure V.9) indicates that the energy loss process

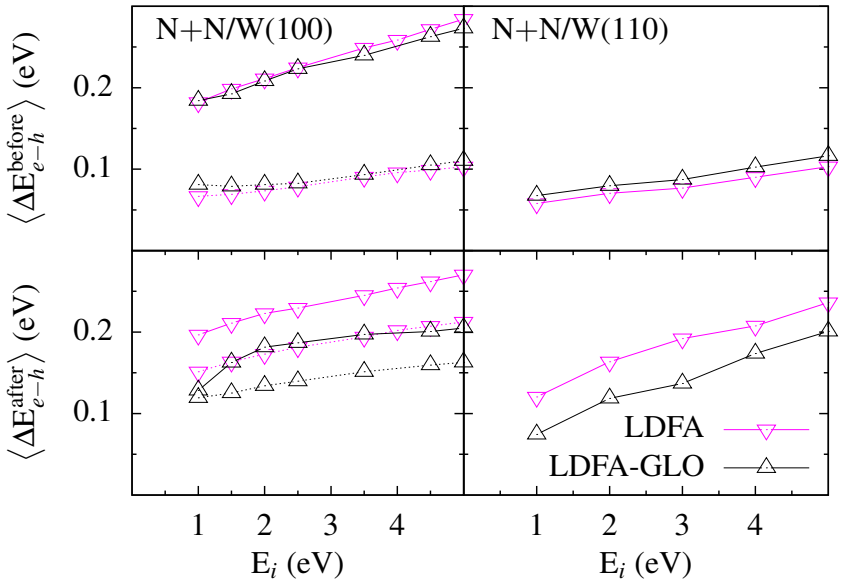

Figure V.10: Average energy loss due to $e-h$ pair excitations before ($\langle \Delta E_{eh}^{before} \rangle$, top panels) and after ($\langle \Delta E_{eh}^{after} \rangle$, bottom panels) the first collision with the surface. Left panels: results for the ER1 (solid lines) and ER2 (dashed lines) mechanisms identified in N+N/W(100). Right panels: results for all *ER* trajectories in the case of N+N/W(110). Results from the LDFA-GLO (LDFA) calculations are plotted in black (pink).

along the trajectory is rather similar regardless the system, though the efficiency of each energy loss channel changes.

Concerning the observed coupling between the two energy dissipation channels, the analysis of Figure V.8 highlights that, when phonons are accounted for, the projectile loses an important part of its kinetic energy upon the first collision with the surface. Consequently, in comparison with the static surface LDFA calculation, the electronic friction force and, correspondingly, the energy loss are expected to decrease for the remaining (outgoing) part of the trajectory. In order to confirm the latter, we show in Figure V.10 the energy loss into $e-h$ pairs of the *ER* trajectories before ($\langle \Delta E_{eh}^{before} \rangle$) and after ($\langle \Delta E_{eh}^{after} \rangle$) the first impact with the surface for N+N/W(100) and for N+N/W(110). In all cases, the differences between the LDFA and LDFA-GLO calculations only are significant after the collision event. Obviously, since both dissipation channels depend and act on the kinetic energy of the moving species, the inclusion of one affects the other. Nevertheless, we have shown here that this coupling is relatively small even when both dissipation channels are of the same order of magnitude. Otherwise, its effect will be imperceptible as found in previous works [126, 129], as well as in the present work for H_2 *recombination*.

Finally, we analyze the changes that the two energy dissipation channels may have in the internal energy of the formed molecules. The final average translational, vibrational,

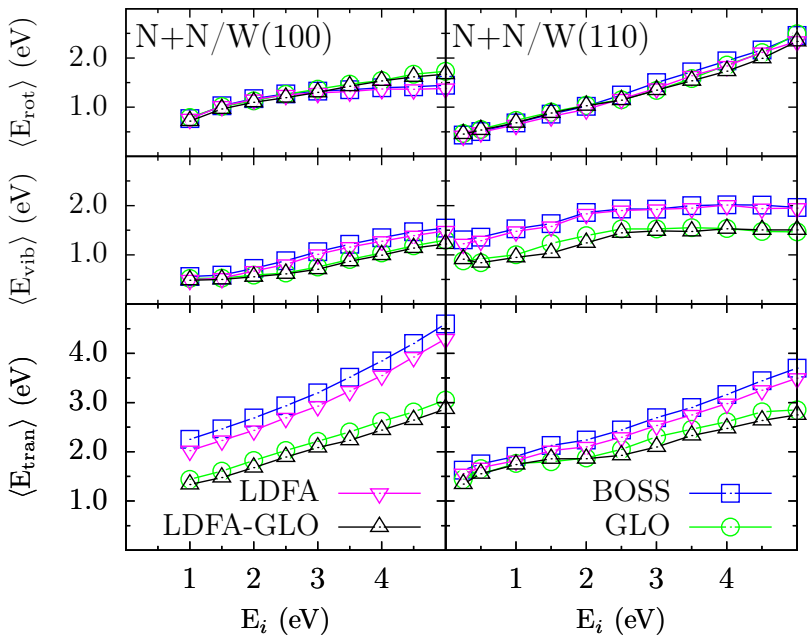

Figure V.11: Final average translational $\langle E_{tran} \rangle$, vibrational $\langle E_{vib} \rangle$, and rotational energies $\langle E_{rot} \rangle$ of the formed molecules as a function of the initial collision energy E_i: BOSS (blue squares), LDFA (pink down triangles), GLO (green circles), and LDFA-GLO (black up triangles).

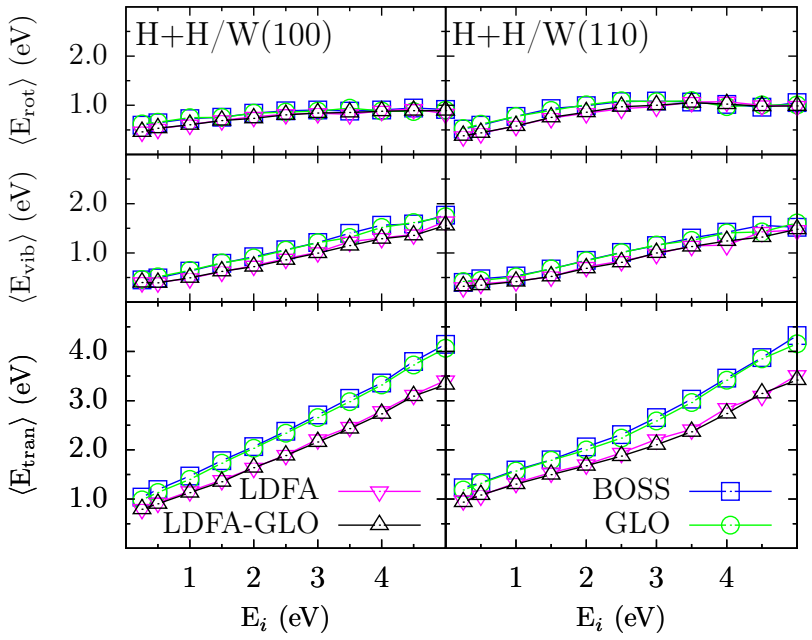

Figure V.12: Same as Figure V.11 but for H+H/W(100) and H+H/W(110).

and rotational energies of the ER-formed N_2 and H_2 are plotted in Figures V.11 and V.12, respectively, as a function of the initial collision energy E_i. As shown in Figure V.11, the largest effect on N_2 *ER recombination* are due to phonon excitations, which affect both the vibrational and the translational energy, as already discussed in ref [72]. Our new simulations that include energy dissipation into $e-h$ pair excitations show that this mechanisms causes a decrease of the translational energy only. However, such a decrease is small in comparison to the reductions caused by phonon excitations. Regarding H_2 *recombination*, Figure V.12 shows that the effect of energy dissipation into the metal electrons in the vibrational and rotational energies is very minor, but noticeable on the translational energy, which is reduced by 0.25-1.0 eV. In agreement with the results discussed so far, the effect of surface phonons is negligible in both the translational and the internal energy of the formed H_2.

V.3 Conclusions

QCT simulations have been performed to disentangle the influence of $e-h$ pair and phonon excitations on the *ER recombination* of H_2 and N_2 on the (100) and (110) crystallographic planes of tungsten. Calculations have been carried out within the single adsorbate limit under normal incidence condition in the 0.25-5.0 eV energy range. Energy transfer due to phonon excitations was described within the GLO scheme [134, 135] and $e-h$ pair excitations was modeled within the LDFA [124].

Phonon excitations reduce reactivity in the case of N_2 recombination in the range of 10-50% depending on the incidence energy and the crystal face. However, phonon excitations do not affect H abstraction due to the large mismatch between the mass of the projectile and that of the tungsten atoms. Regarding $e-h$ pair excitations the opposite behavior is observed. Whereas they have a very minor effect on the *ER recombination* of N_2, they can produce variations of the cross section for H_2 *recombination* of up to a 36%. The effect of including electronic excitations in the dynamics can be rationalized as a reduction of the effective collision energy. As a result, in the regions where the *ER* cross sections increase (decrease) with energy, electronic excitations reduce (enhance) the *recombination* probability.

Energy exchanged between the molecule and the metal have been also evaluated separating the contributions of each of the dissipation channels. Whereas energy loss due to $e-h$ pair excitations is about three times larger for H_2 *recombination* than for N_2 *recombination*, energy loss due to phonons is an order of magnitude larger for the latter than for the former. Although phonons are the main energy loss channel for N_2 formation, a non negligible effect of electronic excitations is observed. However, in

the case of H one can safely neglect any effect related to phonon excitations. Finally, the effect of energy losses in the final energy distribution in the DOF of the molecules is analyzed. The $e-h$ pair excitations mostly reduce the translational energy of the molecules, whereas phonon excitations (only significant in the case of N_2 recombinations) also affect the vibrational energy.

All in all, the description of the *ER* process is here refined by including dissipation channels in the dynamics. In the case of H_2 *recombination*, due to its light mass, it is enough to incorporate $e-h$ pair excitations and that surface movement can be neglected. On the contrary, for N_2 *recombination*, phonon excitations is the dominant mechanism, though a noticeable effect of the electronic excitations is also obtained.

Chapter VI

Eley-Rideal abstraction of Nitrogen and Hydrogen from tungsten surfaces in the single adsorbate limit: Stereodynamical effects

Since the *ER abstraction* is ultrafast (subpicosecond time scale) and involves only one rebound of the projectile, the surface might be thought to act as a spectator and consequently play a minor role in the reaction. This is definitely not the case as significant crystallographic anisotropies were revealed, in particular for N_2 *recombination* on W(100) and W(110) [73] for which corrugation is important. As a consequence of such corrugation, stereodynamical effects, i.e., sensitivity of the dynamics on the initial orientation of the colliding partners, might be anticipated. The initial orientation of the average metal-adsorbate bound with respect to the impinging atom initial momentum might be changed by varying the incidence angle. While the beam incidence angle did not lead to any sizable change of the reaction rate constants on H(D) atom reaction with adsorbed D(H) on Pt(111) [83], it was shown to greatly influence the CO oxidation by atomic oxygen on Pt(111), Ir(111), and Ru(001) [230]. Besides, for the *recombination* of NO molecules from N oxidation on O-covered Ru(0001), scattering angles of the diatom were shown to negligibly depend on the incidence angle. For H_2 *recombination* on Cu(111) [55, 59] and C oxidation on O-covered Pt(111) [91] the incidence angle slightly affects reactivity but significantly influences the final energy distributions of the formed molecules.

Although, many studies have analyzed H–H and N–N *ER* reactions on W [11, 56, 61, 71–73, 77, 78, 78, 80, 141–143, 231–234], none of them have focussed on the effect of

the incidence angle of the scattering atom. The stereodynamics of *ER abstraction* in H_2 and N_2 *recombination* on W(100) and W(110) is here studied. The organization of the Chapter is as follows. Section VI.1 gives details of the PESs and QCT simulation methodology. Results from the dynamics simulations are discussed in section VI.2. Stereodynamics influence on reactivity, energy dissipation to the metallic surface and energy distribution of the formed molecules is analyzed. Section VI.3 summarizes and concludes.

VI.1 Calculation details

Off normal incidence scattering of atomic hydrogen and nitrogen off H- and N-preadsorbed W(100) and W(110) surfaces is investigated within the zero coverage limit (single adsorbate). QCT are used relying on the same global FPLEPS PESs investigated in the Chapter V. The methodology for molecular dynamics simulation at normal incidence [80] has been detailed in Chapter V so that only the main lines are recalled here.

In order to rationalize non-adiabatic effects in the *abstraction* process, simulations are performed within two different schemes, namely, BOSS scheme in which neither energy exchange with the surface phonons nor electronic excitations are accounted for, and the LDFA-GLO scheme that includes the effect of $e-h$ pair excitations within the LDFA and energy exchange with the metal lattice within GLO as detailed in Chapter IV.

The initial conditions for the QCT simulations are the following. The adsorbed atom is initially located at the most favorable adsorption site with velocity and position consistent with the ZPE (see Table V.1), computed through a Z, Y, and Z mode decomposition (see Chapter IV). The adsorption sites for H and N on both W surfaces are illustrated in Figure VI.1 (up). As done for normal incidence conditions in Chapter V, the friction acts only when the target energy exceeds the ZPE in order to conserve the ZPE before collision. The friction force is then applied until the end of the trajectory. The impinging H (N) atom (projectile), starts at Z_p = 7.0 Å (8.0 Å), i.e., in the asymptotic region of the potential, with initial collision energies E_i that vary within the range 0.1-5.0 eV. The direction of the projectile initial velocity, v_i, is defined by θ_i, the polar angle with respect to the surface normal and ϕ_i, the azimuthal angle with respect to the x-axis. θ_f and ϕ_f are the corresponding quantities describing the direction of the final velocity, v_f, of the formed diatom. The coordinate systems are depicted in Figure VI.1 (down). For H *recombination* on W(100), incidence angles defined by θ_i=40°, 80° with ϕ_i= 0°, 45° and 90° are investigated. For N *abstraction* on W(100), due to higher symmetry, only θ_i=40°, 80° with ϕ_i= 0°, 45° are considered. Finally, for H and N *re-*

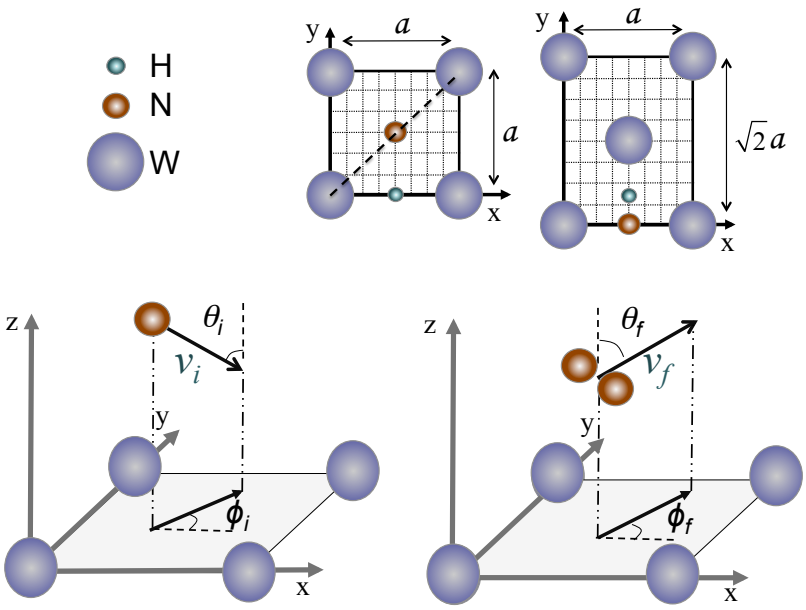

Figure VI.1: Up: adsorption sites for H and N atoms on W(100) (left) and W(110) (right)) crystal surfaces. W atoms are purple, H atoms are blue and N atoms are red. Down: Coordinate systems defining the incidence of impinging atoms and scattering of the formed diatom.

combination on W(110), θ_i=40°, 80° with ϕ_i= 0°, 54.74° and 90° incidence angles are scrutinized. The results of the dynamics for these off-normal incidences are compared with the results for normal incidence discussed in Chapter V.

The possible exit channels for the dynamics simulation are defined in detail in Chapter IV. We here focus on ER *abstraction* process, which is assumed to occur when the formed molecule moves definitively towards the vacuum before the second rebound of the projectile. Taking advantage of symmetry for each system and incidence, the (X_p, Y_p) initial coordinates of the projectiles are randomly sampled in areas that ensure projectiles rebounds in the vicinity of the target. The sampling areas were varied until *ER* cross sections were converged. A sampling density of 8444 trajectories/Å^2 was used to ensure good statistics.

VI.2 Results

VI.2.1 Eley-Rideal reactivity

The computed *ER abstraction* cross sections, σ_{ER}, are displayed in Figure VI.2 for N_2 *recombination* from W(100), as a function of the projectile collision energy E_i for the different incidences.

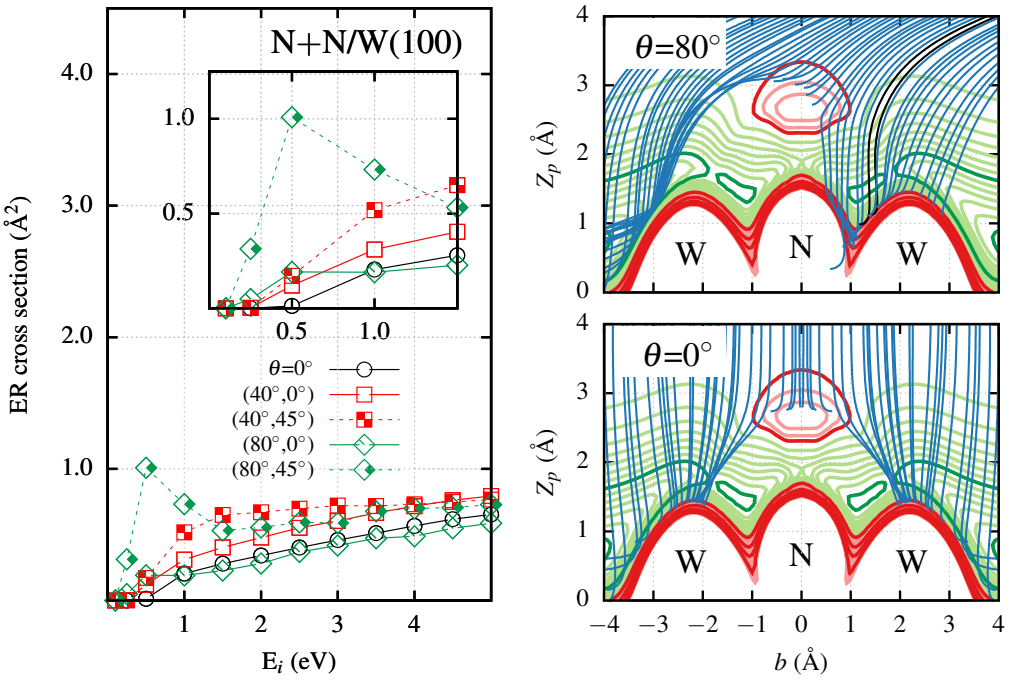

Figure VI.2: Left: *ER abstraction* cross sections, σ_{ER}, as a function of the projectile collision energy E_i for N+N/W(100). The incidence angles (θ_i,ϕ_i) are indicated. Right: Projections of relevant projectile trajectories on the ϕ_i=45° plane for θ_i=0° (down) and θ_i=80° (up) down to the first rebound. Black (Blue) trajectories are (non) reactive. Green (red) contour levels are negative (positive) separated by 0.5 eV (0.2 eV). Zero potential energy is defined for the target at the bottom of the adsorption well and the projectile at 8 Å from the surface.

A significant effect of incidence is evidenced at low collision energy. Normal incidence N *abstraction* reactivity was previously found to involve a significant 0.53 eV collision energy threshold despite the existence of nonactivated reaction pathways [73]. Such a threshold was attributed to a dynamical effect, resulting from an interplay between the entrance channel N–N repulsion and the strong attraction of the projectile towards the top W surface atoms. Figure VI.2 (left and inset) reveals that the normal incidence threshold is drastically reduced, from 0.53 eV at θ_i=0° to ∼0.1 eV at θ_i=80°. In this chemical system, due to the depth of the adsorption site (Z=0.65 Å), reaction only stems from projectiles that abstract the target after bouncing on a neighboring tungsten atom. Such a mechanism involve mainly projectiles impinging the surface about a plane normal to the surface whose azimuth is 45° (dashed line in the surface unit cell of Figure VI.1(A)) [71, 73]. Projections of reactive trajectories onto that plane reveal the dynamical origin of the significant increase of reactivity at large off-normal incidence (see Figure VI.2). At normal incidence and low collision energy (E_i=0.5 eV), deflection of the impinging projectiles by the repulsive potential energy bump above the N adsorbate associated with the strong N–W attraction steers the projectile towards the neighboring empty cells, thus

preventing the impinging atoms to efficiently collide with the N-adsorbate (Figure VI.2, down right). Conversely, upon increasing the polar angle to θ_i=80°, the topology of the interactions in the entrance channel clearly redirects impinging projectiles towards the N-adsorbate (black lines on Figure VI.2, down right), thus leading to a significant increase of reactivity. This occurs mainly in the plane normal to the surface whose azimuth is 45°, in which the adsorbate and tungsten atoms lie. In this chemical system, low energy *ER* reactivity thus critically depends on the direction of incidence as a consequence of the strong corrugation of the PES in the entrance channel.

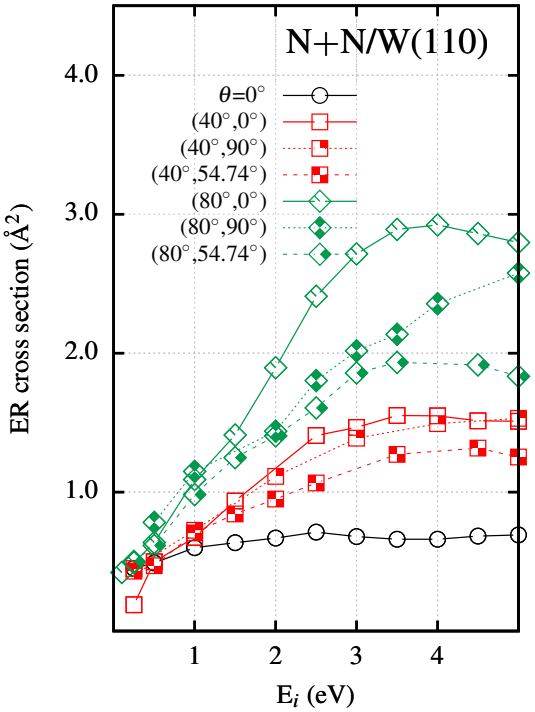

Figure VI.3: *ER abstraction* cross sections, σ_{ER}, as a function of the projectile's collision energy E_i for N+N/W(110). The (θ_i,ϕ_i) incidences are indicated.

For the W(110) surface symmetry, the N *abstraction* cross-sections significantly increase with the polar angle θ_i above E_i=1.0 eV, as displayed in Figure VI.3. For instance, at E_i=5.0 eV, the cross section increases from $\sim$ 0.7 Å^2 at θ_i=0° to $\sim$ 1.4 Å^2 at θ_i=40° (ϕ_i=0°) and $\sim$ 2.5 Å^2 at θ_i=80° (ϕ_i=0°), with a sensible dependence on the azimuthal angle. *ER abstraction* dynamics at normal and (θ_i=80°, ϕ_i=0°) incidences, for E_i=3.0 eV, are illustrated in Figure VI.4 and VI.5 respectively, where relevant reactive trajectories are plotted in the three dimensional space. At normal incidence, *ER* reactions involving projectiles boucing at impact parameter b smaller than 3.17 Å (*close-ER*, up) are discriminated from that involving higher impact parameters (*far-ER*, down). Both *close-ER* and *far-ER* contribute significantly to the total cross section, by 64% (0.43 Å^2) and 36%

(0.25 Å^2), respectively. The trajectories of the projectiles leading to *abstraction* down to the first rebound on the surface (green lines, N-approach) indicates that, at such an incident energy, projectiles impinge the surface without being steered. The large majority of the N impinging atoms first collide with W atoms prior to abstracting the N target. Only about 10% of the projectiles react upon colliding on top of the target, i.e., with an impact parameter lower than 0.75 Å and an altitude higher than the target's equilibrium altitude (1.155 Å).

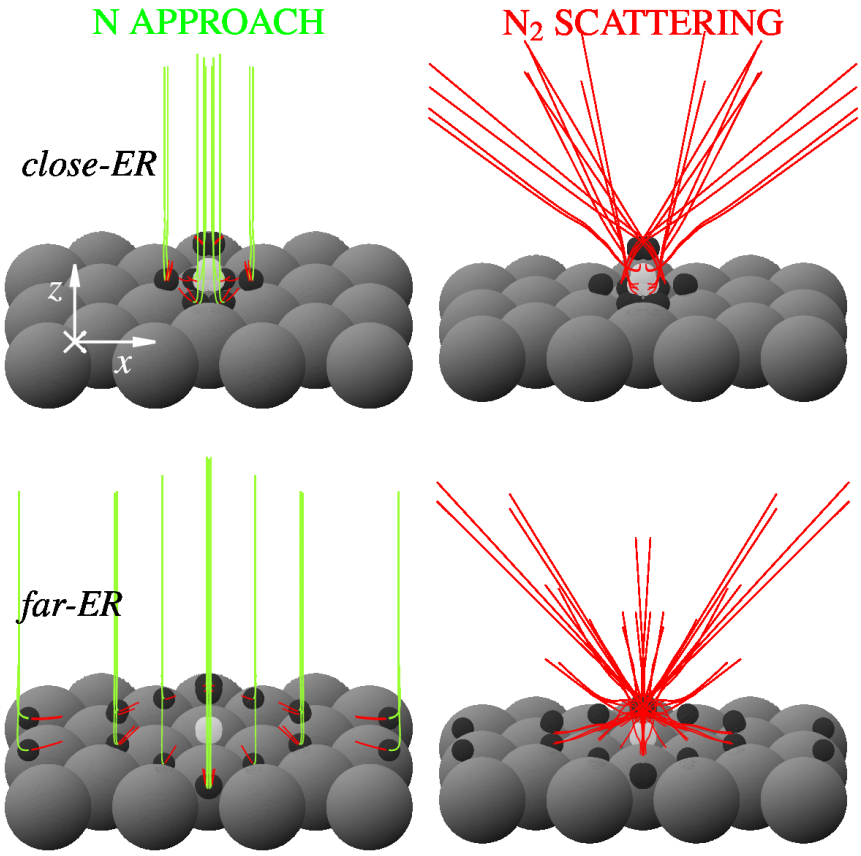

Figure VI.4: ER *recombination* of N on W(110) for an initial collision energy of 3.0 eV and θ_i=0°. Left panels: trajectories of the projectiles down to the first rebound (green lines) and during the following fs (red lines). Right panels: Diatom *CM* scattering trajectories. Gray spheres represent surface W atoms. Black (white) spheres represent the projectiles (targets) positions at the instant of its rebound..

The evolution of the trajectories during the first femtosecond after the rebound (red lines in left panels) shows that the collisions with the tungsten atoms direct the projectiles towards the target. The trajectories of the *CM* of the formed diatom (red lines in right panels) highlights that the molecules scatter off the surface in directions roughly

similar to the ones with which the projectiles are scattered from the W atoms.

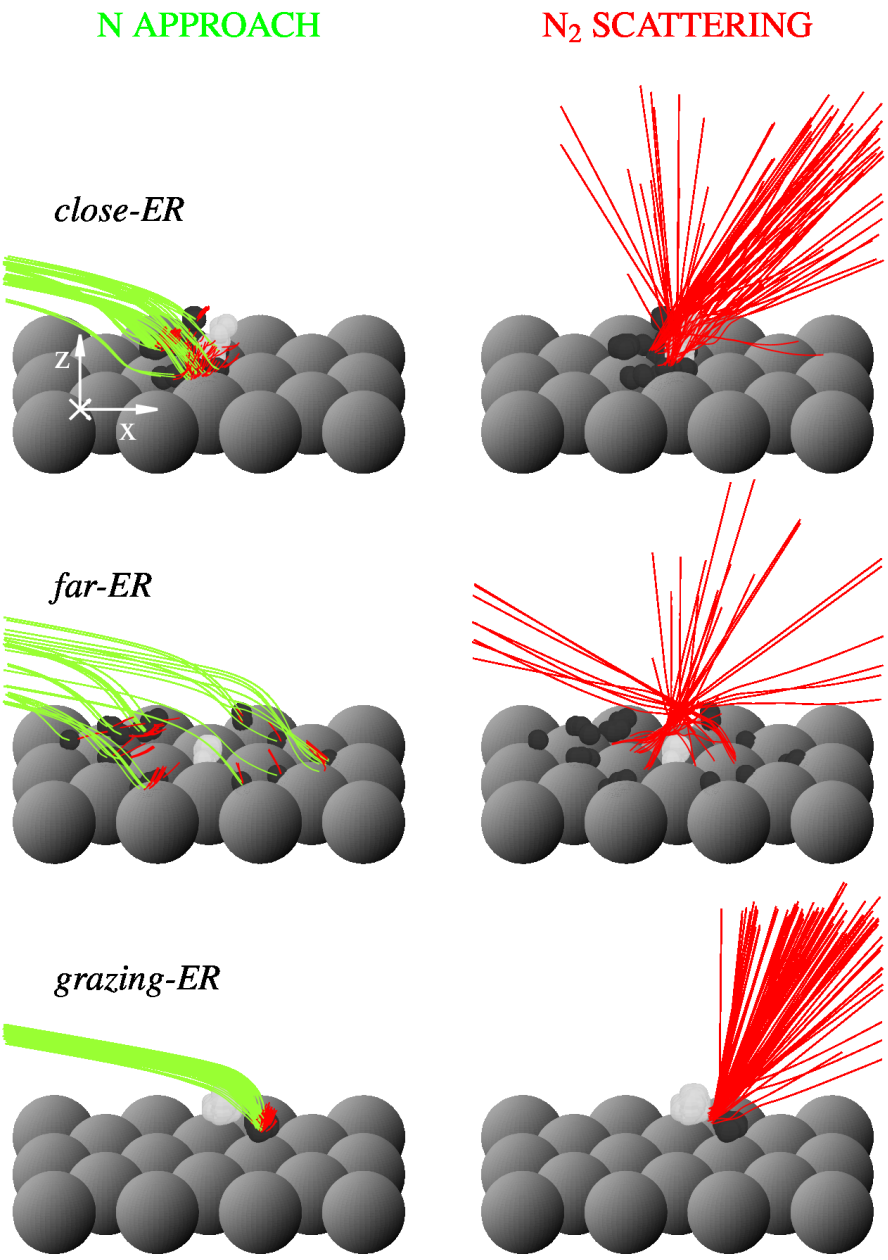

Figure VI.5: Same as Figure VI.4 but for θ_i=80° and ϕ_i=0°.

At the most reactive incidence, (θ_i=80°, ϕ_i=0°) (Figure VI.5, down) in addition to the previously discussed *close-ER* and *far-ER* mechanism, a new reaction pathway (*grazing-ER*) appears in which the projectiles are no longer directed towards the adsorbate upon colliding surface atoms. While approaching the surface the projectiles are captured by the target and then collide just on top of the next W atom following the incoming

direction. The positions of the targets at the instant of projectile's collision with the surface highlights that they have already been abstracted out of the adsorption site. This *grazing-ER* path is responsible of approx. 50% of the total *ER* cross section at this incident conditions. The contribution of *grazing-ER* to the total reactivity increases with E_i until $E_i \approx 3.0$ eV. For higher incident energies, the contribution of the three channels remains constant. *Close-ER* and *far-ER* cross sections increase by a factor of 2 with respect to normal incidence though the dynamics proceed in a similar way as for normal incidence. This *grazing-ER* path is also observed at (θ_i=80°, ϕ_i=90°) incidence, but its contribution to the total *ER* cross section is smaller representing as much as 30% of the total reactivity. Interestingly, similar mechanism was identified in the efficient N_2 *recombination* on N-covered Ag(111) [70, 235]. At (θ_i=80°, ϕ_i=54.74°) incidence, on the other hand, *ER* reaction proceeds similarly to normal incidence: molecules are mostly formed after the collision of the projectiles with W atoms that redirect them towards the targets.

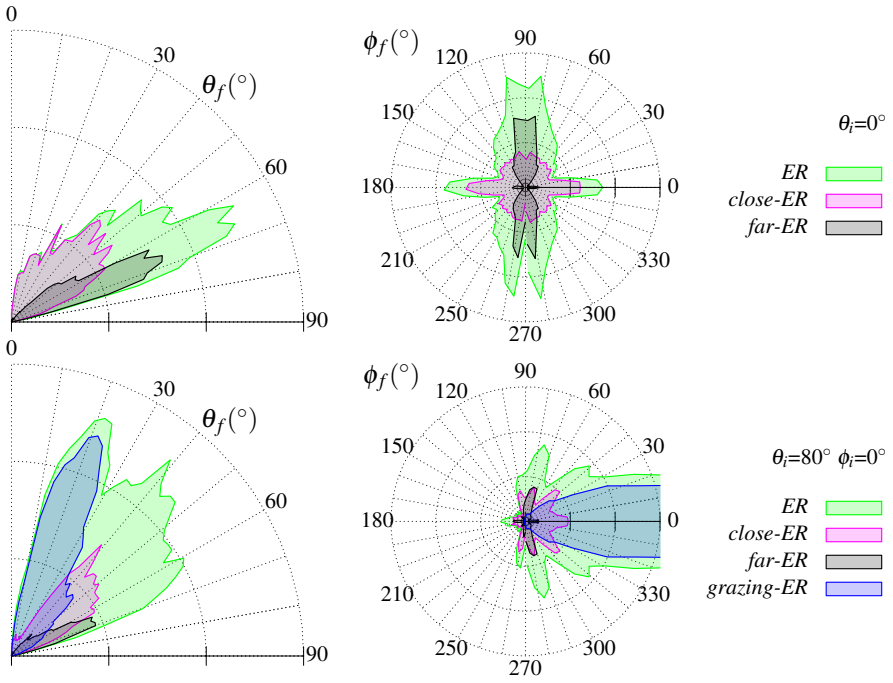

Figure VI.6: Final θ_f (left panels) and ϕ_f (right panels) angle distributions of *ER*-formed diatom (green) for E_i=3.0 eV. Angular intensities of *close-ER* (pink), *far-ER* (black) and *grazing-ER* (blue) are also represented. Top panels are for θ_i=0° incidence and bottom panels for θ_i=80° and ϕ_i=0° incidence.

Figure VI.6 displays the scattered diatom polar (left) and azimuthal (right) angle distributions for normal and (θ_i=80°, ϕ_i=0°) incidences. Since *ER* reaction occur before the incident atom reaches equilibrium with the surface, the product is expected

to retain a "memory" of the parallel momentum of the projectile, i.e., an asymmetrical angular distribution of the formed molecules around the surface normal is expected for off normal incidences. Such behavior in the angular distributions have been observed in many *abstraction* processes such as in HD *recombination* on Cu(111) [84, 90, 236] or HCl *abstraction* from Au(111) [85, 102]. In accordance, *ER*-formed N_2 molecules at (θ_i=80°, ϕ_i=0°) have a distribution of scattering polar angles around 45° with respect to the surface normal and peaked in the forward direction. Nevertheless, the larger θ_f at normal incidence highlights that the initial larger parallel momentum does not suppose higher final parallel momentum in the formed molecules. Similarly, although the NO polar angular distributions produced when Ru(0001)–O(2×1) is exposed to the nitrogen beam [237] are sharp and forward peaked, θ_f is shown to be independent of θ_i. The authors claim that the absence of a clear dependence of θ_f on θ_i is indicative of an interaction at the surface that is more complex than that of simple scattering. Indeed, this is the case also in the present work, the dependence of θ_f on θ_i comes from the dynamical changes characterised above, i.e., due to the new *grazing-ER* pathway. As

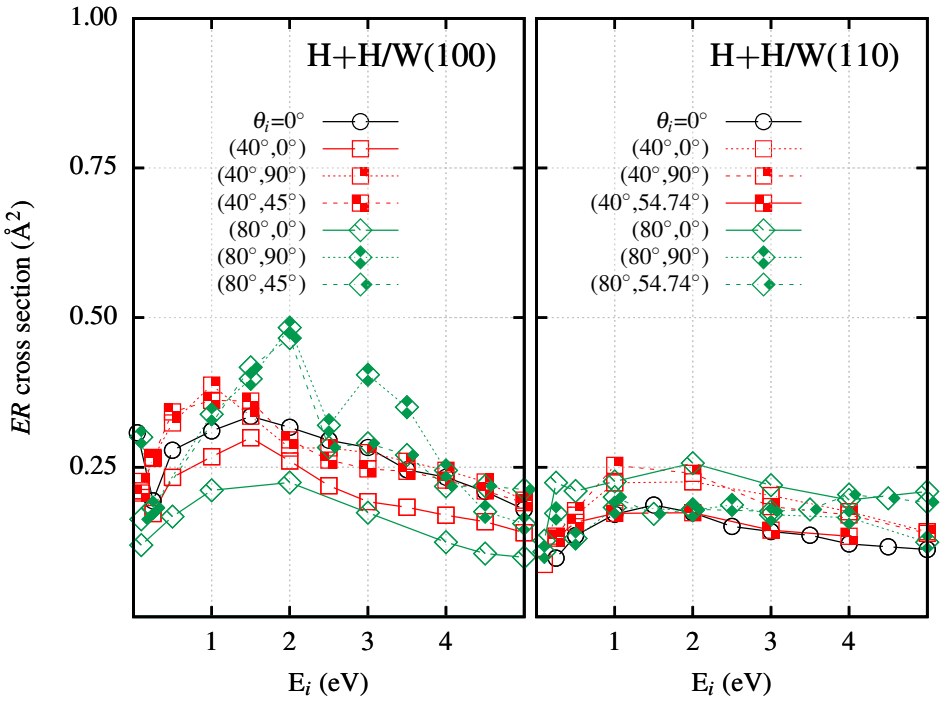

Figure VI.7: *ER abstraction* cross sections σ_{ER} as a function of the projectile's collision energy E_i for H+H/W(100) and H+H/W(110). The (θ_i,ϕ_i) incidences are indicated in each plot.

far as *close-ER* and *far-ER* are concerned, the polar distributions are not significantly dependent on the incidence conditions. Conversely, the exit azimuths reveal the signature of forward scattering [68, 69, 237]. The *grazing-ER* mechanism appearing at large

incidence involve a much narrower distribution of scattering angles close to the normal and forward direction.

In comparison with N *abstraction*, Figure VI.7 shows that much smaller quantitative changes are observed for the cross-sections of H_2 *recombination* as a function of incidence angle. Nevertheless, a slight sensitivity to the incidence angle is observed for H+H/W(100), in particular at large incidence θ_i=80°. Such a specific behavior depends on an intricate competition between two *ER abstraction* mechanisms involving rebounds of the projectile on W atoms from the surface and on the first subsurface layer [77]. Nevertheless, it does not lead to large changes in the absolute cross-sections.

VI.2.2 Non-adiabaticity

In order to quantify energy dissipation to the metal, calculations have also been carried out within the LDFA-GLO scheme, using a surface temperature of 300 K. *ER* cross sections for the BOSS and LDFA-GLO models are displayed in Figure VI.8 and VI.9 as a function of E_i for H_2 and N_2 *recombination*, respectively. As for normal incidence [80], for the rest of incidences, the qualitative evolution of σ_{ER} with E_i is only slightly affected by accouting for energy dissipation channels. Quantitative differences between both models only appear for N *recombination*, in particular for N+N/W(110), for which reactivity sensibly decreases at large off-normal angles when including dissipation.

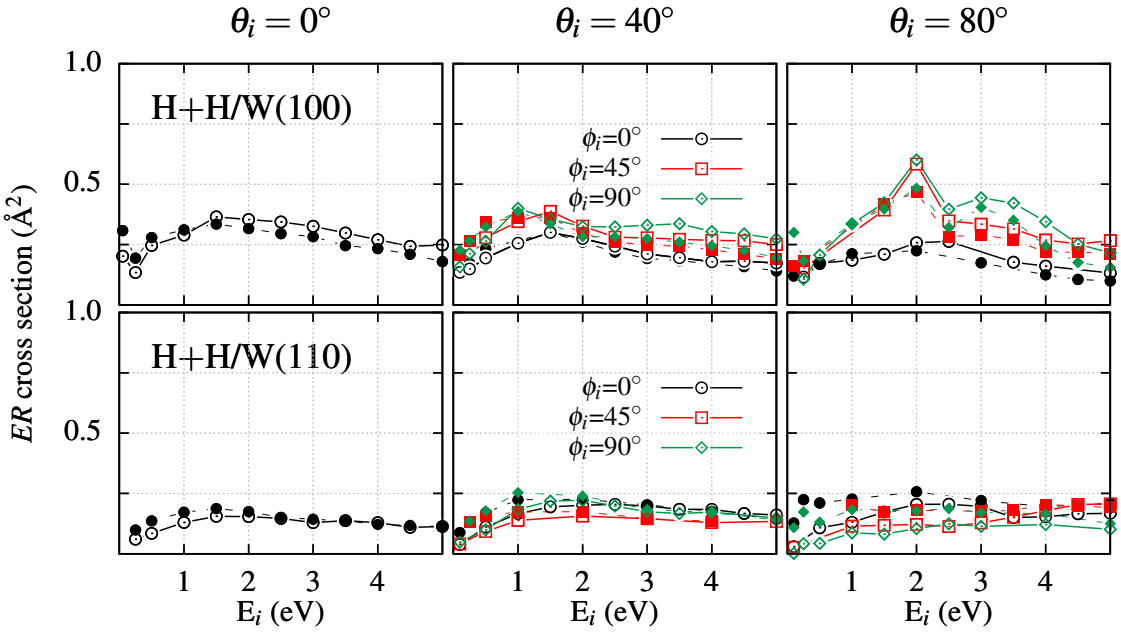

Figure VI.8: *ER recombination* cross sections σ_{ER} as a function of the projectile's collision energy E_i for the BOSS (solid symbols) and LDFA-GLO (empty symbols) simulations for H+H/W(100) and H+H/W(110). The different incidences (θ_i,ϕ_i) are indicated.

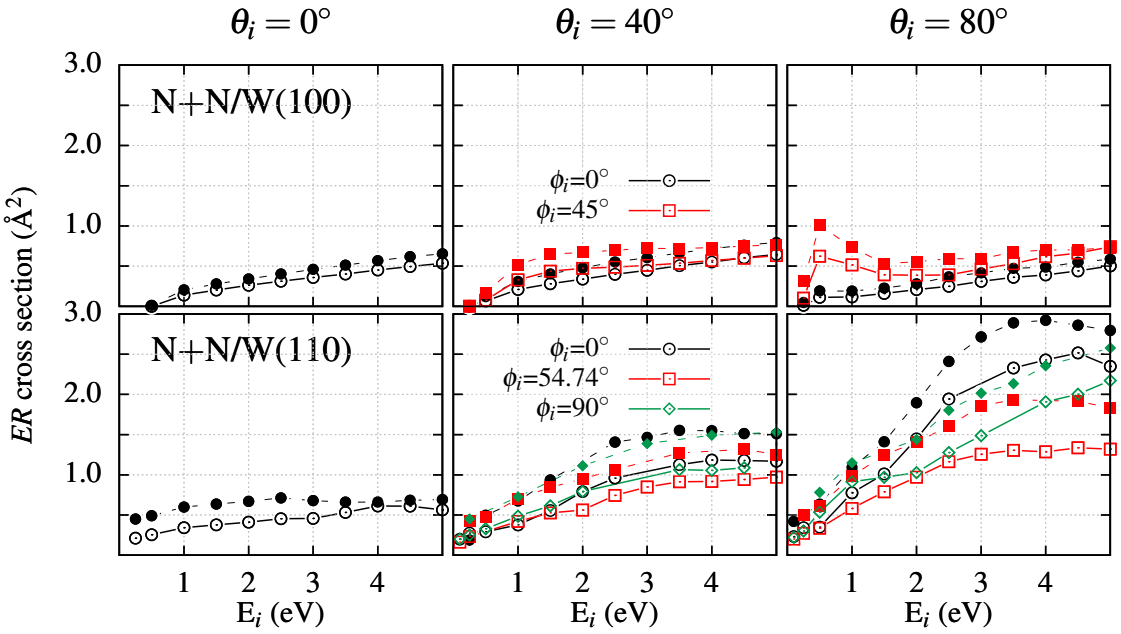

Figure VI.9: Same as Figure VI.8 but for N+N/W(100) and N+N/W(110).

The contribution of electronic excitations $\langle \Delta E_{eh} \rangle$ and phonon excitations $\langle \Delta E_{ph} \rangle$ dissipation channels to the total average energy loss to the surface $\langle \Delta E \rangle$ has been analyzed as done in previous Chapter (see Equation V.1 and text). The results for H and N *abstraction* are displayed in Figures VI.10 and VI.11 respectively. Overall, the average energy losses upon *ER recombination* of H and N on H- and N- W(100) and W(110) surfaces are within the range of 0.5-2.0 eV, increasing with E_i and do not largely depend on the incidence angle of the projectile. For all incidences and similar to what was observed at normal incidence in Chapter V, the energy loss due to phonon excitations is one order of magnitude higher for N_2 than for H_2 *recombination*. Because of the smaller mass mismatch between N and W than between H and W. Conversely, energy dissipation due to $e-h$ pair excitations is about three times larger for H_2 *recombination* than for N_2 *recombination*.

For H_2 *recombination* (Figure VI.10) negligible influence of the incidence angle on the energy loss is found. For N_2 *recombination* (Figure VI.11) the energy losses are more sensitive to the incidence angle. Nevertheless, the differences are small and very likely originated by the differentiated dynamics of each particular incidence. For instance, lower panels of Figure VI.11 highlight the lower energy loss to phonon excitation at high E_i as θ_i increases. This is in accordance with the increasing contribution of *grazing-ER* to the reactivity because in this mechanism the projectiles experience less attraction than in the rest of mechanisms. Besides, the higher influence of dissipation channels on the reactivity of N on W(110) contrasts the smaller energy losses on this system than on

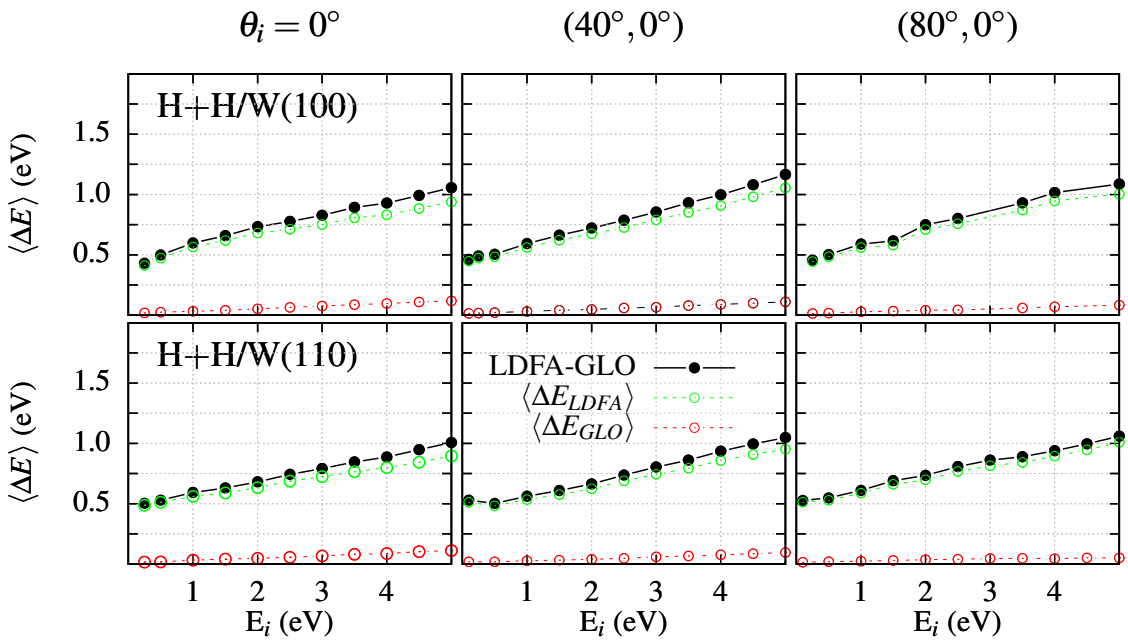

Figure VI.10: Average energy loss $\langle \Delta E \rangle$ as a function of the projectile's collision energy E_i for the LDFA-GLO (black) simulations. The average energy loss into phonons $\langle \Delta E_{ph} \rangle$ (red) and into $e-h$ pair excitations $\langle \Delta E_{eh} \rangle$ (green) are also shown.

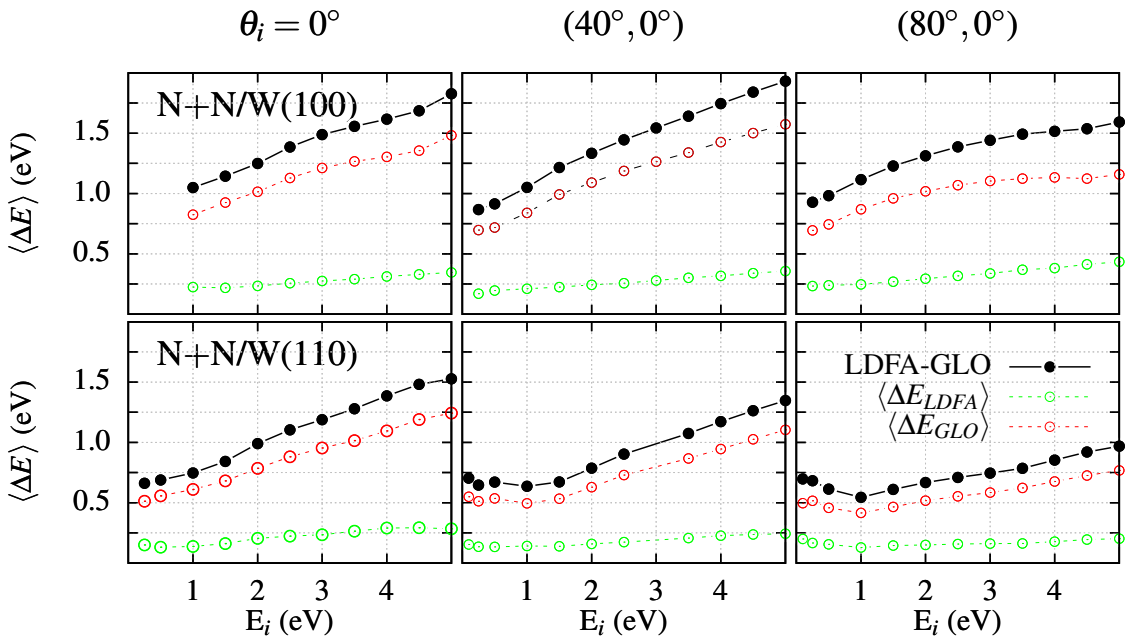

Figure VI.11: Same as Figure VI.10 but for N+N/W(100) and N+N/W(110).

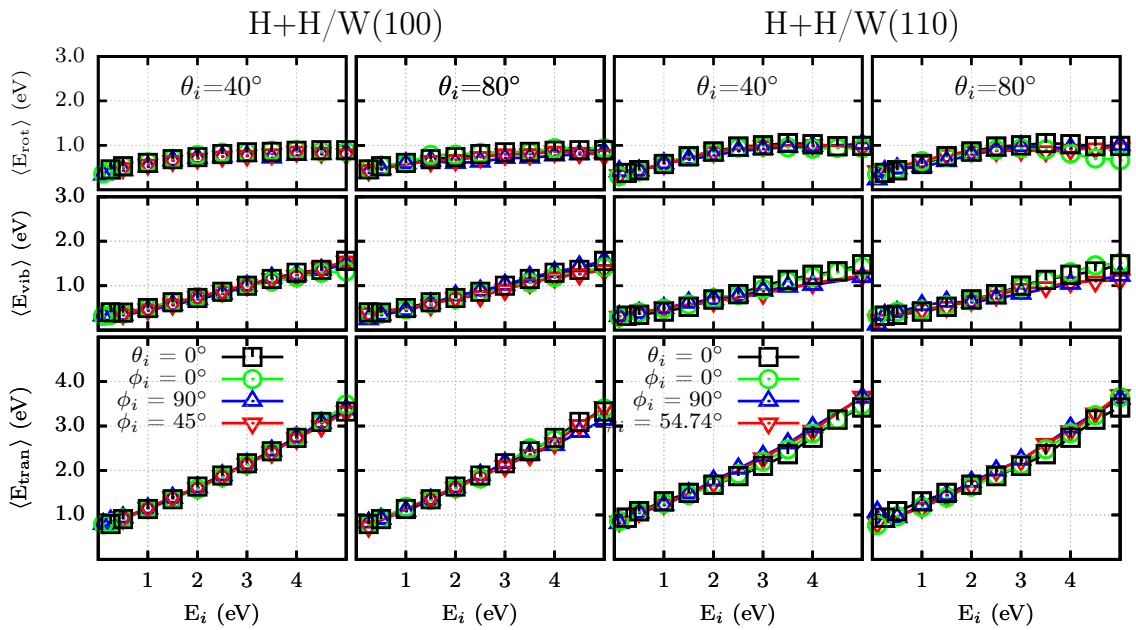

Figure VI.12: Final average translational $\langle E_{tran} \rangle$, vibrational $\langle E_{vib} \rangle$, and rotational energies $\langle E_{rot} \rangle$ of the formed molecules as a function of the initial collision energy E_i.

W(100). The reason for this is that phonon excitation as well as $e-h$ pair excitations affect more high b reactions (see Chapter V), whose contribution to the total *abstraction* is much higher on W(110). As a conclusion, as for normal incidence, the characteristics of energy dissipation to the metal depend on the chemical system. Finally, note also that for N *abstraction*, incidence angle influences the amount of energy dissipated but weakly affects its partition between $e-h$ pair and phonon excitation.

VI.2.3 Energy distribution

The influence of the incidence angle on the distribution of energy into the internal motion of the formed molecules is here investigated within the LDFA-GLO scheme. The final average translational, vibrational, and rotational energies of H_2 and N_2 are plotted in Figures VI.12 and VI.13, respectively, as a function of E_i. The dependence of the average internal energies on the incident angle for *ER*-formed H_2 molecules is negligibly small. The average internal energies of *ER*-formed H_2 molecules that were shown to be insensitive to the crystal face in Chapter V are here found to be also independent of the incidence angle.

ER-formed N_2 molecules, on the other hand, are more affected: differences as high as 0.7 eV in the internal energy distribution can be observed depending on the incidence angle (θ_i, ϕ_i) and E_i. While for N *abstraction* on W(100) the final average internal energies depends on the incidence principally at high E_i, for W(110), the distributions

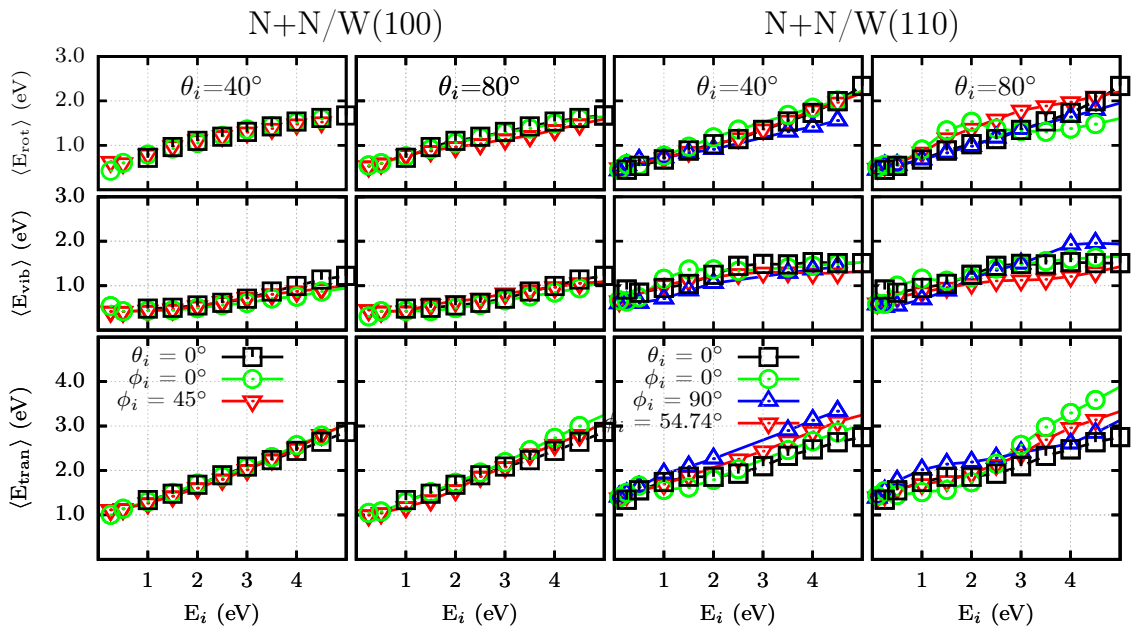

Figure VI.13: Same as Figure VI.10 but for N+N/W(100) and N+N/W(110).

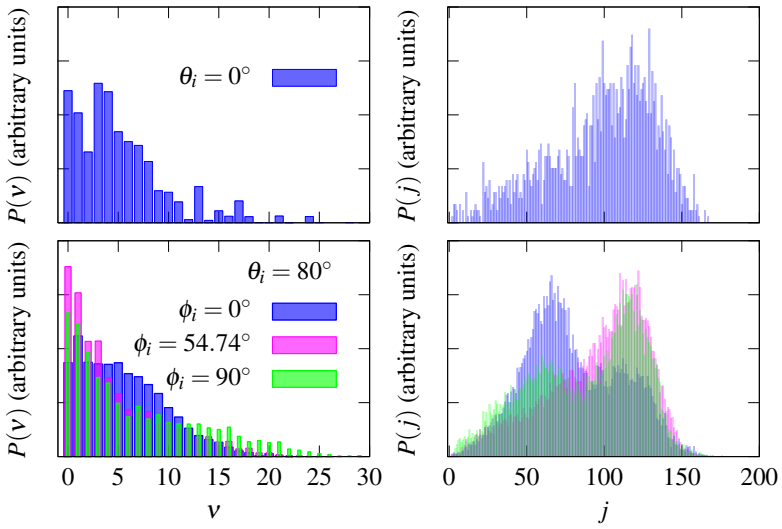

Figure VI.14: Normalised vibrational (left) and rotational (right) states distributions of the *ER*-formed N_2 molecules on W(110) when E_i=5.0 eV for θ=0° (upper panles) and θ=80° (bottom panels) incidences.

depend on the incidence for all the E_i range.

The main differences in the final energy distributions of the *ER*-formed molecules are due to the dynamical changes caused by the incidence angle that were discussed in Section VI.2.1. For instance, for N_2 *recombination* on W(110), where we identified the highest dynamical changes due to the incidence angle, the rotational state distribution is characterized by different shapes depending on the incident angle, as for E_i=5.0 eV (see Figure VI.14). The normal incidence and (θ_i=80°, ϕ_i=54.74°) incidence rotational

distributions are very similar, in the range of 0-160 j with a peak around j=125. But for (θ_i=80°, ϕ_i=0°) and (θ_i=80°, ϕ_i=90°) incidences, a supplementary peak appears at lower j. The vibrational states distributions, in the other hand, reveal a higher contribution of high ν states molecules. These distinct rotational states at (θ_i=80°, ϕ_i=0°) and (θ_i=80°, ϕ_i=90°) correspond to grazing-ER molecules, and in accordance higher peak is observed in the former incidence where the efficiency of this path is higher.

As a matter of fact, the partition of energy into the DOF of *ER* formed diatom does not depend on incidence angle for H *abstraction* on tungsten. For N_2 *recombination*, steredynamical effects are negligible for W(100) but significant for W(110) at high collision energy. These essentially originate from the large contribution to reaction of the *grazing-ER* mechanism whose dynamical pathways involve very distinct dynamics.

VI.3 Conclusions

We have investigated the effect of the incidence angle of the projectile in *ER abstraction* process. Reactivity, energy dissipation to the metal, and final energy distribution of the molecules have been analyzed. We find that the incidence angle affects much more the *abstraction* of nitrogen than hydrogen from tungsten due to the higher corrugation of the potentials in the former cases.

Non negligible quantitative changes on the reactivity are found in the four systems, at least for the highest incident polar angle. Nevertheless, high qualitative changes on *ER* reactivity are only found for N_2 *recombination*. On one side, the energy threshold for N *abstraction* fron W(100) is drastically reduced with the polar incidence angle. On the other side, very efficient N *ER abstraction* is observed at the highest θ_i due to the appearance of a new pathway, *grazing-ER*, which has been characterized in detail. The incidence angle effects have dynamical origin in N *recombination* in both crystal faces, which is related to the high corrugation of the PES on this systems.

The energy dissipated to the metal via phonon excitations and low energy $e-h$ pair excitations is analyzed as well as the effect of these two processes in the reactivity. The main conclusions of the same analysis at normal incidence (Chapter V) remain. The average energy losses upon *ER recombination* of H and N on H- and N- W(100) and W(110) surfaces are within the range of 0.5-2.0 eV, increasing with E_i and do not largely depend on the incidence of the projectile.

The partition of energy into the DOF of the *ER* formed diatom does not depend on incidence angle for H *abstraction* on tungsten. For N_2 *recombination*, stereodynamical effects are negligible for W(100) but significant for W(110) at high collision energy.

These essentially originate from the large contribution to reaction of the *grazing-ER* mechanism whose dynamical pathways involve very distinct dynamics.

Chapter VII

Non-adiabatic effects on Hydrogen *abstraction* from H-covered W(110)

H *abstraction* from H-covered W(110) has recently been studied within the adiabatic approach [78]. The authors show that *abstraction* essentially proceeds via the *HA* process at low coverage and incident energies, while as these two initial conditions increase *HA* and *ER* processes compete giving *recombination*. As in this work, to the best of our knowledge, all the theoretical studies analyzing *HA* abstraction dynamics on metals have overlooked $e-h$ pair excitations, although their influence has been experimentally suggested [136]. This issue is of prime importance as dissipation to electronic excitations, which is ubiquitous upon interaction/scattering of atoms and molecules with metals [115–123, 186, 215], might significantly affect hyperthermal motion of *hot atoms* [126–128, 137, 138], and consequently, *HA recombination*.

We here investigate the role of $e-h$ pair excitations within the framework of hydrogen *recombination* on W(110). The Chapter is structured as follows. Methodology and details of the calculations are presented in Section VII.1. Results from the dynamics simulations are discussed in Section VII.2. Finally, we conclude in Section VII.3.

VII.1 Calculation details

The normal incidence scattering of atomic hydrogen off a H-covered W(110) surface is simulated using QCT for $\Theta = 0.25$ ML, 0.75 ML and 1.0 ML coverages. The approach relies on a DFT based multiadsorbate PES developed by Pétuya *et al.* [78], in which the finite coverage potential is developed as a two-H terms expansion (see Chapter III).

The PES developed in Ref. [78] has been generalized to describe H penetration to the subsurface down to −4.4 Å (Z=0 is defined by the altitude of the topmost surface layer). QCT calculations use a 6×6 rectangular ($a \times a\sqrt{2}$) supercell with periodic boundary conditions in order to model an infinite covered surface. Thus, 18, 54, and 72 adsorbed atoms represent the Θ=0.25 ML, 0.75 ML, and 1.0 ML coverage, respectively. The classical equations of motion are integrated for one projectile atom and for the adsorbed targets.

	ZPE (meV)			*adsorption* site (Å)		
coverage Θ	x-	y-	z-	X	Y	Z
0.25 ML	47	60	71	1.585	0.6503	1.07
0.75 ML						
purple	35	47	76	1.591	0.6823	1.145
green	35	54	82	1.585	0.6923	1.216
1.0 ML	41	50	81	1.585	0.6993	1.1974

Table VII.1: Values of the ZPE along the x-, y-, z-axes, and cartesian coordinates of the most favorable *adsorption* sites for the multi-adsorbate PES at Θ=0.25 ML, 0.75 ML, and 1.0 ML coverages. The origin of the coordinate system is located on a W surface atom.

The initial conditions for the QCT simulations are the following. The targets initially sit in their equilibrium positions and are given the ZPE (see Table VII.1) as detailed in Chapter IV. Previous works [76, 78] showed that the most stable atomic *adsorption* site predicted by the PES is located very close to the threefold hollow site, in agreement with experiments. At Θ=0.25 ML coverage the adsorbates are located on this positions. However, with increasing coverage, due to the interactions between adsorbates, the equilibrium positions are slightly modified. In fact, the multi-adsorbate PES reproduces the observed surface arrangements at low temperature [225, 226, 238, 239]. The ordered p(2×2) phase is characterized for Θ=0.75 ML (Figure VII.1) but disorders at around 250 K [225, 226, 238, 239]. In accordance, the PES predicts two sub-lattices of adsorbates differentiated by purple and green atoms in Figure VII.1. The green adsorbates are surrounded by four nearest neighbors, whereas the purple adsorbates have two nearest and two next-nearest neighbors. The two kind of adsorbates adopt slightly different equilibrium positions (Table VII.1). Close to saturation, at Θ=1 ML coverage, the H atoms follow a (1×1) structure (Figure VII.1). The adsorbed H atoms exhibit a great mobility around their *adsorption* site. The structure has been qualified as a "two-dimensional quasi-liquid-like phase" by Balden *et al.* [225]. The accuracy of the multi-adsorbate PES was checked by Pétuya *et al.* [78] by performing DFT optimization calculations using the parameters previously adopted for the construction of the CRP PES [76]. Reasonable agreement was found between the multi-adsorbate PES and DFT equilibrium positions and the discrepancies in total DFT energy between both structures

were shown small (<81 meV).

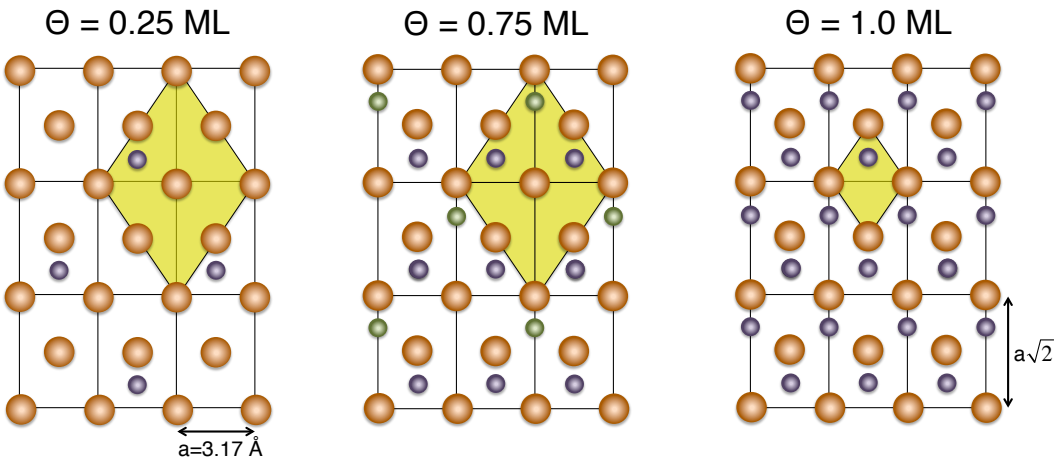

Figure VII.1: Position of the adsorbed H atoms (purple and green points) at Θ=0.25 ML (left), Θ=0.75 ML (middle) and Θ=1.0 ML (right). The lattice constant parameter is a=3.17 Å. Sampling areas of initial (X_p,Y_p) positions of the projectiles for each coverage are represented in yellow.

The initial altitude of the projectile is taken in the asymptotic region of the potential, at Z_p=7.0 Å from the surface. The (X_p,Y_p) initial position of the projectile is randomly sampled in the covered surface irreducible unit cell (yellow areas of Figure VII.1). For Θ = 0.25 ML and 0.75 ML coverages, 120 000 trajectories have been computed to ensure convergence, while for Θ=1.0 ML coverage, 30 000 trajectories were enough. Since the multiadsorbate PES ignores possible interaction between three hydrogen atoms (see eq. (III.6)), trajectories are stopped whenever one H atom has two neighboring H atoms closer than 1.5 Å. As the actual fate of such trajectories is unknown, the corresponding contribution is taken as an uncertainty to any possible outcome of scattering defined below [76–78].

In order to rationalize non-adiabatic effects upon scattering, molecular dynamics simulations are performed within the BOSS and LDFA schemes (see Section IV.2). In the former model, neither energy exchange with the surface phonons nor electronic excitations are accounted for. In the latter, electronic non-adiabaticity is introduced through a dissipative force in the classical equations of motion for the hydrogen atoms. To prevent leakage of the ZPE, the friction acts only when the energy of the preadsorbed atom exceeds the ZPE. Dissipation to surface phonons is here ignored on the ground that, as recently demonstrated [128], dissipation to electrons is largely dominating the relaxation of hydrogen on metals.

VII.2 Results

The cross sections *per* adsorbate for the most relevant exit channels are displayed in Figures VII.2, VII.3, and VII.4 as a function of the incident energy of the projectile, E_i, at Θ=0.25 ML, Θ=0.75 ML, and Θ=1.0 ML coverages, respectively. For the three coverages, the effect of $e-h$ pair excitations is to increase *adsorption* at the expense of *absorption*, *reflection* and *abstraction*. Nevertheless, the qualitative evolution of these

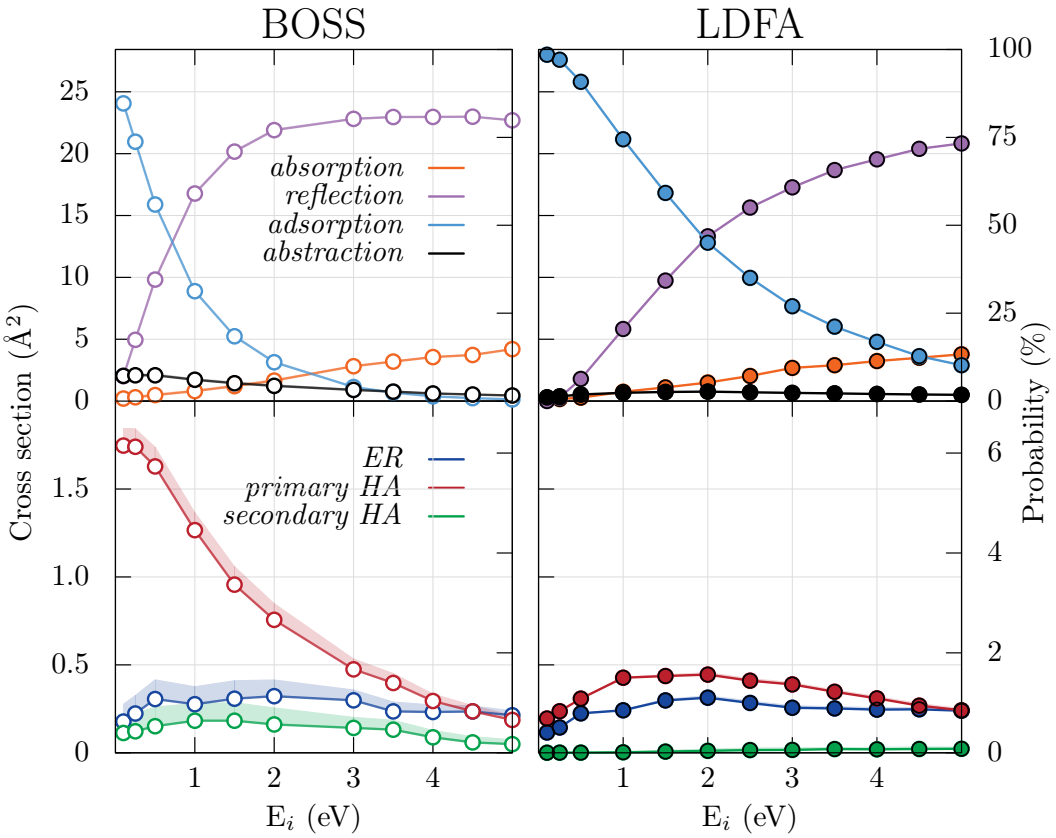

Figure VII.2: Top panels: cross sections *per* adsorbate for *adsorption* (blue), *absorption* (orange), *reflection* (purple) and *abstraction* (black) as a function of the projectile incident energy, E_i. Bottom panels: cross section *per* adsorbate for *ER* (blue), *primary HA* (red) and *secondary HA* (green) as a function of E_i. The numbers at the right axis represent the corresponding probabilities. Left (right) panels correspond to BOSS (LDFA) results. The surface coverage is 0.25 ML. Uncertainties, which correspond to the contribution of stopped trajectories (see text), are represented by shaded domains when their contribution is larger than the size of the symbols.

channels with E_i hardly changes. At low E_i, most of the projectiles adsorb on the surface whereas *absorption* and *reflection* significantly increase with E_i [78]. The reduction experienced by the *abstraction* cross section when accounting for $e-h$ pair excitations is much more pronounced for low coverage and low E_i, and as apparent from the lower

panels of Figure VII.2, mainly originates from a drastic reduction in the *HA* channels. As the coverage increases, the effect of $e-h$ pair excitations on *abstraction* becomes smaller (see Figures VII.3 and VII.4). Besides, as previously shown in Chapter V, electronic excitations slightly affects *ER abstraction*, a result that has been rationalized in terms of effective reduction of E_i in Chapter V. The already small contribution to *abstraction* via *secondary HA* decreases when including electronic excitations, particularly at Θ=0.25 ML, for which this contribution almost disappears. Overall, within the LDFA approximation *ER* and *HA* mechanisms compete whatever the coverage, but as the coverage increases *ER* becomes the dominant *abstraction* channel.

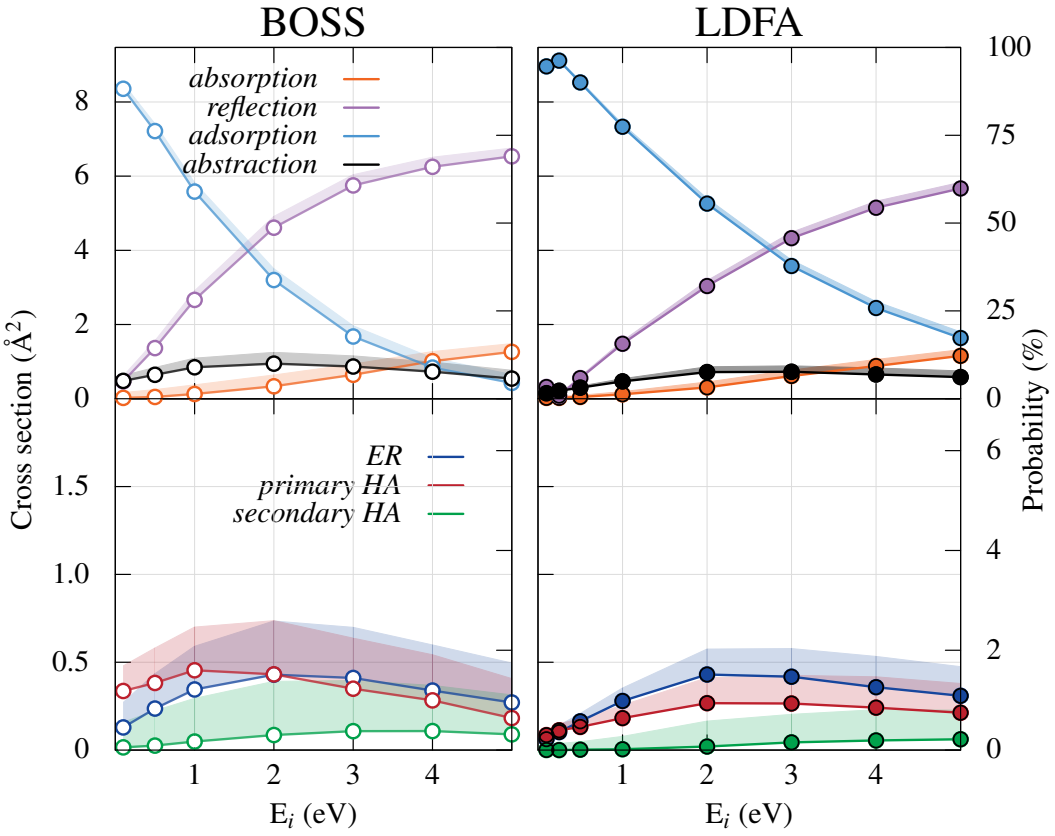

Figure VII.3: Same as in Figure VII.2 but for Θ=0.75 ML surface coverage.

To understand the significant decrease of the *primary HA* process at Θ=0.25 ML and E_i=0.5 eV, we have followed the time evolution of the total energy of the projectile, E_p, for both BOSS and LDFA simulations. At each time step E_p is calculated at the projectile position $\mathbf{R}_p$ as

$$E_p = K_p + V^{3D}(\mathbf{R}_p) + \frac{1}{2}\sum_{i\neq p}^{N} I^{6D}(\mathbf{R}_i, \mathbf{R}_p)\,, \tag{VII.1}$$

where K_p is the kinetic energy of the projectile and its potential energy is approximated

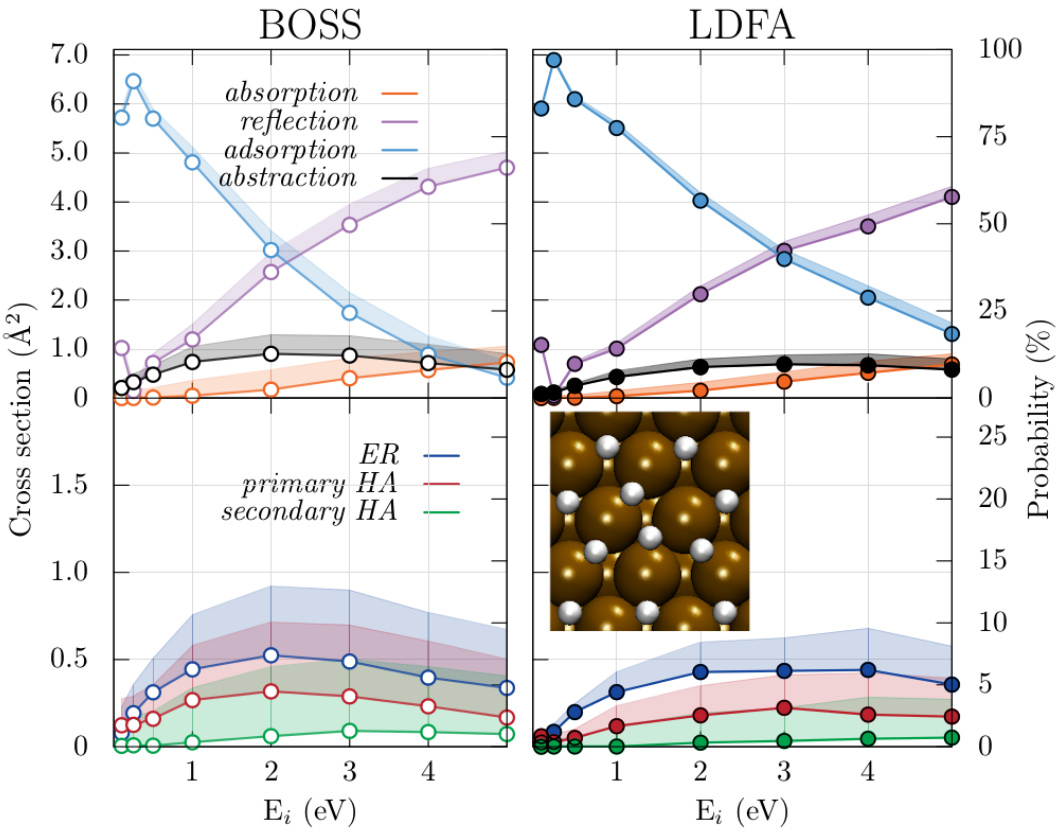

Figure VII.4: Same as in Figure VII.2 but for Θ=1.0 ML surface coverage. Inset: *adsorption* structure from DFT (see text).

as the sum of the surface-projectile atom potential $V^{3D}(\mathbf{R}_p)$ and half of the diatom interpolation potential $I^{6D}(\mathbf{R}_i, \mathbf{R}_p)$, which describes the projectile-adsorbate interaction on the surface. Figure VII.5 (right panel) displays the calculated E_p distribution and the fraction of the projectiles still traveling on or below the surface (-4.4 Å$< Z_p <$ 3.5 Å) at increasing integration times. The results are obtained in each simulation from 10 000 trajectories. In order to facilitate the implications of E_p in determining whether the projectile will permanently be trapped on the surface, the left panel sketches the potential energy diagram for the *adsorption* and *abstraction* processes (ZPEs are neglected). The origin of potential energy is chosen for the projectile at infinite distance from the covered surface and the adsorbates sitting at their equilibrium position. Both *adsorption* and *abstraction* processes are exothermic by about 3.0 and 1.5 eV respectively. The red line represents the initial total energy of the projectile with E_i=0.5 eV incident energy ($E_p = E_i$). Hence, the projectile must loss about 3.5 eV to stick in a surface three-fold site. However, *abstraction* already becomes endothermic as soon as the projectile loses about 2.0 eV, i.e., when $E_p < -1.5$ eV. Comparing the BOSS and LDFA energy loss distributions plotted in the right panel, we find that when $e-h$ pair excitations

are included in the calculation (black), 80% of the projectiles already have an energy below −1.5 eV after 0.2 ps. Consequently, these atoms cannot lead to *recombination* and adsorb. In contrast, the BOSS energy distribution shows that after 0.2 ps more than a

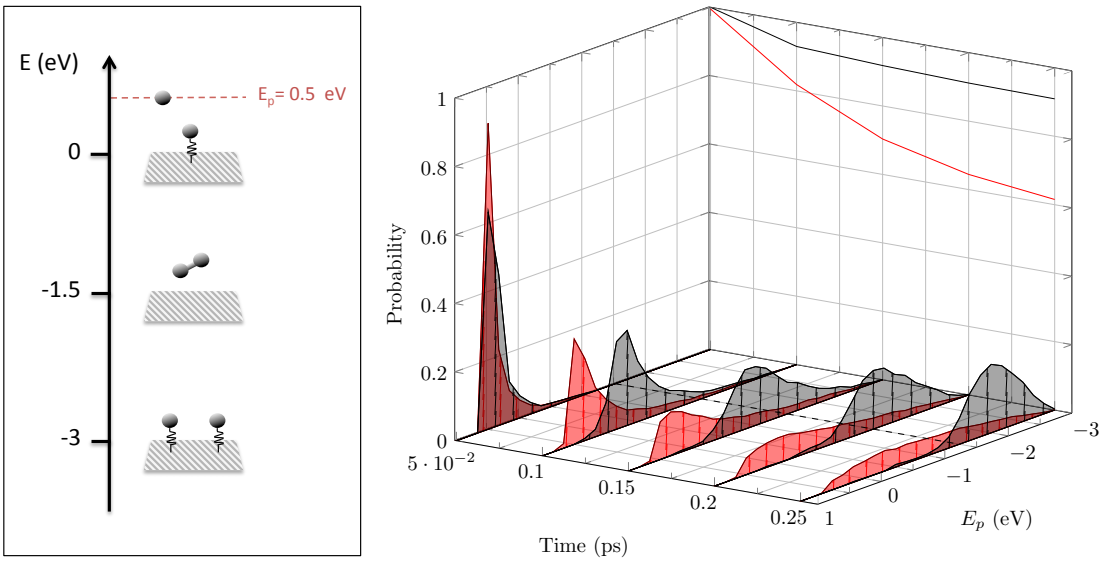

Figure VII.5: Left panel: potential energy diagram for *adsorption* and *abstraction* processes. Energies are in eV. Right panel: Total energy distributions of the projectiles travelling at the surface at different times for BOSS (red) and LDFA (black) calculations for E_i =0.5 eV and Θ=0.25 ML (left front plane, arbitrary units). The curves in the right front plane displays the fraction of projectiles located at heights -4.4 Å $< Z <$ 3.5 Å as a function of time. The dashed line ($E_p = -1.5$ eV) indicates the threshold energy below which *abstraction* becomes endothermic.

half of the projectiles still have enough energy to recombine with an adsorbate. In this case, 0.8 ps are required in order to all projectiles to loss 2.0 eV. As a consequence, at Θ=0.25 ML coverage, the energy loss due to $e-h$ pair excitations highly reduces the recombining hot-species lifetime. This is illustrated in the left panels of Figure VII.6, where the distribution of *ER* and *primary HA abstraction* times as obtained within the BOSS and LDFA simulations are displayed for the same initial condition. This time is taken as the total time for *abstraction*. When accounting for $e-h$ pair excitations, the timescale for both *abstraction* processes become really similar and, concomitantly, the distances travelled on the surface before *recombination*. Actually, the abstracted adsorbates are basically the ones initially located in the irreducible surface unit cell or in the first periodic cells (not shown). The reduction of the projectile traveled length caused by $e-h$ pair excitations is also the reason of the strong decrease observed in the LDFA *secondary HA* probabilities, in particular at low coverage. Remarkably, the influence of $e-h$ pair excitations for high E_i is less important. Right panels in Figure VII.6 show that the timescales for *ER* and *HA abstraction* processes at E_i=5.0 eV are

already quite similar within the BOSS model. Concomitantly, the influence of $e-h$ pair excitations on *HA abstraction* is as small as in ER mechanisms. Similarly, at high coverages (Θ= 0.75 and 1.0 ML) the influence of $e-h$ pair excitations is less important. Previous BOSS simulations performed at such coverages [78] already showed that the projectile energy is efficiently dissipated into the other adsorbates, resulting in a short

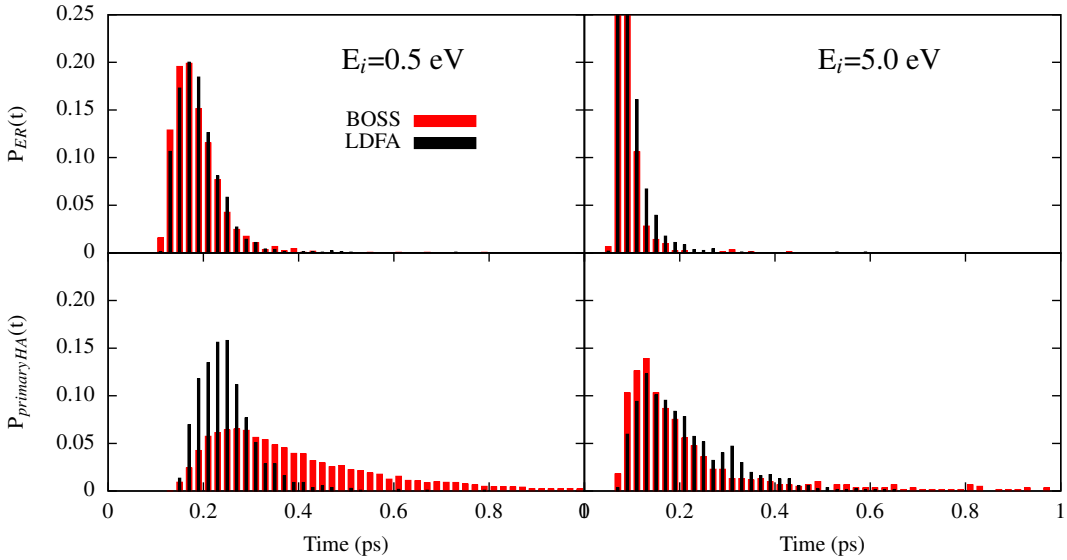

Figure VII.6: Normalized distribution of *ER* (upper panel) and *primary HA abstraction* times within the BOSS (red) and LDFA (black) simulations at 0.25 ML coverage.

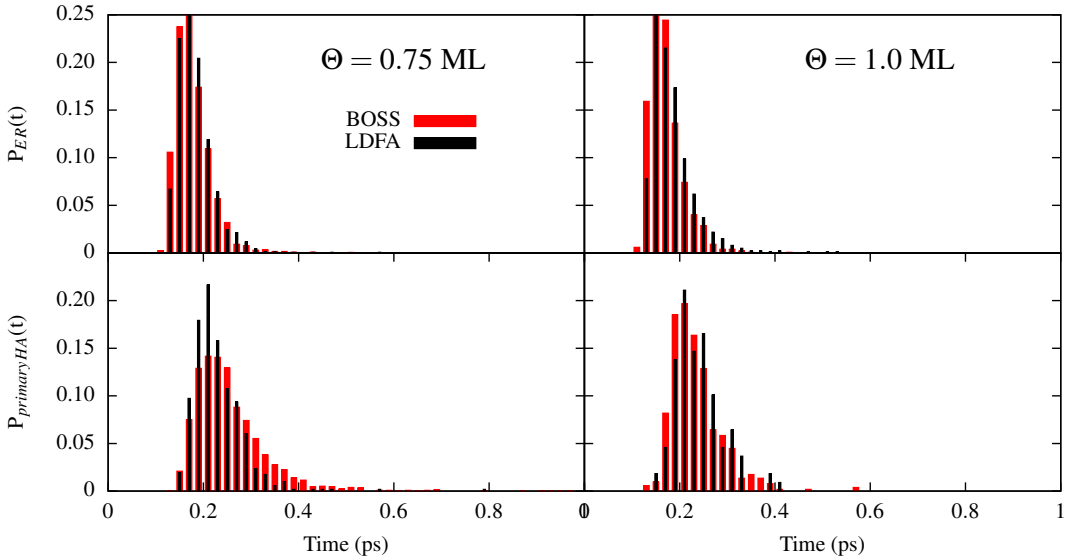

Figure VII.7: Same as Figure VII.6 but for Θ= 0.75 and 1.0 ML coverages when E$_i$=0.5 eV.

lifetime for the hot species. Moreover, a high density of adsorbates also results in a

screening of the impinging hydrogen that then cannot interact closely with the surface. The influence of $e-h$ pair excitations on the timescale of both mechanisms at Θ=0.75 and 1.0 ML coverages when E_i=0.5 eV (Figure VII.7) is equally negligible. The extra energy loss mediated by $e-h$ pair excitations thus influences much less reactivity at such coverages, as illustrated by Figure VII.3 and VII.4.

At high coverage (Θ=1.0 ML) and low incident energy (<0.5 eV), the simulations predict a large *adsorption* probability (>80%), suggesting possible supersaturation of the surface. The dynamics predicts that the extra atom adsorbs in the second three-fold hollow site of the unit cell. In order to discard any interpolation error, additional DFT relaxation calculations have been carried out for 41 adsorbates (Θ=1.025 ML) using a 5×4 surface unit cell and the same parameters previously adopted for the construction of the CRP PES [222]. These calculations confirm indeed that *adsorption* of an H atom on the saturated surface is energetically favorable by 2.07 eV, the structure of the surrounding H atoms being slightly distorted as illustrated in the inset of Figure VII.4 (left). Interestingly, such adsorbing sites with lower binding energy have already been anticipated in the literature to rationalize the experimentally observed hot vibrational states distributions of H_2 molecules resulting from *abstraction* on Tungsten surfaces [143, 233]. Low-energy electron diffraction and inelastic He-atom scattering measurements have actually confirmed the formation of hydrogen superstructure at Θ=1.5 ML coverage. [240]

Finally, we analize the average internal energy distribution of the formed molecules. The final average translational, vibrational, and rotational energies of the *ER*-formed and *HA*-formed H_2 molecules are plotted in Figures VII.8, as a function of the initial collision energy E_i at Θ=0.25 (left), 0.75 ML (middle), and 1.0 ML (right) coverages. Results from BOSS (squares and dashed lines) and LDFA (circles and solid lines) calculations are shown. The main conclusions of previous BOSS calculations [78] are unchanged. Although *ER*-formed molecules own always higher internal energy than *HA*-formed molecules, both mechanism produce "hot" molecules.In both *ER* and *HA* mechanisms the energy of the formed molecules increases with E_i, in particular the translational energy. With increasing coverage the mean final translational energy of the formed molecules clearly decreases, whereas the average rotational and vibrational energies of the formed molecules are less affected by coverage.When accounting for $e-h$ pair excitations the formed molecules suffer an important reduction in the average translational energy in both *abstraction* mechanisms. The average rovibrational energy of the formed molecules is slightly and very similarly affected in both *abstraction* processes, except at low coverage and high E_i. At these conditions, the inclusion of electronic excitations reduces more the average vibrational energy of the *HA*-formed molecules than that of the *ER*-formed ones. Surprisingly, at low coverage and low E_i, the inclusion of $e-h$ pair excitations affects similarly the final energy distribution of *ER* and *HA*-formed molecules. This

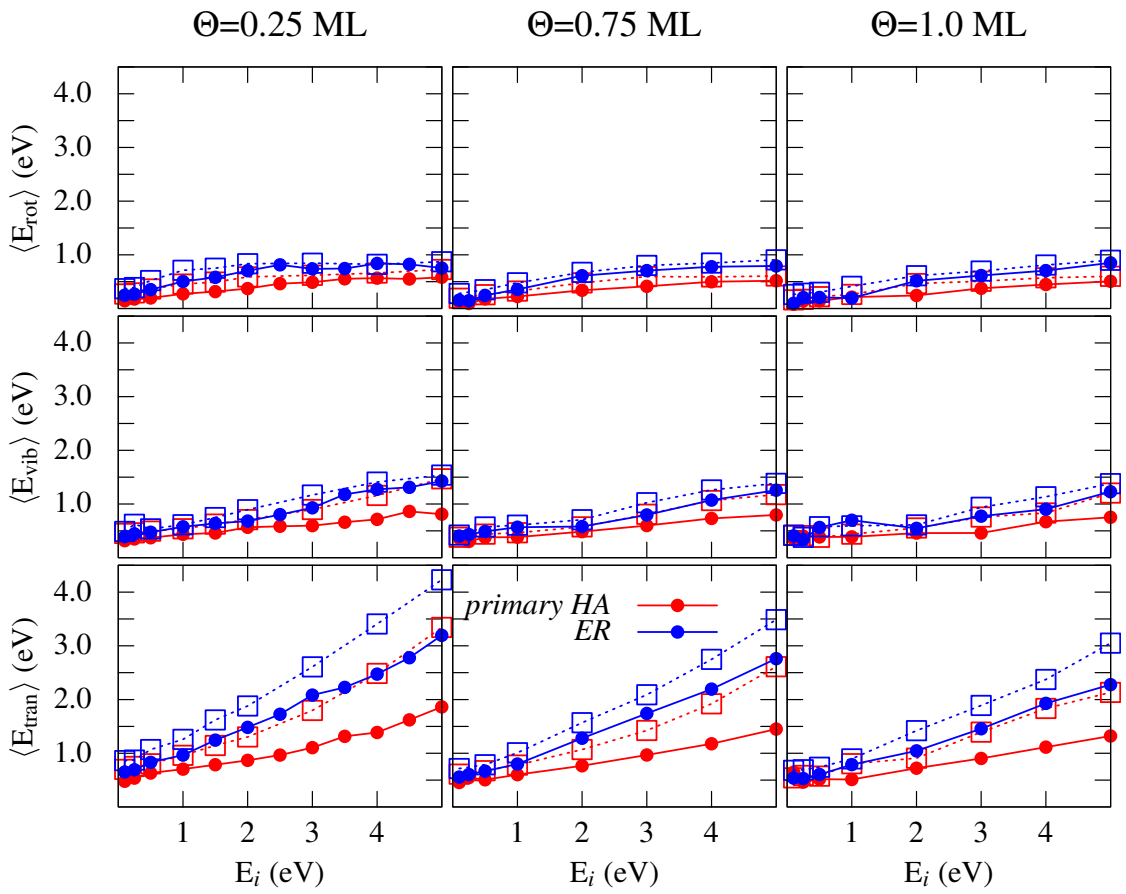

Figure VII.8: Final average translational $\langle E_{tran} \rangle$, vibrational $\langle E_{vib} \rangle$, and rotational energies $\langle E_{rot} \rangle$ of the *ER*-formed (blue) and *HA*-formed (red) molecules as a function of the initial collision energy E_i: BOSS (squares and dashed lines) and LDFA (circles and solid lines).

contrasts with the drastic reduction we observe at these conditions in the *HA* cross sections that are not observed for *ER* reaction, but also with the average energy loss of the projectiles to $e-h$ pair excitations in *ER* and *HA* *abstraction* processes as a function of E_i shown in Figure VII.9. Although the energy loss to $e-h$ pair excitations in *HA* *abstraction* is about two times larger than in *ER* reaction, the reduction on the average final energy of the formed molecules when including electronic excitations is similar for both mechanisms. For instance, the same reduction of 0.54 eV is observed at E_i=1.0 eV and 0.25 ML coverage. The reason is that the inclusion of electronic excitations removes principally the slow reaction time *HA* trajectories that were leading to "cold" products in the BOSS calculation. The latter compensates the reduction of energy experienced when accounting for electronic excitations by fast reaction time *HA* molecules that remain, i.e., by "hot" molecules. As the coverage increases the energy losses to electronic excitations for the two mechanisms become more similar, in accordance with the closer reaction times for *ER* and *HA* *abstraction* processes (see Figure VII.7).

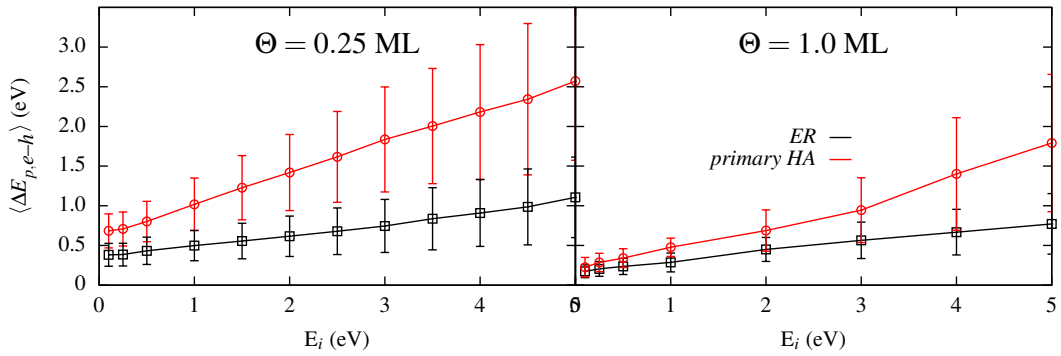

Figure VII.9: Projectile's average energy loss into $e-h$ pair excitations $\langle \Delta E_{p,e-h} \rangle$ as a function of the incident energy E_i.

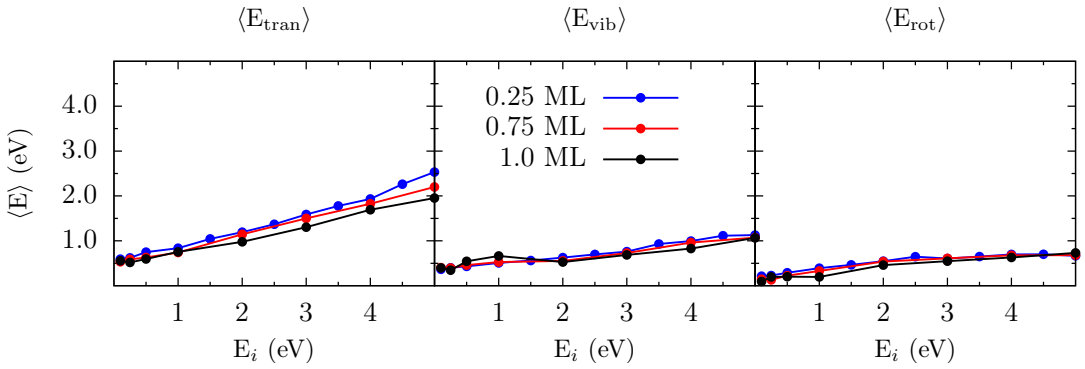

Figure VII.10: Final average translational $\langle E_{tran} \rangle$ (bottom panels), vibrational $\langle E_{vib} \rangle$ (middle panels), and rotational energies $\langle E_{rot} \rangle$ (top panels) of the abstracted H_2 molecules as a function of the initial collision energy E_i. LDFA results for Θ=0.25 ML (blue), 0.75 ML (red) and 1.0 ML (black) are shown.

All in all, within LDFA the final energy distribution of abstracted H_2 molecules as a function of E_i (Figure VII.10) slightly depends in the coverages. Whereas a decrease of the translational energy is observed when increasing the coverage, the average rotational and vibrational energies of the formed molecules show more complex behavior that depend on the incident energy E_i. Nevertheless, the changes in the internal energies due to the coverage are small, thus the final energy distribution of the molecules shows weak sensitivity in coverage.

VII.3 Conclusions

This chapter has been devoted to theoretically investigate the effect of $e-h$ pair excitations on hydrogen *abstraction* on the W(110) surface at finite coverages. Although

the effect of $e-h$ pair excitations is to increase *adsorption* at the expense of *absorption*, *reflection* and *abstraction*, the qualitative evolution of the three former channels with E_i hardly changes. Focusing on the different abstraction processes, the *HA recombination* mechanism, which is supposed to dominate *recombination* at low coverage and low E_i, is shown to be significantly affected by the efficient energy loss via low-energy electronic excitations that greatly reduce the relaxation time of *hot* hydrogen *atoms* on the W(110) surface. As a result, the *HA* mechanism is considerably diminished in favor of H *adsorption* for these incidence conditions. Thus, the evolution of the *abstraction* channel with E_i changes at Θ=0.25 ML coverage. As a matter of fact, within LDFA both *ER* and *HA* mechanisms compete whatever the coverage, but as the coverage increases *ER* becomes the dominant *abstraction* channel.

Regarding the final energy distribution of the formed molecules, the effect of $e-h$ pair excitations depends on the timescale of the process under study. At the low 0.25 ML coverage the final energy distribution of *HA*-formed molecules suffers higher reduction than that of *ER*-formed molecules when including electronic excitations. At higher coverages, as both *HA* and *ER* processes take place in the same timescale, similar effect of $e-h$ pair excitations is obtained in both mechanisms. Low energy $e-h$ pair excitations mostly reduce the translational energy of the molecules in all cases. Overall, within LDFA the average energy partition between translation, rotation, and vibration is weakly affected by coverage.

Chapter VIII

Adiabatic and non-adiabatic dynamics of Hydrogen *abstraction* from H-covered W(100)

Although similar H *abstraction* kinetics are observed for Ni(100) and Ni(110) [81], for Pt [241], Cu [95], and Ag [136] differences are observed for the different crystal faces, which has been related to the reconstruction these surfaces experience. In the previous Chapter, we have shown that H *recombination* on W(110) proceeds via both *ER* and *HA* mechanisms for low E_i and low coverage, whereas as the coverage increases *ER* mechanism dominates the *abstraction* of H_2. This chapter is devoted to study the influence of surface symmetry on both *abstraction* channels by investigating the H_2 *recombination* from W(100) at finite coverages. In order to do so, a multiadsorbate CRP PES has been constructed.

The Chapter is structured as follows. Details of the construction of the CRP PES are presented in Section VIII.1. In Section VIII.2 the influence of the PES representation within the single adsorbate limit is analyzed. The multiadsorbate CRP PES for the H-covered W(100) surface is presented in Section VIII.3. Then, in Section VIII.4, the dynamics of H *abstraction* from H-covered W(100) is analyzed and compared with previous results for H *abstraction* on H-covered W(110). Energy dissipation via $e-h$ pair excitations is studied since they are shown to drastically affect hyperthermal diffusion of H hot atoms on W(110), and concomitantly *HA abstraction*. Finally, Section VIII.5 concludes.

VIII.1 Construction of the H+H/W(100) potential energy surface

The PES constructed to study H_2 dissociation on W(100) by H. F. Busnengo and A. D. Martínez [222] has been extended in order to simulate H *recombination* with H-covered W(100). Let us refer to the former as H_2/W(100) PES and to the latter as H+H/W(100) PES. To model the LH mechanism [242], which can be seen as the reverse mechanism of dissociative adsorption, a PES determined for dissociative adsorption can usually be used straightforwardly without any additional data. For *HA* and *ER recombinations*, conversely, atomic configurations at the entrance channel (one atom far from the surface) have to be added in the interpolation or fitting scheme. For dissociative adsorption, internuclear distances in the range of $[r_{eq}/2,\ 2r_{eq}]$ are, usually, considered, where r_{eq}=0.75 Å is the equilibrium internuclear distance. For *abstraction* processes, internuclear distances until the atom-atom interaction vanishes must be taken into account for the whole Z range. In the particular case of H_2 interacting with non-magnetic metal surfaces as W, spin-polarized DFT calculations are required whenever the interatomic distance r >1.6 Å and at least one of the atoms is relatively far from the surface, e.g., for Z >2.6 Å. Therefore, extra spin-polarized DFT atom-surface and molecule-surface calculation need to be added.

To compute the extra H- and H_2-surface total energies, DFT calculations had been carried out using the same parameters as in the construction of the H_2/W(100) PES. The slab supercell approach is applied. A 2×2 cell and a 5×5×1 mesh of **k**–points according to the Monkhorst-Pack method [158] are used. An electron smearing of σ=0.4 eV is introduced within the Methfessel and Paxton approach. The PW91 [243,244] functional is used to describe electronic exchange and correlation. We have used the VASP code [245–249] that employs a plane wave basis set to describe electronic wave functions. Electron-ion interactions are described through ultrasoft pseudopotentials [250]. The energy cutoff employed in all the calculations was set to 230 eV. With these parameters the obtained equilibrium lattice constant for bulk W is a = 3.17 Å, in good agreement with the experimental value [251].

The construction of the multiadsorbate H+H/W(100) PES has been done following the CRP interpolation method, explained in Chapter III. The H_2/W(100) PES of Ref. [222] was obtained by interpolation of 28 2D-(Z_{CM}, r) cuts calculated with DFT. These 2D-(Z_{CM}, r) cuts have been extended to r_{max} =3.0 Å, which is the value at which I^{6D} is found to vanish. The sites (X_{CM},Y_{CM}) for which 2D-(Z_{CM}, r) cuts were used as input data are: $(0,0)$, $(a/4,0)$, $(a/2,0)$, $(a/4,a/4)$, $(a/4,a/2)$ and $(a/2,a/2)$ where a =3.17 Å. On high-symmetry sites, only 2D-(Z_{CM}, r) cuts for molecular configurations

perpendicular and parallel to the surface were used, whereas on low-symmetry sites tilted configurations (with ϑ=$\pi/4$) are included in the input data set. The V^{3D} atom-surface potentials were computed for the same surface sites, to which spin polarized energy data had been added for Z >2.6 Å. Moreover, the PES was generalized to describe H penetration to the subsurface down to −4 Å by the addition of V^{3D} data for Z values down to −4 Å (Z=0 is defined by the altitude of the topmost surface layer). For negative values of the center of mass altitude of the molecule Z_{CM}, the interpolation function I^{6D} is assumed to be constant and equal to the value of I^{6D} at Z_{CM}=0 Å. Therefor, the PES does not accurately describe the atom-atom interaction within the bulk. However, our goal had been to model *recombination* of atoms that penetrate in the bulk and later return to the surface where they recombine. In fact, in the QCT calculations we did not find any event in which two atoms interact well inside in the metal.

Once the DFT energy data are calculated the previously employed interpolation procedure is used: I^{6D} was obtained by subtracting the atom-surface interactions V^{3D} from the molecule-surface potential [252]. 2D-cubic splines are used in the interpolation of I^{6D} over Z_{CM} and r for each molecular configuration. Then symmetry-adapted expansions of trigonometric functions are employed for the interpolation over ϑ and φ on each surface site [253]. Finally, for the interpolation over X_{CM} and Y_{CM} 2D-periodic cubic splines are used. The atom-surface potentials were interpolated by using a 3D-cubic spline.

The resultant PES reproduces properly the most stable atomic adsorption configuration located in the bridge position with a Z altitude of 1.107 Å [228,229,254–257], as well as the DFT chemisorption energy of 3.09 eV. Following the method presented in Chapter IV the X, Y and Z components of the ZPE have been calculated. For the parallel motion to the surface, the ZPE is 69 meV and 40 meV, respectively, for the X and Y directions. The ZPE for vibrational motion normal to the surface is 67 meV. These values are in good agreement with theoretical [258, 259] and experimental [227, 229, 255, 260] values reported previously for H/W(100).

In order to evaluate the quality of the constructed CRP PES, additional DFT energy calculations have been performed and compared with the CRP values. We also compare with the FPLEPS PES to evaluate the differences between the two PES representations. Figure VIII.1 shows 1D-cuts of the potential as a function of the projectile altitude for a given (X_p, Y_p) position while the target is fixed in the bridge site. The agreement between DFT data and the CRP PES is very good (discrepancies being lower than 60 meV), while the FPLEPS is less accurate (discrepancies being lower than 300 meV). For the 1D cuts of Figure VIII.1 root mean square deviations (RMSD) for the FPLEPS and CRP PESs are 195 meV and 22 meV, respectively. In total, we evaluated the spin-polarized DFT

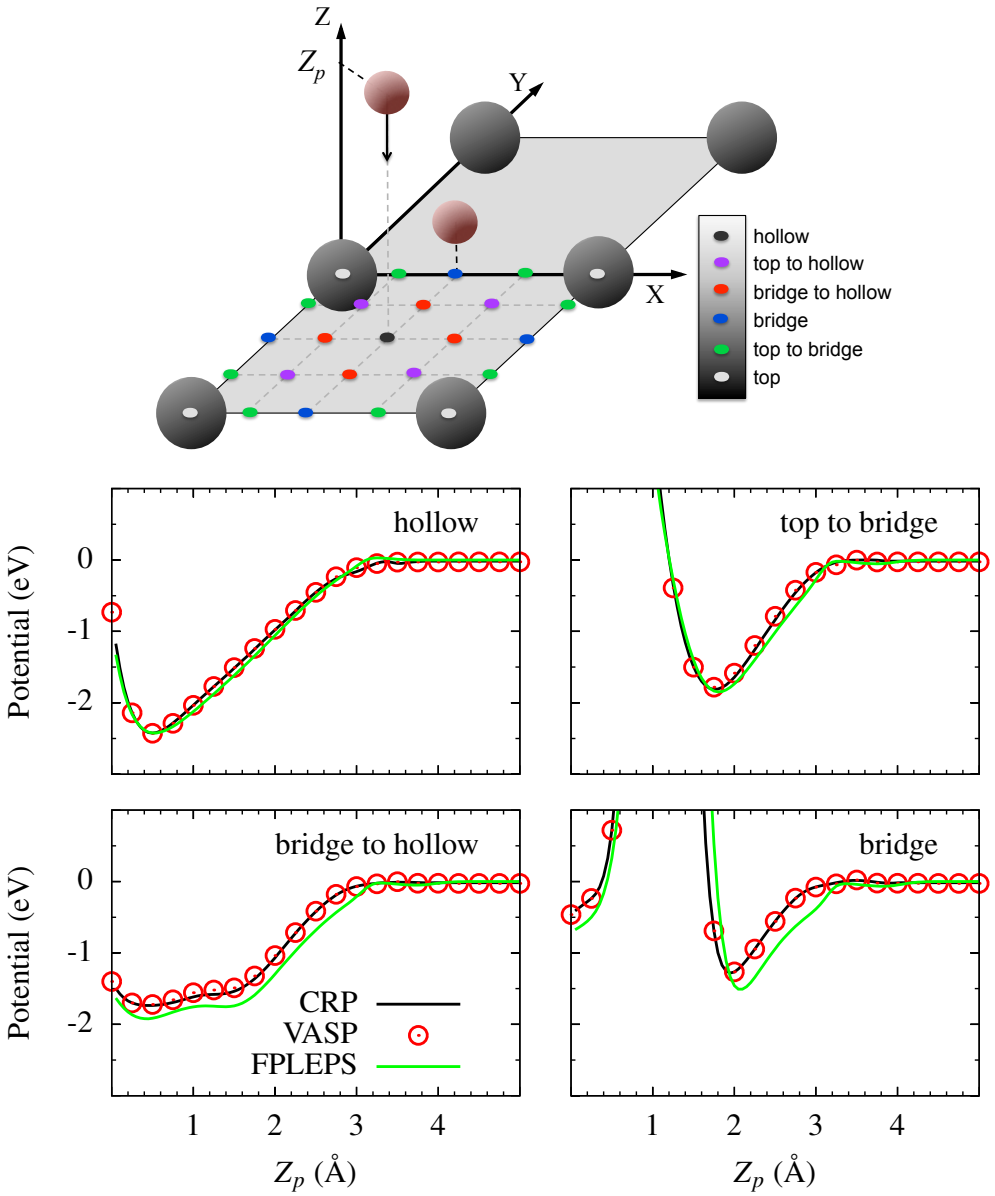

Figure VIII.1: Comparison between the CRP (black line), the FPLEPS (green line), and the spin-polarized DFT calculations (red circles) in the *ER* entrance channel for different (X_p, Y_p) positions: (A) top to bridge $(0, a/4)$, (B) bridge $(a/2, 0)$, (C) hollow $(a/2, a/2)$ and (B) bridge to hollow $(a/2, a/4)$ positions. The different (X_p, Y_p) positions and the coordinate system defining Z_p are indicated in the upper figure.

total energy of 192 configurations, for the target at bridge, bridge to hollow, and top to bridge positions while the projectile approaches the surface from 3.5 Å to 0 Å over top, bridge, hollow, top to bridge, bridge to hollow, and top to hollow positions. Only potential energies relevant for the present work (<5.0 eV) are considered. We compared them with the values predicted by the FPLEPS and CRP PESs. The RMSD were 50 meV for the CRP and 300 meV for the FPLEPS.

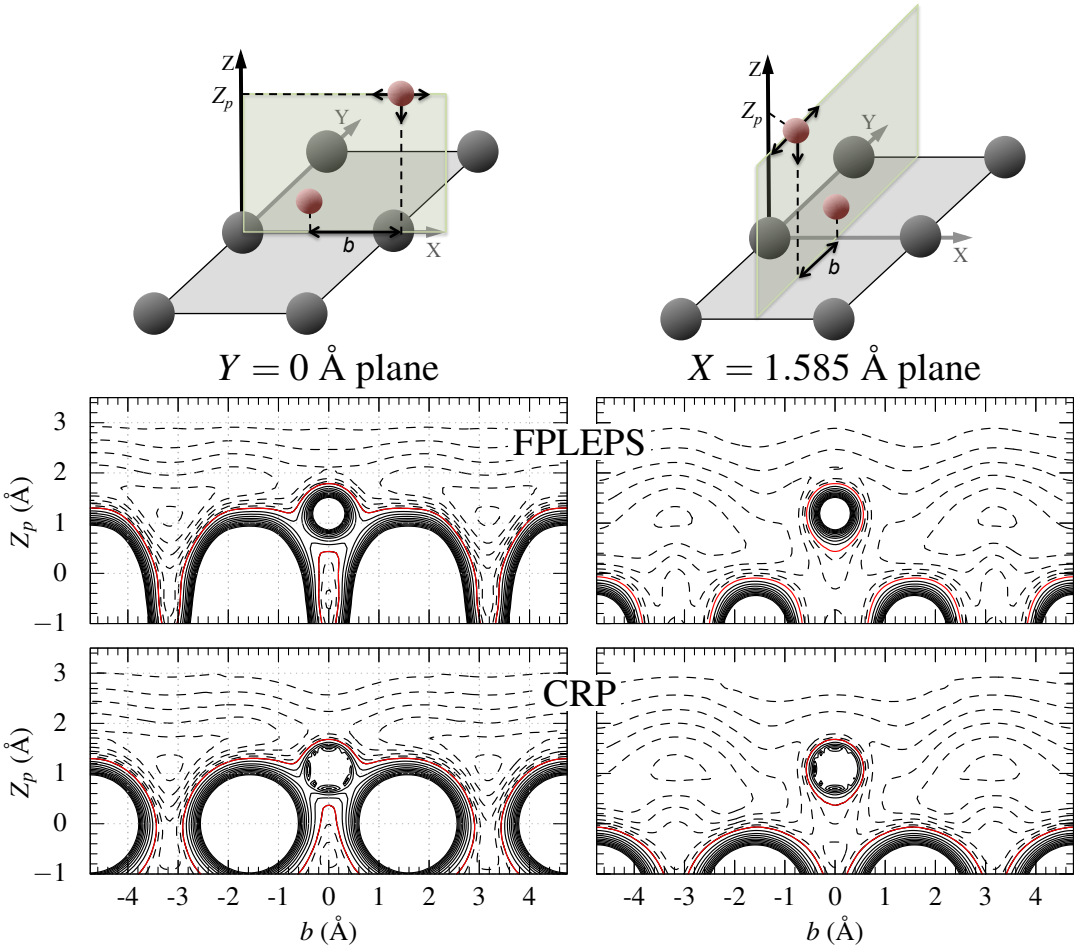

Figure VIII.2: 2D (b,Z_p)-cuts of the FPLEPS (top) and the CRP (bottom) PESs. The adsorbate sits in its equilibrium position and the projectile spans the (b, Z_p) plane for X=1.585 Å (right panels) and Y=0 (left panels). Full lines (dashed lines) are positive (negative) potential isovalues separated by 1 eV (0.5 eV). The red line correspond to zero potential energy isovalue. Top right (left) scheme indicate the (b, Z_p) plane for X=1.585 Å(Y=0) and the coordinate system used.

As mentioned in Chapter IV, useful information can be extracted from a static analysis of the PESs. Potential energy 2D (b, Z_p)-cuts along $X_p = 1.585$ Å and $Y_p = 0$ Å planes are displayed in Figure VIII.2 for the CRP (left) and FPLEPS (right) PESs. The adsorbate sits in its equilibrium position, whereas the projectile is allowed to move on the $X = 1.585$ Å and $Y = 0$ Å (b, Z_p) planes as sketched in upper part of Figure VIII.2. In both planes, the PES shows an attractive potential directed to the unoccupied bridge sites. In the vicinity of the target, the potential is less attractive. The repulsive structure resembles the crystal structure within the plane. The two PESs are qualitatively very similar. However, some discrepancies are observed. On the one hand, close to the target position, the topology of the two PESs differs due to the lower adsorption altitude in the CRP PES. On the other hand, the absorption windows in the

$X_p = 1.585$ Å plane are much thinner in the CRP PES than in FPLEPS (see down left panel of Figure VIII.2).

VIII.2 Dynamics of H_2 *Eley-Rideal abstraction* from W(100): Zero coverage limit

In order to analyze the sensitivity of the *ER abstraction* dynamics on the PES representation, the normal incidence scattering of atomic hydrogen off H-preadsorbed W(100) surface is investigated within the zero coverage limit (single adsorbate), using QCT. The constructed global ground-state CRP PES for two atoms interacting with an infinite and periodic surface is employed. The same initial conditions studied in Chapter V are investigated in order to compare with FPLEPS results.

The *ER* cross sections as a function of E_i for the FPLEPS and CRP PESs are shown in Figure VIII.3. Although some differences in the PESs have been identified when comparing potential energy curves, these differences hardly affect *ER* reactivity. Small quantitative differences are only found at high E_i, but the evolution of σ_{ER} with E_i is unchanged.

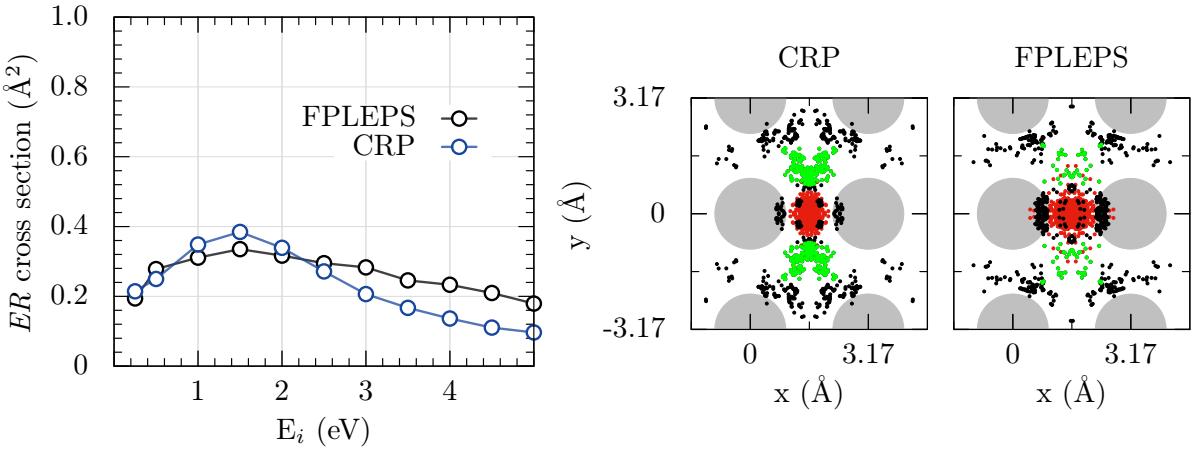

Figure VIII.3: Left panel: Cross sections for *ER abstraction* using the CRP (blue) and FPLEPS (black) PESs. Right panels: (X_p,Y_p) turning positions of the projectiles leading to *ER recombination* at E_i=0.5 eV for the CRP and FPLEPS PESs by rebounding on the first layer W atoms (black) and second layer W atoms (green). The positions of the recombining target atoms are indicated by red points.

Even if *ER* reactivity is weakly affected by the representation of the PES, some dynamical changes are observed in the *ER abstraction* process. As previously characterized, reactive trajectories may proceed upon colliding on the first W layer as well as on the second W layer [77] (below the hollow site). The analysis of the (X_p, Y_p) turning points

for the projectiles leading to *ER recombination* shown in right panels of Figure VIII.3 highlights the contribution of molecules bouncing off the second layer (green points) at the expense of reaction through collision on the closest W atoms to the adsorbate. For the CRP (FPLEPS) PES, the projectile goes below the target and catches it on its way back after colliding in a second layer W atom for 35% (11%) of *ER* trajectories. This is very likely due to two differences in the PESs. On the one hand, *ER* reaction upon collision on the two closest W atoms to the target decreases due to the lower adsorption Z altitude of the adsorbate in the CRP (1.107 Å) PES (1.2 Å for the FPLEPS). On the other hand, projectiles are more efficiently scattered towards the target by the second layer W atoms due to the thinner *absorption* path in the CRP PES representation (see Figure VIII.2, Section VIII.1). Moreover, due to the lower adsorption altitude on the CRP PES, the adsorbates (red points) are less displaced from the adsorption site in this PES representation when the projectile bounces off the surface.

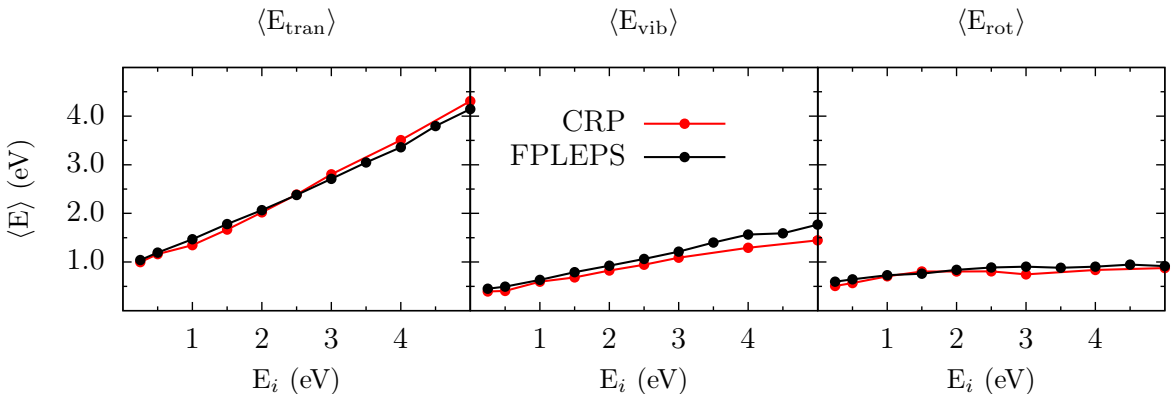

Figure VIII.4: Final average translational $\langle E_{tran} \rangle$, vibrational $\langle E_{vib} \rangle$, and rotational energies $\langle E_{rot} \rangle$ of the *ER*-formed H_2 molecules as a function of E_i. Results for FPLEPS (black) and CRP (red) PESs are shown.

Figure VIII.4 displays the mean final translational, rotational and vibrational energies of the *ER*-formed H_2 molecules as a function of E_i. Although there are some small quantitative discrepancies in the vibrational mode at high E_i, the qualitative behavior is not affected by the PES representation.

VIII.3 Multiadsorbate potential energy surface for H-covered W(100)

In order to account for finite coverages, we expand the interaction potential up to two-body terms. Therefore, three-body and higher order interactions between adsorbates

are disregarded (see Chapter III). Θ=0.5 ML and 1.0 ML H-coverages on W(100) have been modeled using a 6×6 rectangular (a×a) array with periodic boundary conditions. Same adsorption positions as in the single adsorbate limit are found for such coverages, since the atoms do not interact at larger internuclear distances than 3.0 Å. The studied adsorption structures for the two coverages can be visualized with help of Figure VIII.5.

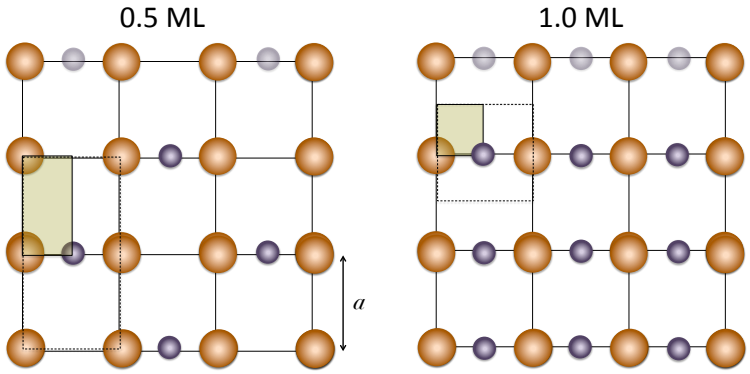

Figure VIII.5: Position of the adsorbed H atoms at Θ=0.5 ML (left) and 1.0 ML (right).The purple points represent the H atoms positions and a=3.17 Å is the lattice constant parameter. Sampling areas of initial (X_p,Y_p) positions of the projectiles for each coverage are represented in yellow.

Potential energy 2D (b, Z_p)-cuts for the different coverages along the X_p = 1.585 Å and Y_p = 0 planes at Θ=0.5 ML and 1.0 ML coverages are shown in Figure VIII.6. The comparison with Figure VIII.2 shows that at Θ = 0.5 and 1.0 ML coverages the interaction potential close to the target is very weakly affected by the coverage. In the X_p = 1.585 Å and Y_p = 0 Å planes, at 0.5 (1.0) ML coverage the interaction potential is a periodic repetition of the interaction potential in the b range [-1.585 Å,1.585 Å] ([-4.755 Å, 1.585 Å]) for one adsorbate (Figure VIII.6). Therefore, for 1 ML coverage the attractive potential wells are fully occupied on these planes. As a consequence the interaction potential is less attractive. We also analyze the $Y = X - 1.585$ Å plane, and its parallel $Y = X - 4.755$ Å plane, (A) and (B), respectively, on the upper scheme in Figure VIII.6. At 1.0 ML coverage, both planes are equivalent. At 0.5 ML, half of the diagonal planes do not have any adsorbate filing a bridge adsorption site within the plane. This is noticed in the 2D (b, Z_p)-cuts for the $Y = X - 4.755$ Å plane in Figure VIII.6. The negative values of the interaction potential is therefore reduced as the coverage increases and the projectiles will experience in average less attraction to the surface.

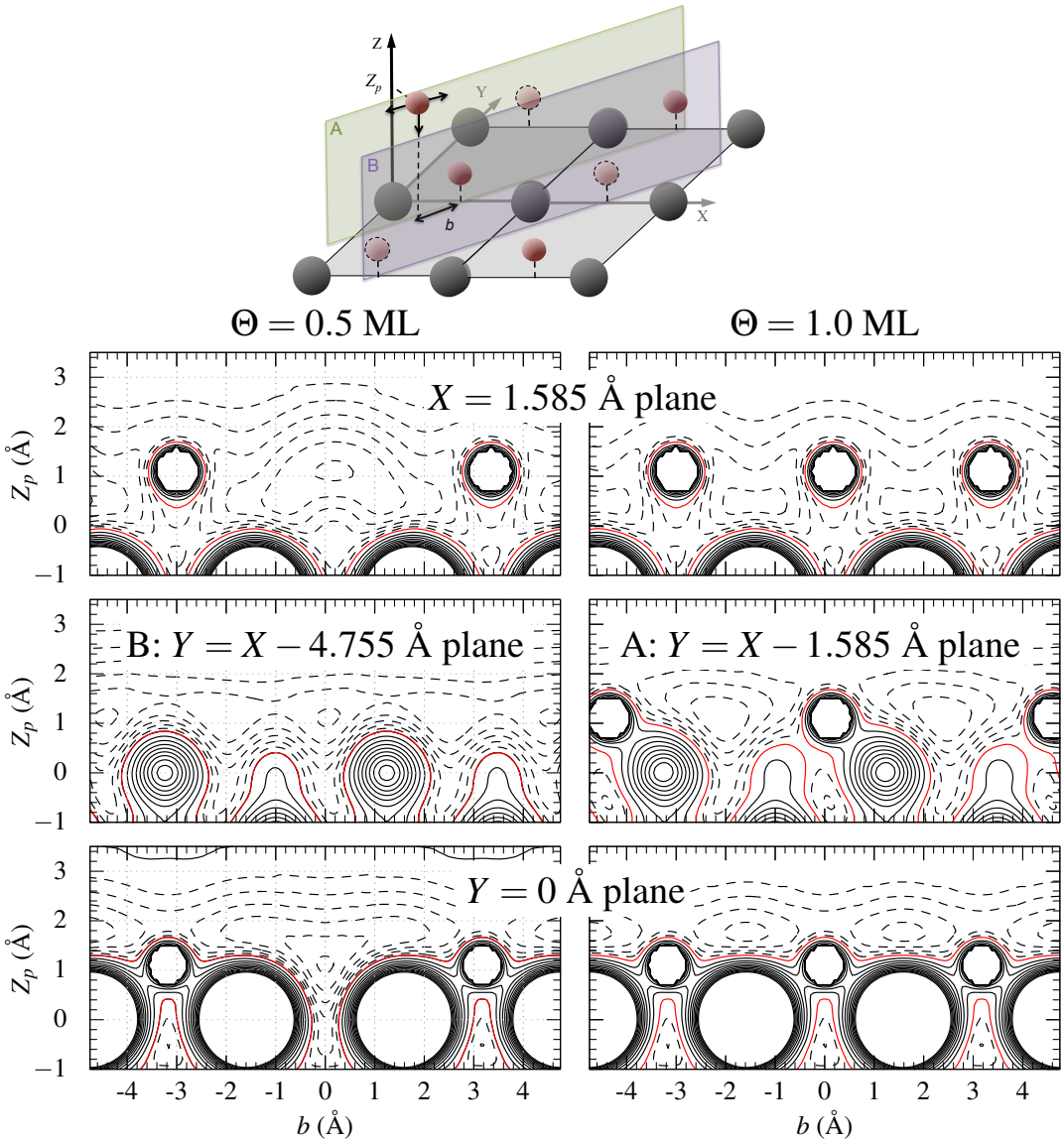

Figure VIII.6: 2D (b, Z_p)-cuts of the multiadsorbate CRP PES for $\Theta = 0.5$ ML (left) and 1.0 ML (right) coverages when the adsorbates sit in their equilibrium position and the projectile spans the indicated (b, Z_p) plane. The coordinate system and the $Y = X - 1.585$ Å(A) and $Y = X - 4.755$ Å (B) planes are indicated in top. the Y=0 and X=1.585 Å planes and the corresponding coordinate systems have been indicated in Figure VIII.2. 0.5 (1.0) ML surface coverage is represented by light (dark and light) red points. Full lines (dashed lines) are positive (negative) potential isovalues separated by 1 eV (0.5 eV). The red line correspond to zero potential energy isovalue.

VIII.4 Recombination of H_2 upon H scattering off H-covered W(100)

The normal incidence scattering of atomic hydrogen off an H-covered W(100) surface is simulated using QCT, for $\Theta = 0.5$ ML and 1.0 ML coverages. The approach relies

on the DFT based multiadsorbate CRP PES. Calculations use a 6×6 rectangular (a×a) array with periodic boundary conditions in order to model an infinite covered surface. The classical equations of motion are integrated for one projectile atom and 16 (36) adsorbed targets for Θ=0.5 (1.0) ML coverage. The targets initially sit in their equilibrium positions and are given the ZPE as detailed in Chapter IV. The initial altitude of the projectile is taken in the asymptotic region of the potential, at Z_p=7.0 Å from the surface. The (X_p, Y_p) initial position of the projectile is randomly sampled in the covered surface irreducible unit cell (yellow areas of Figure VIII.5). The factor A accounting for the total area per adsorbate is A=4 for both coverages. For Θ = 0.5 ML (1.0 ML) coverage, 30 000 (15 000) trajectories have been computed to ensure convergence. As the multiadsorbate PES ignores possible interaction between three hydrogen atoms (see eq. III.6), trajectories are stopped whenever one H atom has two neighboring H atoms closer than 1.5 Å. The corresponding contribution is taken as an uncertainty to any possible outcome of scattering defined in Chapter IV [76–78].

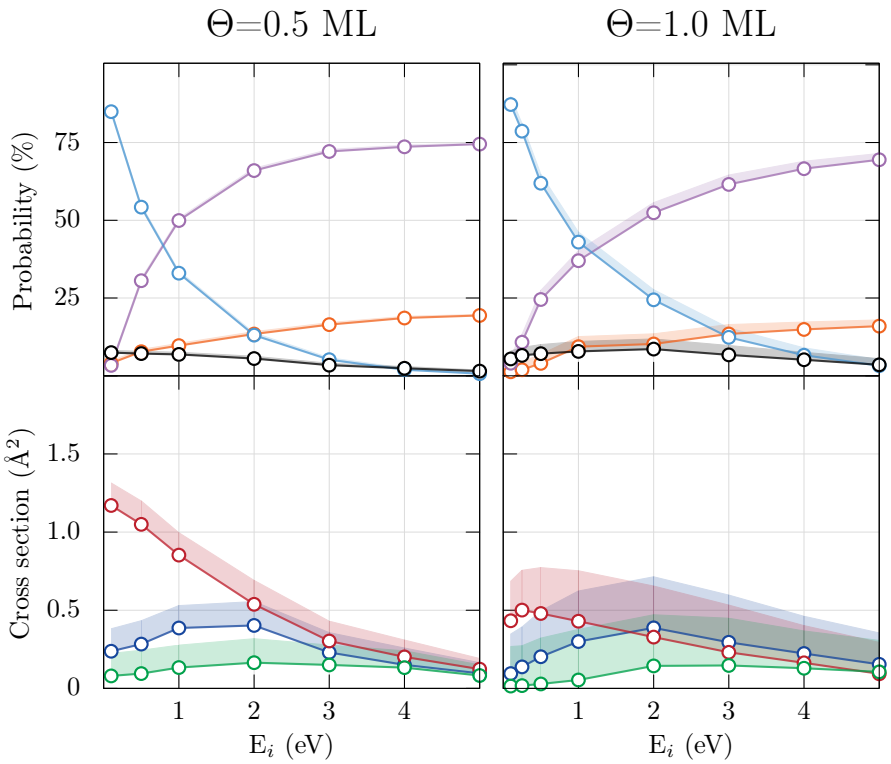

Figure VIII.7: Top panels: probabilities for *adsorption* (blue), *absorption* (purple), *reflection* (orange) and *abstraction* (black) as a function of the projectile's incident energy. Bottom panels: cross section for *ER* (blue), *primary HA* (red) and *secondary HA* (green) abstractions as a function E_i. Left and right panels correspond to 0.5 and 1.0 ML coverages, respectively. Uncertainties, which correspond to the contribution of stopped trajectories are represented by shaded domains.

In order to rationalize non-adiabatic effects upon scattering, molecular dynamics

simulations are performed within the BOSS and LDFA models. Whereas in the former energy exchange with the surface is neglected, in the latter electronic non-adiabaticity is accounted for. To prevent leakage of the ZPE, the friction acts only when the energy of the preadsorbed atom exceeds the ZPE. Dissipation to surface phonons is here ignored on the ground that, as recently demonstrated [128], dissipation to electrons is largely dominating the relaxation of hydrogen on metals. As a result of H-atom scattering, the exit channels for the finite coverage case described in Chapter IV are discriminated.

The probabilities from the BOSS calculation for *adsorption*, *reflection*, *absorption* and *abstraction* are displayed in upper panels of Figure VIII.7 as a function of E_i for Θ=0.5 and 1.0 ML coverages. Many similarities with H interaction with H-covered W(110) [78] are found (see top panels of Figure VII.2, VII.3, and VII.4). The predominant outcome at low incident E_i, *adsorption*, highly decreases in favor of *absorption* and *reflection* channels with E_i. For these processes, coverage influence is quantitative: *Adsorption* is favoured due to the more efficient energy loss to adsorbates, whereas *reflection* and *absorption* probabilities decrease with coverage.

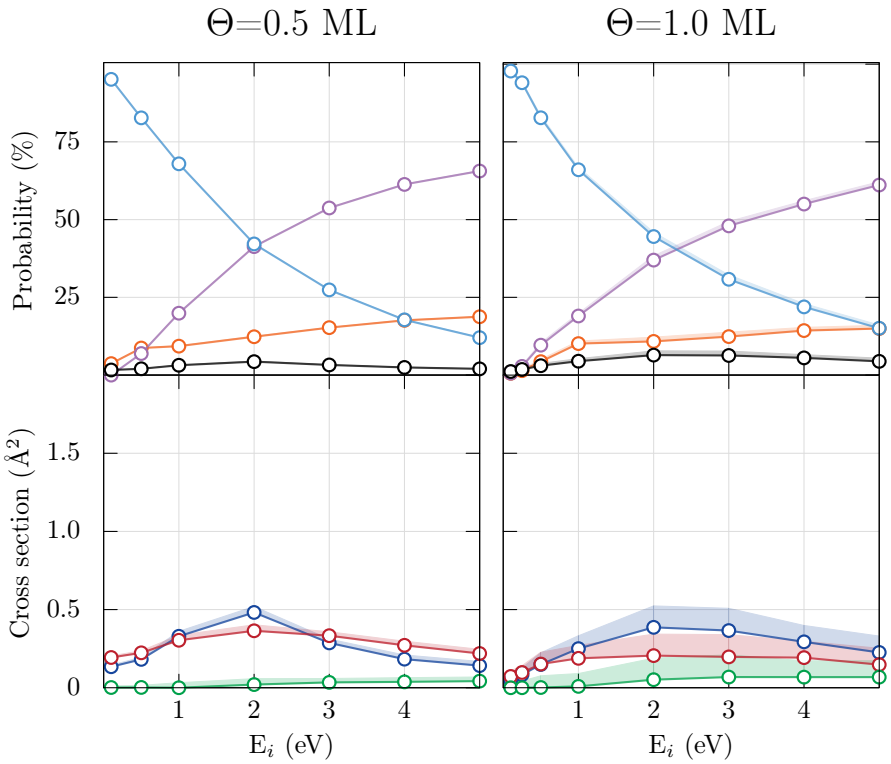

Figure VIII.8: Same as in Figures VIII.7 but for LDFA calculation.

Concerning the *recombination* processes, bottom panels of Figure VIII.7 display the cross sections *per* adsorbate for *ER*, *primary HA* and *secondary HA abstraction* as a function of E_i. As for the W(110) surface (see bottom panels of Figure VII.2, VII.3, and VII.4), within the BOSS approximation, *HA* mechanism dominates *abstraction* at

low incident energies and coverages, whereas as E_i and Θ coverage increase the two mechanisms compete. The qualitative behaviour of the cross sections changes with E_i: specifically, at 0.5 ML, *abstraction* cross section decreases with E_i, whereas at 1.0 ML, it increases until $E_i \sim 1.5$ eV, and then decreases with E_i. Secondary *HA* contribution to the total cross section is small and decreases with coverage, especially at low E_i.

The comparison with LDFA results in Figure VIII.8 helps rationalizing the effect of energy dissipation to the metal electrons. For the two coverages, accounting for $e-h$ pair excitations increases *adsorption* at the expense of *reflection* and *abstraction* (see upper panels in Figure VIII.8). Nevertheless, the qualitative evolution of these channels hardly changes because of electronic excitations. As in the W(110) surface

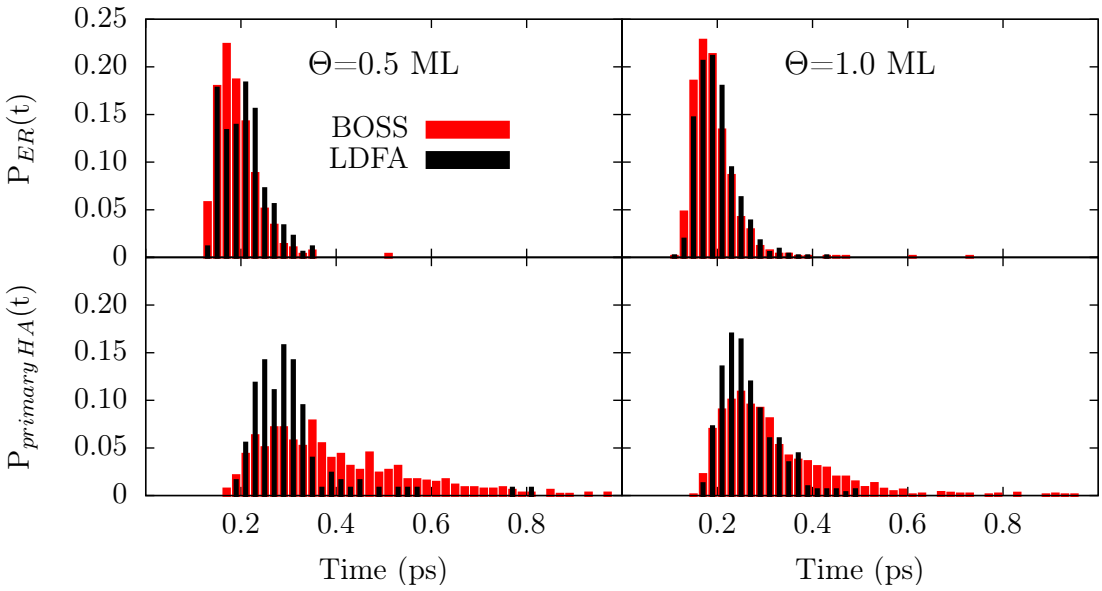

Figure VIII.9: Normalized distribution of *ER* (upper panels) and *primary HA abstraction* (bottom panels) times within the BOSS (red) and LDFA (black) simulations at Θ=0.5 ML (left) and 1.0 ML coverages (right).

The significant reduction of *HA recombination* caused by energy dissipation to $e-h$ pair excitations on W(100) stems, as well as in W(110), from the great reduction of the relaxation time for *hot* hydrogen *atoms* and concomitantly, the recombining hot-species lifetime. This is illustrated in Figure VIII.9 where the distribution of *ER* and *primary HA abstraction* times as obtained within the BOSS and LDFA simulations are displayed for Θ=0.5 ML (left panels) and 1.0 ML (right panels) coverages when E_i=0.5 eV. This time is taken as the total time for *abstraction*. At Θ=0.5 ML coverage, when accounting for $e-h$ pair excitations, the timescale for both *abstraction* processes become similar. Concomitantly, the distances travelled on the surface before *recombination* become similar. This is illustrated by representing the initial position of projectiles leading to *ER* (bottom panels) and *HA* (top panels) reaction with respect to the recombining target

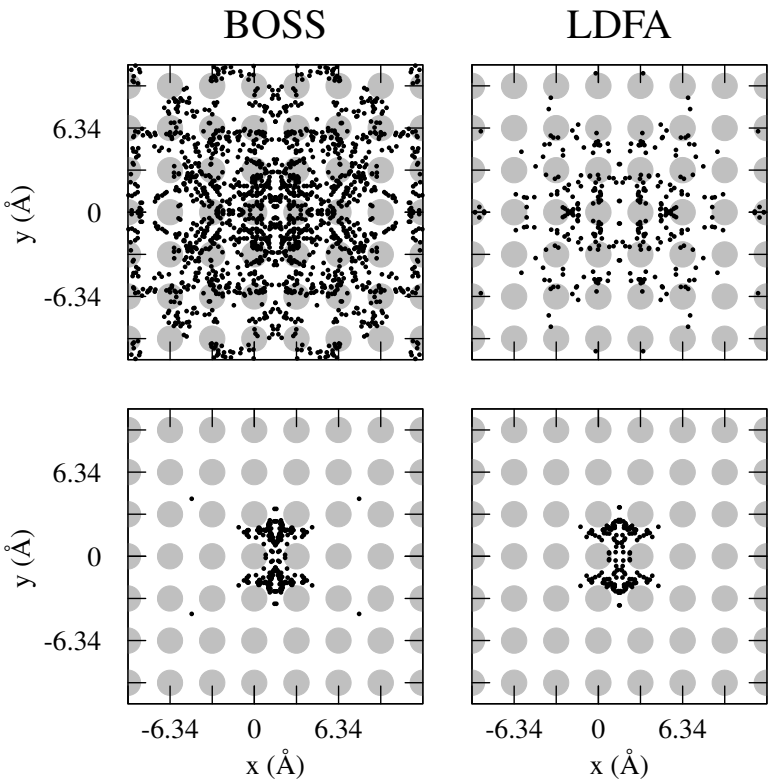

Figure VIII.10: $(X_p,\ Y_p)$ turning position of the projectiles (black points) leading to *ER* (bottom panels) and *primary HA* (top panel) *abstraction* for BOSS (right) and LDFA (left) simulations at 0.5 ML coverage when E_i=0.5 eV. The recombining adsorbate sits at the position $(X = 1.585$ Å, $Y = 0)$.

position chosen at $(X = 1.585$ Å, $Y = 0)$. The results are shown in Figure VIII.10 for BOSS and LDFA calculations. The reduction of the projectile travelled length caused by $e-h$ pair excitations is also the reason for the strong decrease observed in the LDFA *secondary HA* cross sections, in particular at low coverage. Remarkably, the influence of $e-h$ pair excitations for high coverages (Θ=1.0 ML) is less important. At this coverage, the timescale (right panels in Fig VIII.9) as well as the traveled length (left panels in Figure VIII.11) of *HA* and *ER* reaction in BOSS simulations are closer. The projectile energy is more efficiently dissipated into the other adsorbates, resulting in a short lifetime for the hot species even when electronic excitations are not accounted for. The extra energy loss mediated by $e-h$ pair excitations thus influences less reactivity at such coverages, as illustrated by Figure VIII.7 and VIII.8. Although the *ER* cross section shows low dependence on coverage, changes on the dynamics are clearly observed. At high coverage, within LDFA, projectiles impact parameters b<1.0 Å contribute significantly to the total reactivity (22%) in contrast with the findings at Θ=0.5 ML coverage, in which this contribution is smaller (9%). The static analysis of the PESs for the Θ=0.5 ML and 1.0 ML coverages (Figure VIII.6) highlights the origin of

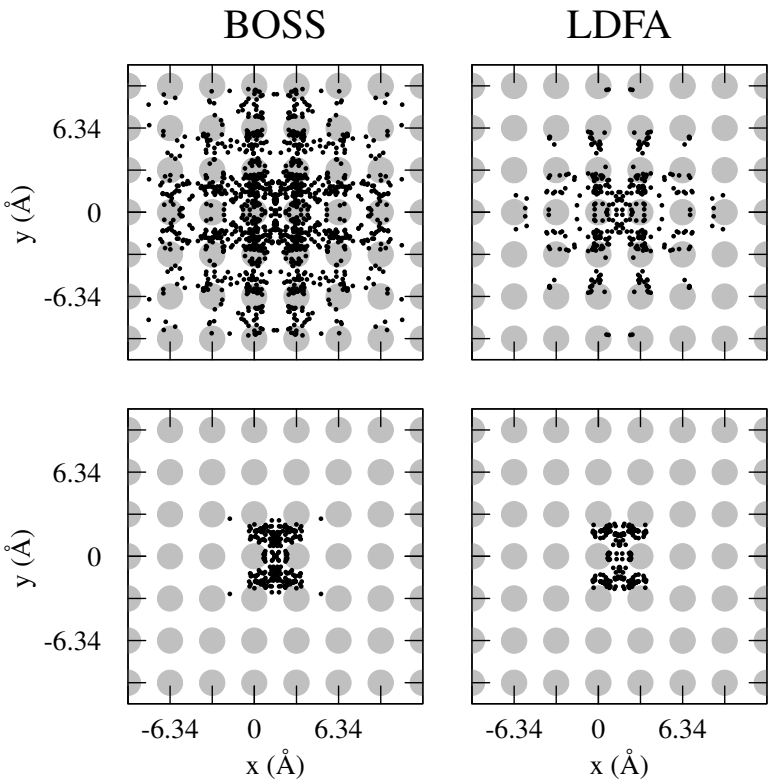

Figure VIII.11: Same as Figure VIII.10 but for Θ=1.0 ML coverage.

these dynamical changes. The attraction to the adsorption wells redirects projectiles far from the adsorbates. As coverage increases, the adsorption wells are filled and therefore, attraction diminished. Similarly to *ER abstraction*, *HA abstraction* also experiences a reduction in the b parameters of the projectiles.

For *ER recombination* of H_2 from W(100) and W(110), the influence of the crystallographic anisotropy on cross sections and energy distribution of the formed molecules was analyzed in detail within the BOSS approximation, using FPLEPS PESs [77]. Within these calculations cross sections were shown qualitatively similar, but a factor two larger on W(100) than on W(110). However, within the CRP PES representation the *ER* reactivity on W(110) increases compared with the one obtained using the FPLEPS PES [76]. In contrast, the FPLEPS and CRP PESs representations predict almost the same *ER* cross sections in the case of W(100) (see Section VIII.2). As a consequence, *ER* cross sections become rather similar in both crystal faces when employing the more accurate CRP PESs. Within LDFA, the comparison of the *ER* cross sections as a function of E_i at different coverages on the two crystal faces of W (middle panels of Figure VIII.12) highlights the weak sensitivity of *ER* cross sections on the crystal face as well as on the Θ coverage. It is also interesting to analyze the influence of the crystal face on *HA abstraction* (bottom panels of Figure VIII.12) since on this *abstraction* process the interaction

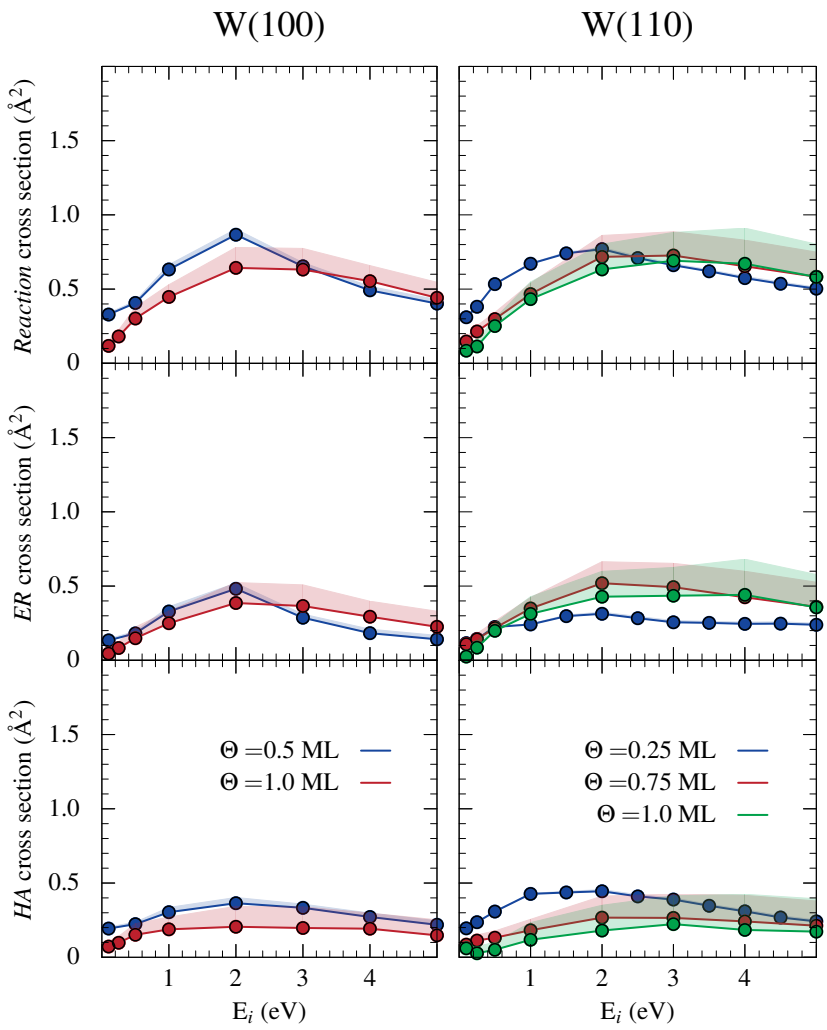

Figure VIII.12: Cross section for *ER*, *primary HA* and *abstraction* as a function of E_i off W(100) (right) and W(110) (left). Uncertainties, which correspond to the contribution of stopped trajectories are represented by shaded domains.

time of the projectile with the surface is larger. In accordance with the similarities between the dynamics of the two *abstraction* mechanisms when including dissipation to $e-h$ pairs, *HA abstraction* is also weakly sensitive in the crystal face as well as in the coverage. All in all, *abstraction* cross sections weakly depend on coverage and on the crystal face. In both systems, for low energies (E_i <2.0 eV) the *abstraction* cross sections decreases with coverage, whereas at higher energies reactivity is independent of the coverage.

Finally, we analyze the average internal energy distribution of the formed molecules. The final average translational, vibrational, and rotational energies of the *ER*-formed and *HA*-formed H_2 molecules are plotted in Figures VIII.13, as a function of the initial

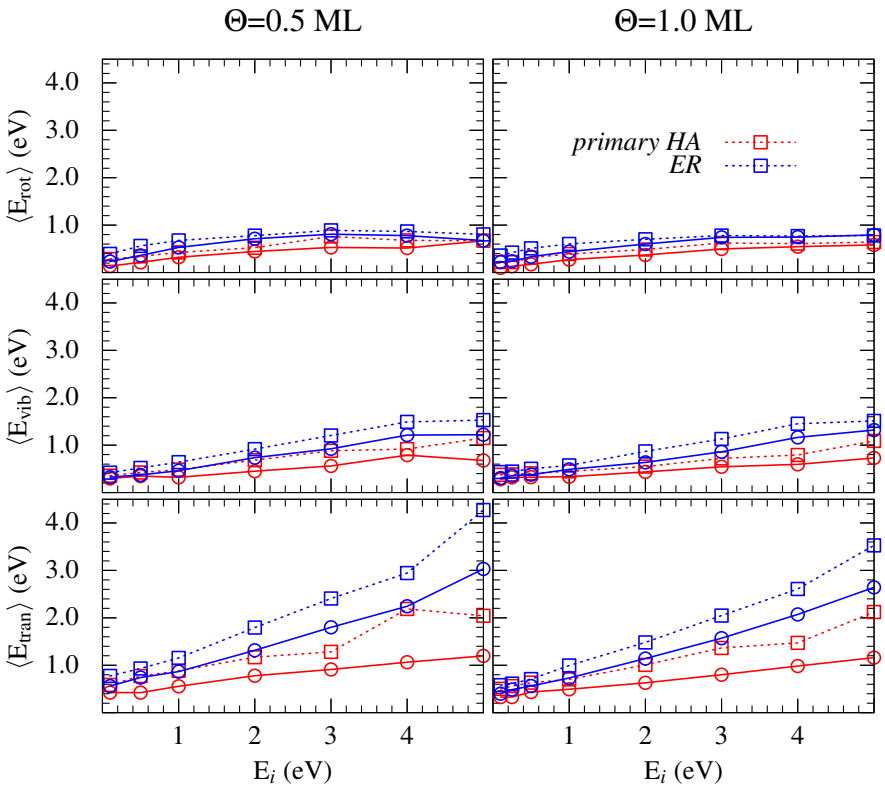

Figure VIII.13: Final average total $\langle E_{tot} \rangle$, translational $\langle E_{tran} \rangle$, vibrational $\langle E_{vib} \rangle$, and rotational energies $\langle E_{rot} \rangle$ of the *ER* (blue) and *HA* (red) formed molecules as a function of the initial collision energy E_i: BOSS (squares) and LDFA (circles).

collision energy E_i at Θ=0.5 (right panels) and 1.0 ML (right panels) coverages. As expected, *ER*-formed molecules carry always higher internal energy than *HA*-formed molecules. This is also true for each internal energy mode, but the differences at low E_i are particularly small. In both *recombination* mechanisms the internal energy of the formed molecules increases with E_i. Figure VIII.13 shows that most of the energy is channelled into translational energy. Within the BOSS simulations, the average rotational and vibrational of the formed molecules is rather similar regardless the coverage, whereas the translational energy decreases with Θ. This reveals that energy dissipation to the adsorbates increases with coverage. Interestingly, the observed decrease in the translational energy with Θ is very similar in both mechanisms. When accounting for $e-h$ pair excitations the average translational energy suffers an important reduction that decreases with Θ. As a consequence, the average translational energy slightly decreases with coverages within LDFA. In accordance with the similar lifetimes of the two mechanisms and the concomitant similar travelled distances, the effect of $e-h$ pair excitations is more or less the same for *ER* and *HA recombinations*. Overall, our results suggest that the internal energy of *ER*-formed and *HA*-formed H_2 molecules on W(100) are almost insensitive to the coverage. Moreover, the comparison of the average energy

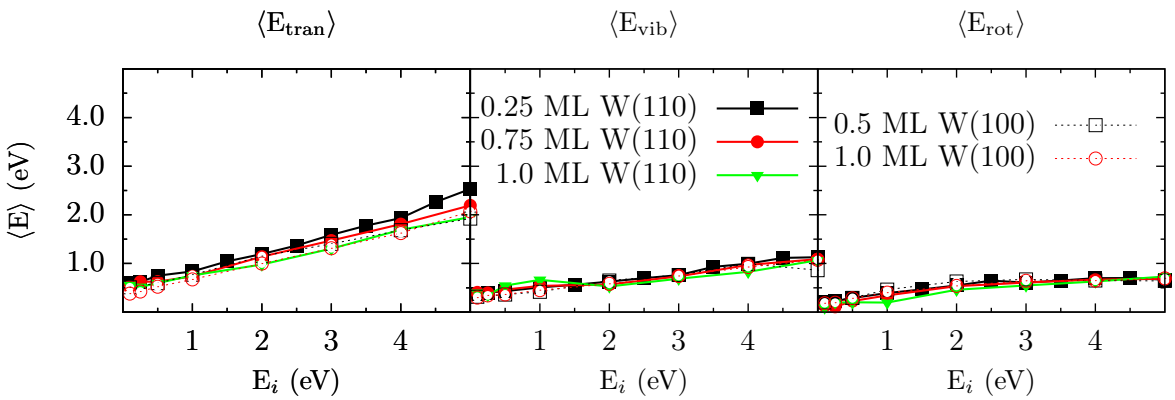

Figure VIII.14: Final average translational $\langle E_{tran} \rangle$, vibrational $\langle E_{vib} \rangle$, and rotational energies $\langle E_{rot} \rangle$ of the abstracted H_2 molecules formed in W(100) and W(110) as a function of E_i.

distributions of H_2 molecules abstracted from W(100) with the ones abstracted from W(110) as a function of E_i for all the studied coverages (Figure VIII.14) confirms this statement: the partition of internal energy of H_2 molecules abstracted from W(100) and W(110) depends on E_i, but hardly does on the coverage and crystal face within the initial conditions studied in the present work.

VIII.5 Conclusions

We have theoretically investigated hydrogen *abstraction* on a W(100) surface at finite coverages (Θ=0.5 ML and 1.0 ML). Within the BOSS approximation, the *HA* process dominates *abstraction* of H_2 at low coverage (Θ = 0.5 ML) and low collision energy (E_i<2.0 eV). *ER* and *HA recombination* processes produce vibrationally and rotationally hot molecules, however *ER* leads to the more excited ones. With increasing surface coverage, *HA* versus *ER* balance changes to make *ER* the dominant mechanism (Θ = 1.0 ML). Moreover, the total *abstraction* time decreases and both primary *HA* and *ER* processes take place in the same timescale at high coverages. The average energy partition between rotation and vibration is weakly affected by coverage changes. The mean final translational energies decrease when surface coverage increases because of scattering off other adsorbates before *recombination*.

The effect of $e-h$ pair excitations is to enhance *adsorption* at the expense of *absorption*, *reflection* and *abstraction*, but the qualitative evolution of the three former channels with E_i hardly changes. In contrast, *abstraction* is drastically reduced at low E_i and low coverage. The *HA recombination* mechanism, which is supposed to dominate *recombination* at low coverage and low E_i, is shown to be significantly affected by the electronic excitations, since they greatly reduce the relaxation time and travelled length

of hot hydrogen on the W(100) surface. As a result, the *HA* mechanism is considerably diminished in favour of H *adsorption* for these incidence conditions. Thus, the evolution of the *abstraction* channel with E_i changes at Θ=0.5 ML coverage. As a matter of fact, within LDFA both *ER* and *HA* mechanisms compete whatever the coverage, but as the coverage increases *ER* becomes the dominant *abstraction* channel. Within LDFA the average energy partition between translation, rotation, and vibration is weakly affected by coverage changes.

The comparison of LDFA calculations of H *abstraction* from W(100) and W(110) surfaces shows low sensitivity on the crystal face, both the reactivity and final energy distributions of the formed molecules are similar. Moreover, within LDFA *ER* and *primary HA* dynamics share lots of similarities at all initial conditions studied here. Both *abstraction* processes take place on the same timescale and the travelled length by the projectiles before *recombination* are similar, thus highlighting the arbitrary character of their separation. Primary *recombination* on W(100) and W(110) might be considered as a unique reactive process.

Chapter IX

Conclusions

Through these pages, we present the results of quasiclassical molecular dynamics (QCT) simulations we carried out to disentangle the influence of different factors on the *recombination* of H_2 and N_2 resulting from atomic adsorbate *abstraction* by atom scattering off the W(100) and W(110) surfaces. For that purpose, different potential energy surfaces (PESs) determined from density functional theory (DFT) energy values have been employed, based on either the Flexible - Periodic - London - Eyring - Polanyi - Sato (FPLEPS) fitting method, or the Corrugation Reducing Procedure (CRP) interpolation. While *Eley-Rideal (ER) recombination* is analyzed in the four systems, *Hot-Atom (HA)* reaction is only studied for H *abstraction*. The influence of electron–hole ($e-h$) pair excitations is investigated in detail, via the local density friction approximation (LDFA). When included, phonon excitations are introduced using the generalized langevin oscillator (GLO) model.

First, the dissipation of energy to metal surfaces upon *ER recombination* is investigated. Calculations have been carried out within the zero coverage limit under normal incidence condition. Initial collision energies E_i within the range 0.25-5.0 eV are analyzed. We have confirmed that phonon excitations are only relevant for N_2, for which they reduce the reactivity in the range of 10–50% [71–73, 76, 77]. Energy loss due to phonons is an order of magnitude smaller for H (0.01–0.1 eV) than for N (0.5–1.4 eV). Conversely, energy losses via $e-h$ pair excitations (0.4–1.1 eV for H and 0.2–0.4 eV for N) negiglibly affect *ER* reactivity of N_2, but can produce variations of the cross section for H_2 *recombination* of up to a 36%. The effects have been rationalized as a reduction of the effective collision energy. Similarly, the effect of the *e-h* pair excitations for N_2 dissociation on W(110) [124, 131] and on W(100) [131], as well as for H_2 dissociation on Cu(110) [124] have also been related to the reduction of the collision energy. Concerning the way the energy losses are distributed among the different degrees of freedom of the molecules, we observe that $e-h$ pair excitations mostly reduce the translational energy

of the molecules, whereas phonon excitations may also affect the vibrational energy of N_2. All in all, the description of the *ER* process is here refined by including dissipation channels in the dynamics. We have demonstrated that in the case of H_2 *recombination*, due to its light mass, it is mandatory to incorporate $e-h$ pair excitations and that surface movement can be neglected. On the contrary, for N_2 *recombination*, phonon excitation is the dominant mechanism, though a noticeable effect of the electronic excitations also shows up.

Second, we have investigated the stereodynamics of *ER* reactions on metal surfaces, i.e., the sensitivity of the dynamics on the initial orientation of the colliding partners. To do so, the previous four systems are further studied, under several off normal incidences for the projectile atom. Important qualitative changes on *ER* reactivity are only found for N *abstraction*. On the one hand, the energy threshold for N *abstraction* on W(100) is drastically reduced with increasing the polar incidence angle because it allows avoiding the N–N repulsion region upon approach. On the other hand, very efficient N_2 *ER abstraction* is observed at the highest polar incidence θ_i due to the appearance of a new pathway, denoted as *grazing-ER*, for which the adsorbate is captured by the projectile that passes above it before colliding with the surface and being forward scattered. Interestingly, a similar mechanism was identified in the efficient N_2 *recombination* on N-covered Ag(111) [70, 235]. The incidence angle effects have dynamical origins in N_2 *recombination* in both crystal faces, steeming from the high corrugation of the PESs. Low dependence of the energy losses on the incidence angle is found, thus previous conclusions apply regardless the angle of incidence. The partition of energy into the DOF of *ER* formed diatom does not depend on incidence angles for H *abstraction* on tungsten, while for N_2 *recombination*, stereodynamical effects are observed, in particular on W(110) at high collision energy. These essentially originate from the large contribution to reaction of the *grazing-ER* mechanism whose dynamical pathways involve very distinct dynamics. All in all, we have shown that the incidence angles of the projectile might be very relevant on the *ER* dynamics and on the product energy and angular distributions. The origin of those stereodynamical effects is the high corrugation of the PESs.

Third, we have theoretically investigated for the first time the influence of $e-h$ pair excitations on *HA abstraction* on a metal surface. H *abstraction* form W(110) at Θ= 0.25, 0.75 and 1.0 ML coverages has been studied under normal incidence conditions. *HA recombination* mechanism, which is supposed to dominate *recombination* at low coverage and low E_i, is shown to be significantly affected by the low-energy electronic excitations, since they greatly reduce the relaxation time of *hot* H *atom*. This is consistent with other works in which dissipation to electronic excitations was also found to largely dominate the relaxation of light *hot atoms* at surfaces [126, 128, 137, 138, 261, 262]. Within LDFA

both *ER* and *HA* mechanisms compete whatever the coverage, but as the coverage increases *ER* becomes the dominant *abstraction* channel. For both mechanisms, $e-h$ pair excitations mostly reduce the translational energy of the molecules. Furthermore, the simulations predict large *adsorption* probabilities, suggesting possible supersaturation in accordance with the hydrogen superstructure at Θ=1.5 ML coverage measured by Low Energy Electron Diffraction (LEED) and inelastic Helium Atom Scattering (HAS) [240]. DFT calculations confirm indeed that *adsorption* of an H atom on the saturated surface is energetically favorable by 2.07 eV at 1.025 ML. Interestingly, such adsorbing sites with lower binding energy have already been anticipated in the literature to rationalize the experimentally observed hot vibrational states distributions of H_2 molecules resulting from *abstraction* on tungsten surfaces [143, 233]. All in all, the description of the *abstraction* processes is refined here by including $e-h$ pair excitations in the dynamics, which are predicted to highly affect *HA recombination*.

Fourth, we have investigated for the first time H *abstraction* from W(100) at finite coverages. On the one hand, we analyze the influence of $e-h$ pair excitations. On the other hand, by comparing with previous results for W(110), the crystallographic anisotropy is studied. Two finite coverages (Θ=0.5 ML and 1.0 ML) are studied under normal incidence of the projectile. The results show very high similarities with the W(110) surface. Within the BOSS model, the *HA* process is shown to dominate *abstraction* of H at low coverage (Θ=0.5 ML) and low collision energy, whereas the two mechanisms compete as the coverage and/or collision energy increases. Dissipation to $e-h$ pair excitation highly affects *HA recombinaiton* at low E_i and coverage. At such conditions, energy loss by *hot atom*-adsorbate collisions is inefficient. As a consequence, electronic excitations greatly reduce the relaxation time and travelled length of *hot atoms*. As coverage increases, the efficient energy loss to the adsorbates as well as the harder access to high electronic density regions due to the adsorbates layer makes electronic excitations less important. *ER* and *HA* mechanisms compete whatever the coverage. With increasing surface coverage, the *HA* versus *ER* balance changes to make *ER* the dominant mechanism. Both processes produce vibrationally and rotationally hot molecules, which are weakly affected by coverage changes. Furthermore, very low dependence on the crystal face is observed, concerning the reactivity as well as the final energy distributions of the formed molecules. Besides, in both systems, *ER* and *primary HA* dynamics share lots of similarities that highlights the arbitrary character of their separation for H *abstraction* from tungsten.

This thesis work suggests that the role of $e-h$ pair excitations can be important on both *ER* and *HA* processes. While for H *abstraction* both recombination mechanisms have been analyzed, *ER* reaction was only studied for N_2. Although, for ER nitrogen *abstraction* phonon excitations dominate energy dissipation to the metal, the contri-

bution of $e-h$ pair excitations is not negligible. Moreover, for N *hot atoms*, phonons were previously predicted to dominate the initial stage of the *adsorption* process but a substantial excitation of $e-h$ pairs is active during the long time scales, which govern the final accommodation of the adsorbates [127, 128, 138]. Therefore, the study of *HA recombination* of N_2 is a necessary next step in order to get a wider comprehension of electronic excitations during *recombination* processes.

Regarding the stereodynamical effects on *ER* recombination processes, we have shown that they might be very pronounced when the interaction potential is highly corrugated. In principle, projectiles leading to *HA recombination* loose memory of the initial partition of energy among their degrees of freedom while they travel on the surface. Therefore, stereodynamical effects are not expected at least in the final state of the molecules. However, the incidence angle might affect the formation of *hot atoms*, i.e., the probability of an atom to be trapped on the surface, and thus, might also affect *HA* reactivity. Therefore, an extension of the work would be to study incidence angle effects on *HA recombination*.

Besides, we have shown that for H scattering off H-covered W(100) and W(110) *adsorption* is always the most probable process within the wide range of initial conditions studied in this thesis. In accordance with experimental observations [143, 233, 240], high coverages are predicted for high fluxes of gas interacting with the metal surface as in plasma wall interactions. Therefore, the simulation of higher coverages would allow to access to conditions that are important for those systems. To do so in a reliable way, however, at least three atom interactions should be included. Therefore, a important future step would be to develop a model to account for three atom interactions so that high coverages can be investigated.

Chapter X

Résumé en Français

Les processus élémentaires à l'interface gaz-solide sont intensivement étudiés [1] du fait de leur rôle important dans de nombreux phénomènes naturels ou d'intérêt technologique [2–6]. Cependant, leur description est ardue car l'interaction d'atomes et de molécules avec les surfaces est influencée par de multiples paramètres physiques tels que la température, la présence d'adsorbats, les défauts, l'énergie de collision ou encore l'angle d'incidence. Ainsi, la physique sous-jacente ne peut être précisément décrite théoriquement que dans le cadre d'une approche de dynamique. La problématique étant complexe, l'acquisition de connaissances pour l'interaction d'atomes et de petites molécules avec les surfaces est fondamentale afin d'extrapoler ensuite à des systèmes de plus grande taille.

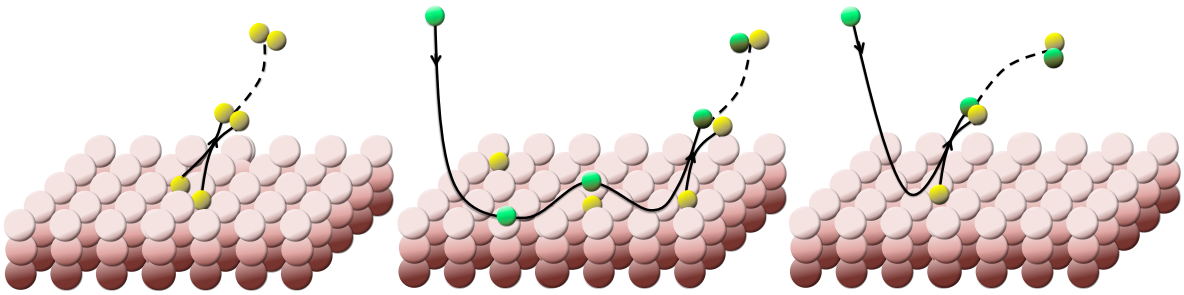

Figure X.1: Processus de recombinaison: Mécanismes *LH* (gauche), *HA* (milieu) et *ER* (droite).

Un processus élémentaire d'importance est la réaction d'*abstraction* au cours de laquelle un atome adsorbé est arraché à la surface en se combinant à un atome de la phase gazeuse (Figure X.1, milieu et droite). La recombinaison de surface peut procéder par mécanisme *Langmuir-Hinshelwood (LH)* [45], *Eley-Rideal (ER)* [46] ou *Hot-Atom (HA)* [47]. Les deux premiers peuvent être considérés comme des mécanismes limites. La réaction *LH* a lieu lorsque deux espèces adsorbées recombinent après diffusion ther-

mique en surface. Le mécanisme *ER* se produit lorsqu'un atome de la phase gazeuse entre en collision avec la surface et recombine en une seule collision, i.e. en se liant à un atome préalablement adsorbé. Le mécanisme *HA* peut être considéré comme un processus intermédiaire entre *ER* et *LH*. Initialement, l'atome incident est capturé par la surface après échange d'énergie avec cette dernière et/ou les adsorbats ou par transfert du mouvement normal vers les mouvements parallèles à la surface. Cet atome capturé est qualifié de "chaud" lorsqu'il diffuse sur la surface avant de se thermaliser. Lors de cette étape de diffusion, cet atome chaud peut recombiner avec un adsorbat.

Au cours des dernières années, la description théorique de la dynamique des processus élémentaires aux surfaces métalliques a atteint un degré de précision sans précédent grâce au développement de calculs de structure électronique basés sur la théorie de la fonctionnelle densité (DFT, Density Functional Theory) et l'explosion des capacités de calcul informatique. Bien que des traitements plus exacts soient possibles, la plupart des modèles développés sont basés sur l'approximation Born-Oppenheimer (BO), [108] de telle sorte que les transitions entre les états stationnaires électroniques sont supposées inexistantes [109]. La comparaison avec l'expérience a démontré la robustesse de cette approximation pour de nombreux processus gaz-surface [110]. En parallèle, la méthode des trajectoires quasi-classiques (QCT, Quasi Classical Trajectory Method) s'est avérée un outil de choix pour rationaliser la dynamique de réactions hétérogènes. Cependant, l'approximation BO n'est plus valide lorsque des transitions non-adiabatiques ont lieu durant la collision gaz-surface. Ces dernières ont été mis en évidence dans nombre d'expériences [115–123]. Dernièrement, diverses théories *ab initio* ont été développées pour décrire l'excitation des paires électron-trou lors des processus hétérogènes aux surfaces métalliques [1]. Parmi elles, un bon compromis entre précision et simplicité de mise en oeuvre est offert par l'approximation de friction de densité locale (LDFA, Local Density Friction Approximation) [124], comme montré en ref [125].

Si le couplage aux phonons a été étudié dans le cadre des réactions de recombinaison, l'excitation des paires $e-h$ a été jusqu'ici négligée, alors que cet effet est suggéré comme déterminant dans la cinétique de recombinaison par *HA* [136]. L'objectif principal de cette thèse est donc d'étudier, pour la première fois, l'influence des excitations electron-trou sur les mécanismes d'*abstraction HA* et *ER*. Pour cela, nous étudions le processus d'*abstraction* de l'hydrogène (H) et l'azote (N) sur des surfaces de Tungstène W(100) et W(110). Le choix des adsorbats est motivé par la connaissance acquise pour d'autres processus élémentaires étudiés théoriquement [126,128,137–139]. Alors que la relaxation des atomes d'hydrogène chauds sur le Pd(100) est entièrement gouvernée par les excitations des paires $e-h$, la dissipation aux phonons domine pour des éléments plus lourds tels que O_2, N ou N_2. Notre choix de systèmes chimiques permet donc d'acquérir une vue d'ensemble des processus d'*abstraction* non-adiabatiques. Comme les canaux de dissi-

pation de l'énergie gouvernent le temps de diffusion hyperthermique des atomes chauds, ils affecteront sensiblement la réactivité *HA*. Au contraire, lors du processus *ER*, l'étape de diffusion hyperthermique est inexistente, mais une quantité non-négligeable d'énergie libérée lors de la réaction peut être tranférée au métal. Le Tungstène a été ici choisi car il est le matériau de choix pour les composants faisant face au plasma dans les diverteurs d'ITER [13], qui doivent contrôler l'extraction des impuretés du réacteur et supporter les plus hauts flux de chaleur. Il est ainsi primordial d'étudier l'interaction d'atomes et molécules d'hydrogène avec les surfaces de Tungstène pour une large gamme d'énergies de collision, depuis l'électron-volt et bien au delà [140]. Comme des surfaces polycristallines sont utilisées pour les applications, un aspect important de notre recherche est de connaitre l'influence de la symmétrie de surfaces de bas indice de Miller, les plus abondantes dans le W polycristallin. Par ailleurs, le processus *ER* revêt un intérêt particulier car il est en général très exothermique, et par là-même, produit des molécules très excitées, [141–143] d'intérêt potentiel pour la production d'ions négatifs par attachement dissociatifs d'électrons [144]. Les approches théoriques employées dans cette thèse nous permettent d'analyser la dynamique de recombinaison de manière très détaillée. Les faibles probabilités de ces processus obligent cependant à utiliser la dynamique classique sur des surfaces d'énergie potentielle (PES) préalablement construites. Cette approche a été largement utilisée et validée pour l'étude des procesesus élémentaires. Les simulations QCT requièrent 3 étapes. Premièrement, une méthode décrivant les interactions entre les espèces en présence est nécessaire. L' approximation BO est appliquée et la DFT est ici utilisée pour calculer l' énergie potentielle d'un grand nombre de configurations des atomes/molécules en considérant la surface statique, i.e. en fixant les atomes de surface dans leur position d'équilibre (modèle BOSS, Born-Oppenheimer Static Surface). Ensuite, ces énergies sont interpolées ou ajustées pour obtenir une représentation continue des interactions, la surface d'énergie potentielle. Pour étudier la recombinaison *ER* dans la limite d'un adsorbat (taux de couverture nul), des PESs ajustées par la function FPLEPS (Flexible - Periodic - London - Eyring - Polanyi - Sato) [159–161] ont été utilisées. L'étude des recombinaisons *ER* et *HA* sur des surfaces couvertes se sont basées sur des PESs reposant dur la procédure CRP [162], dans laquelle les données sont interpolées. Finalement, les équations du mouvement classiques des noyaux - incluant les corrections semi-classiques nécessaires- sont intégrées numériquement. Ainsi, la dynamique adiabatique, i.e. sans transfert d'énergie à la surface est décrite (BOSS). Pour rationaliser les phénomènes non-adiabatiques, l'échange d'énergie aux vibrations du substrat et aux excitations électroniques est incorporé en combinant l'approximation de friction de densité locale (LDFA, Local Density Friction Approximation) [124] pour les excitations électroniques et l'oscillateur de Langevin généralisé (GLO, Generalized Langevin Oscillator) [134, 135] pour le couplage aux phonons comme proposé en Ref. [129].

En utilisant cette méthodologie, quatre études ont été menées:

1. *Abstraction Eley-Rideal* de l'azote et l'hydrogène des surfaces de tungstène: Effet de la dissipation de l'énergie.

Dans la limite d'un seul adsorbat, ce qui correspond à des taux de couverture tendant vers 0, nous avons étudié la dissipation de l'énergie due à la fois aux excitations électroniques et aux phonons pour 4 systèmes impliquant des dynamiques très distinctes à incidence normale, dans la gamme d'énergie 0.25-5 eV: (i) l'*abstraction* des atomes légers d'hydrogène sur les plans W(100) et W(110), pour laquelle l'excitation phononique est attendue être négligeable [76,77] et (ii) celle d'atomes d'azote, plus lourds, pour laquelle le mouvement de la surface peut jouer un rôle. [71–73]. La figure X.2 (gauche) montre que l'excitation phononique réduit de la réactivité de 10 à 50% dans le cas de la recombinaison de N_2 en fonction de l'énergie de collision et la symmétrie de surface. Au contraire, l'excitation des phonons n'affecte pas de manière significative l'*abstraction* de H à cause de la grande différence de masse entre l'atome incident et les atomes de surface (voir Figure X.2, droite). L'effet opposé est observé pour les excitations electron-trou. Alors qu'elles influencent de manière mineure la recombinaison de N_2, elles produisent des variations importantes de la section efficace de formation de H_2 (jusqu'à 36%).

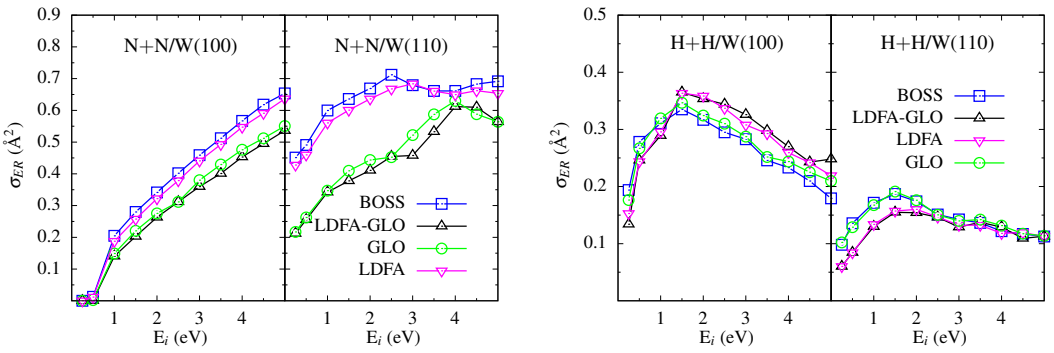

Figure X.2: Sections efficaces de recombinaison *ER*, σ_{ER}, en fonction de l'énergie de collision du projectile E_i pour le modèle BOSS (carrés bleus), LDFA (triangles renversés roses), GLO (cercles verts) et LDFA-GLO (triangles noirs).

Ces effets sont liés aux échanges d'énergie entre les atomes se recombinant et le métal, qui ont été analysés en séparant la contribution de chacun des canaux de dissipation. Alors l'énergie transférée aux électrons est 3 fois supérieure pour la recombinaison de H_2 que celle de N_2, le transfert d'énergie aux phonons est un ordre de grandeur plus important pour cette dernière.

2. Stéréodynamique de *l'abstraction Eley-Rideal* de l'azote et l'hydrogène de surfaces de Tungstène

Nous avons ici étudiés l'effet de l'angle d'incidence du projectile sur l'*abstraction ER* produisant H_2 et N_2 depuis les surfaces W(100) et W(110). La réactivité, la dissipation de l'énergie ainsi que la distribution finale de l'énergie des molécules formées ont été analysées. Des changements quantitatifs de la réactivité sont prédits pour les 4 systèmes (voir Figure X.3), tout du moins pour les angles les plus rasants. Cependant, une forte influence apparait seulement pour la recombinaison de N_2. D'une part, le seuil énergétique à la réaction sur la surface W(100) est drastiquement réduit avec l'augmentation de l'angle polaire par rapport à la normale à la surface. D'autre part, l'*abstraction ER* est très efficace aux angles les plus rasants pour la surface W(110) à cause de l'apparition d'un nouveau mécanisme, qui a été caractérisé en détail. Ces effets stéréodynamiques trouvent leur origine dans la forte corrugation de la PES pour les processus impliquant l'azote.

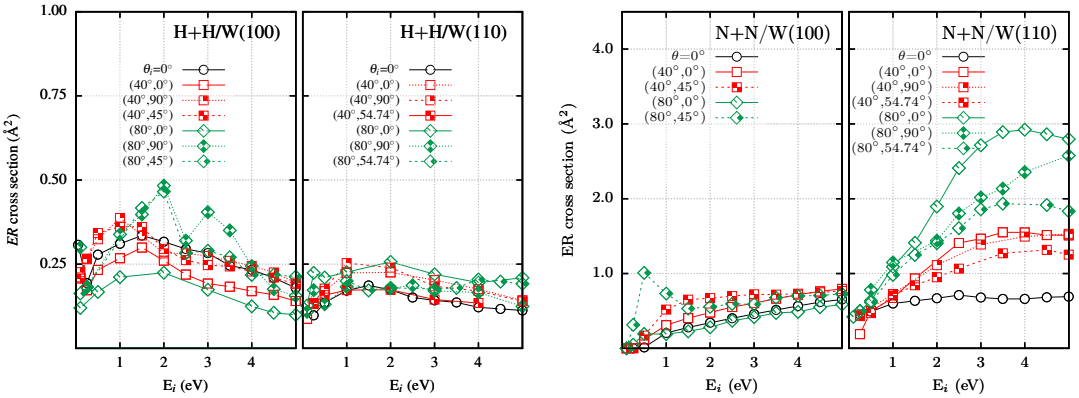

Figure X.3: Sections efficaces d'*abstraction ER*, σ_{ER}, en fonction de l'énergie de collision E_i du projectile pour H+H/W(100), H+H/W(110), N+N/W(100) et N+N/W(110). Les directions d'incidence (θ_i,ϕ_i) sont indiquées sur chaque graphe.

L'énergie dissipée au métal par excitation des phonons et des paires électron-trou est analysée. Les conclusions principales sont identiques à celles de l'incidence normale. Les pertes d'énergie moyennes sont dans la gamme 0.5-2.0 eV, augementant avec l'énergie de collision E_i et dépendent peu de l'incidence.

3. Dynamique non-adiabatique de l'*abstraction* de l'hydrogène de la surface W(110) à taux de couverture fini.

L'effet des excitations électroniques concomittantes à l'*abstraction* de l'hydrogène sur la surface W(110) à taux de couverture fini est étudié. La figure X.4 (haut) montre que, bien que cette dissipation de l'énergie favorise l'*adsorption* aux dépens de *absorption*, *reflexion* et *abstraction*, l'évolution qualitative de ces trois mécanismes avec l'énergie de collision E_i change peu.

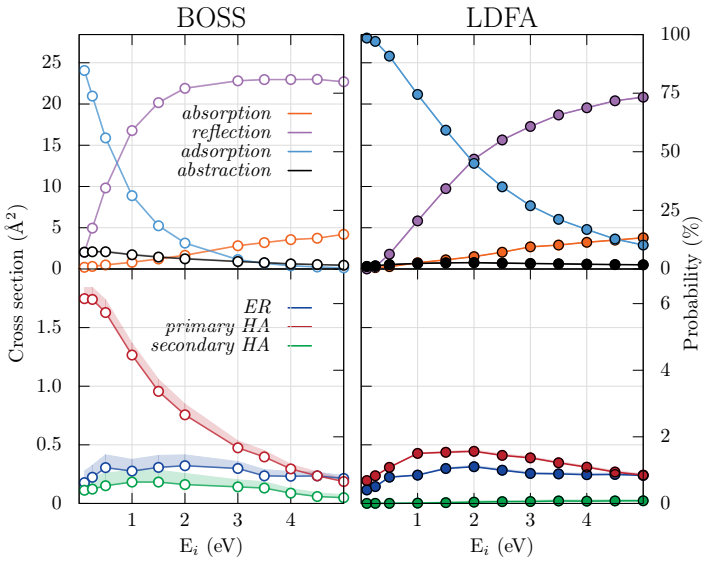

Figure X.4: Haut: Section efficaces par adsorbat pour l'*adsorption* (bleu), *absorption* (orange), la *réflexion* (violet) et l'*abstraction* (noir) en fonction de l'énergie d'incidence, E_i. Bas: Sections efficaces par adsorbat pour *ER* (bleu), *HA primaires* (rouge) et *HA secondaires* (vert) en fonction de l'énergie d'incidence, E_i. L'échelle de droite correspond à la probabilité. Les graphes de gauche (droite) correspondent aux modèles BOSS (LDFA). La couverture de surface est 0.25 ML. Les incertitudes théoriques, (voir chapitre XXX), sont représentées par des domaines ombrés quand leur contribution est supérieure à la taille des symboles.

Il apparait que, en tenant compte des excitations électroniques (modèles LDFA), les mécanismes *ER* et *HA* sont en compétition quel que soit le taux de couverture, mais lorsque le recouvrement augmente, le processus *ER* devient le processus réactif dominant.

4. Dynamique adiabatique et non-adiabatique d'abstraction de l'hydrogène de la surface W(100) à taux de couverture fini.

Nous avons étudié l'*abstraction* de l'hydrogene de la surface W(100) à taux de couverture fini (Θ=0.5 ML and 1.0 ML). Dans l'approximation BOSS, le processus *HA* domine la recombinaison de H_2 à faible recouvrement (Θ = 0.5 ML) et basse énergie de collision (E_i<2.0 eV). Lorsque le taux de couverture augmente, la balance entre les réactivités *HA* et *ER* change en faveur de *ER* qui devient le processus dominant (Θ = 1.0 ML). De plus, le temps *abstraction* décroit et les processus *HA* et *ER* se déroulent sur la même échelle de temps.

Comme pour la symmétrie 110 de surface, l'effet des excitations électroniques est de favoriser l'*adsorption* au dépens de l'*absorption*, la *réflexion* et l'*abstraction*. L'*abstraction* est drastiquement réduite à faible énergie d'incidence E_i et faible recouvrement. Comme précédemment, le processus *HA* est significativement affecté par les excitations électroniques, qui provoquent une diminution importante du temps de relaxation et de la distance parcourue par les atoms chauds sur la surface W(100). Comme illustré en figure X.5,

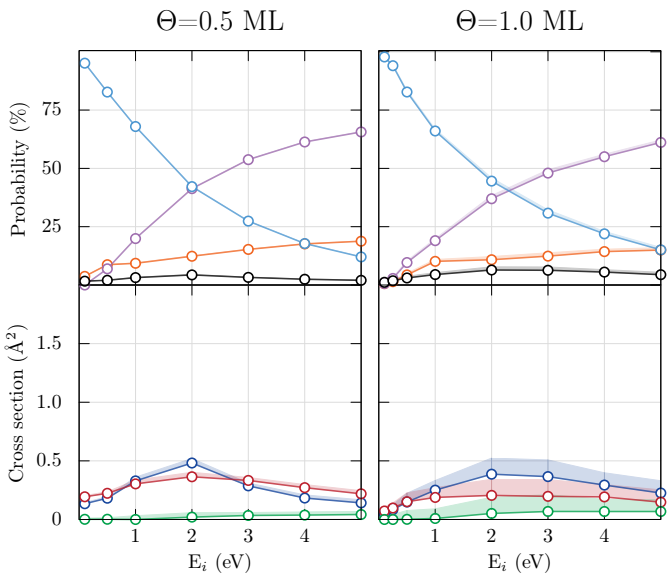

Figure X.5: Haut: Probabilité de réaction de l'*adsorption* (bleu), l'*absorption* (violet), la *réflexion* (orange) et l'*abstraction* (noir) en fonction de l'énergie d'incidence. Bas: Sections efficaces des processus *ER* (bleu), *HA primaire* (rouge) et *HA secondaire* (green) en fonction de E_i. Les graphes de gauche et droite correspondent à des taux de couverture de 0.5 and 1.0 ML, respectivement. Les incertitudes théoriques, (voir chapitre XXX),sont représentées par des domaines ombrés quand leur contribution est plus grande que la taille des symboles.

les deux mécanismes d'abstractions impliquent une réactivité similaires et l'abstraction *ER* devient majoritaire lorsque le recouvrement augmente. La comparaison des résultats de simulation pour l'*abstraction* de H des surfaces W(100) et W(110) montre une faible sensibilité à la symmétrie de surface, que ce soit en termes de réactivité ou de distribution de l'énergie sur les degrés de liberté des molécules formées.

En conclusion, cette thèse a permis d'étudier, pour la première fois, d'un point de vue théorique, l'influence des effets non-adiabatiques sur les processus d'abstraction atomique.

Publications

List of publications related with this thesis:

- **Hydrogen Abstraction from Metal Surfaces: When Electron–Hole Pair Excitations Strongly Affect Hot-Atom Recombination**
  O. Galparsoro, R. Pétuya, H.F. Busnengo, J.I. Juaristi, C. Crespos, M. Alducin, P. Larrégaray;
  Physical Chemistry Chemical Physics Communication, **2016**.
  DOI: 10.1039/C6CP06222A

- **Energy Dissipation to Tungsten Surfaces upon Eley–Rideal Recombination of N_2 and H_2**
  O. Galparsoro, R. Pétuya, J.I. Juaristi, C. Crespos, M. Alducin, P. Larrégaray;
  The Journal of Physical Chemistry C, 119 (27), 15434-15442, **2015**.

- **Stereodynamics of diatom formation through Eley–Rideal reactions**
  O. Galparsoro, J.I. Juaristi, C. Crespos, M. Alducin, P. Larrégaray;
  In preparation

- **Adiabatic and non–adiabatic dynamics of H+H primary recombination on W(100) at finite coverages**
  O. Galparsoro, H. F. Busnengo, A. Martinez, J.I. Juaristi, C. Crespos, M. Alducin, P. Larrégaray;
  In preparation

- **Coverage influence in H abstraction dynamics on W(100) and W(110)**
  O. Galparsoro, H. F. Busnengo, A. Martinez, J.I. Juaristi, C. Crespos, M. Alducin, P. Larrégaray;
  In preparation

List of publications not related with this thesis:

- **Modeling surface motion effects in N_2 dissociation on W(110): Ab initio molecular dynamics calculations and generalized Langevin oscillator model**
  F. Nattino, O. Galparsoro, F. Costanzo, R.D. Muiño, M. Alducin, G.J. Kroes;
  The Journal of Chemical Physics, 144 (24), 244708, **2016**

Bibliography

[1] R. Díez Muiño, H. Busnengo, *Dynamics of Gas-Surface Interactions: Atomic-level Understanding of Scattering Processes at Surfaces*, Springer Series in Surface Sciences (Springer, 2013). (Cited on pages 1, 5, 6, 7, 22, 24, 27, 105, and 106.)

[2] J. M. Thomas, W. J. Thomas, *Principles and Practice of Heterogeneous Catalysis* (WCH, Weinheim, 1997). (Cited on pages 1 and 105.)

[3] G. A. Somorjai, *Introduction to Surface Chemistry and Catalysis* (Wiley, New York, 1994). (Cited on pages 1 and 105.)

[4] A. M. Thayer, *Chem. Eng. News* **March 9**, 27 (1992). (Cited on pages 1 and 105.)

[5] F. Zaera, *Prog. Surf. Sci.* **69**, 1 (2001). (Cited on pages 1 and 105.)

[6] V. P. Zhdanov, *Surf. Sci.* **500**, 966 (2002). (Cited on pages 1 and 105.)

[7] M. J. Molina, L. T. Molina, D. M. Golden, *J. Phys. Chem.* **100**, 12888 (1996). (Cited on page 1.)

[8] J. M. Greenberg, *Surf. Sci.* **500**, 793 (2002). (Cited on page 1.)

[9] J. S. Mathis, *Rep. Prog. Phys.* **56**, 605 (1993). (Cited on page 1.)

[10] G. Winnewisser, E. Herbst, *Rep. Prog. Phys.* **56**, 1209 (1993). (Cited on page 1.)

[11] B. Halpern, D. E. Rosner, *J. Chem. Soc., Faraday Trans. 1* **74**, 1883 (1978). (Cited on pages 1 and 55.)

[12] L. Martin-Gondre, Contribution théorique à l'étude de la réactivité élémentaire gaz-surface d'intérêt en rentrée atmosphérique, Ph.D. thesis, Université Bordeaux 1 (2009). (Cited on pages 1, 22, and 23.)

[13] https://www.iter.org/mach/divertor. (Cited on pages 1, 8, and 107.)

[14] D. S. M.-C. Desjonquères, *Concepts in Surface Physics*, Springer Series in Surface Sciences 30 (Springer Berlin Heidelberg, 1993). (Cited on page 2.)

[15] K. Horn, J. DiNardo, W. Eberhardt, H.-J. Freund, E. Plummer, *Surf. Sci.* **118**, 465 (1982). (Cited on page 2.)

[16] R. Gomer, *Rep. Prog. Phys.* **53**, 917 (1990). (Cited on page 2.)

[17] G. Pacchioni, *Surf. Sci.* **281**, 207 (1993). (Cited on page 2.)

[18] J. H. McCreery, G. Wolken, *J. Chem. Phys.* **63**, 2340 (1975). (Cited on pages 3 and 22.)

[19] A. Kara, A. E. DePristo, *J. Chem. Phys.* **88**, 5240 (1988). (Cited on page 3.)

[20] M. Alducin, R. Díez Muiño, H. F. Busnengo, A. Salin, *Phys. Rev. Lett.* **97**, 056102 (2006). (Cited on pages 3, 23, and 40.)

[21] M. Alducin, R. Díez Muiño, H. F. Busnengo, A. Salin, *J. Chem. Phys.* **125**, 144705 (2006). (Cited on pages 3, 23, 24, and 40.)

[22] M. Alducin, R. D. Muiño, H. Busnengo, A. Salin, *Surf. Sci.* **601**, 3726 (2007). Proceedings of the 24th European Conference on Surface Science. (Cited on page 3.)

[23] A. Salin, *J. Chem. Phys.* **124**, 104704 (2006). (Cited on pages 3, 23, and 43.)

[24] G. Volpilhac, A. Salin, *Surf. Sci.* **556**, 129 (2004). (Cited on pages 3, 24, 25, and 40.)

[25] C. Díaz, *et al.*, *Phys. Rev. Lett.* **96**, 096102 (2006). (Cited on page 3.)

[26] C. Díaz, F. Martín, H. Busnengo, A. Salin, *J. Chem. Phys.* **120**, 321 (2004). (Cited on page 3.)

[27] G. Kresse, *Phys. Rev. B* **62**, 8295 (2000). (Cited on page 3.)

[28] C. Crespos, H. Busnengo, W. Dong, A. Salin, *J. Chem. Phys.* **114**, 10954 (2001). (Cited on page 3.)

[29] L. Martin-Gondre, *et al.*, *Chem. Phys. Lett.* **471**, 136 (2009). (Cited on pages 3, 22, and 23.)

[30] I. Goikoetxea, M. Alducin, R. D. Muiño, J. I. Juaristi, *Phys. Chem. Chem. Phys.* **14**, 7471 (2012). (Cited on page 3.)

[31] M. Alducin, H. F. Busnengo, R. Díez-Muiño, *J. Chem. Phys.* **129**, 224702 (2008). (Cited on page 3.)

[32] A. Gross, M. Scheffler, *Phys. Rev. B* **57**, 2493 (1998). (Cited on pages 3 and 27.)

[33] G. J. Kroes, A. Gross, E. J. Baerends, M. Scheffler, D. A. McCormack, *Acc. Chem. Res.* **35**, 193 (2002). (Cited on page 3.)

[34] C. Díaz, R. Olsen, H. Busnengo, G. Kroes, *J. Phys. Chem. C* **114**, 11192 (2010). (Cited on page 3.)

[35] G. A. Somorjai, *J. Phys. Chem. B* **104**, 1969 (2000). (Cited on page 3.)

[36] T. A. Baker, B. Xu, X. Liu, E. Kaxiras, C. M. Friend, *J. Phys. Chem. C* **113**, 16561 (2009). (Cited on page 3.)

[37] P. Ferrin, S. Kandoi, A. U. Nilekar, M. Mavrikakis, *Surf. Sci.* **606**, 679 (2012). (Cited on pages 3 and 4.)

[38] M. Nezafati, *et al.*, *Comut. Mater. Sci.* **105**, 18 (2015). (Cited on page 3.)

[39] M. Nezafati, *et al.*, *Acta Materialia* **115**, 295 (2016). (Cited on page 3.)

[40] K. A. Peterlinz, S. J. Sibener, *J. Phys. Chem.* **99**, 2817 (1995). (Cited on page 3.)

[41] J. V. G. Alefeld, *Hydrogen in Metals I: Basic Properties*, Topics in Applied Physics 28 (Springer Berlin Heidelberg, 1978). (Cited on page 4.)

[42] A. D. Johnson, S. P. Daley, A. L. Utz, S. T. Ceyer, *Science* **257**, 223 (1992). (Cited on page 4.)

[43] M. Wilde, K. Fukutani, *Phys. Rev. B* **78**, 115411 (2008). (Cited on page 4.)

[44] K. Gibson, D. Killelea, S. Sibener, *J. Phys. Chem. C* **118**, 14977 (2014). (Cited on page 4.)

[45] I. Langmuir, *Trans. Faraday Soc.* **17**, 607 (1922). (Cited on pages 4 and 105.)

[46] D. D. Eley, E. K. Rideal, *Nature* **146**, 401 (1940). (Cited on pages 4 and 105.)

[47] J. Harris, B. Kasemo, *Surf. Sci.* **105**, L281 (1981). (Cited on pages 4 and 105.)

[48] Z. B. Guvenc, X. Sha, B. Jackson, *J. Chem. Phys.* **115**, 9018 (2001). (Cited on pages 4, 5, 35, and 39.)

[49] D. V. Shalashilin, B. Jackson, M. Persson, *J. Chem. Phys.* **110**, 11038 (1999). (Cited on pages 4, 5, and 35.)

[50] S. Caratzoulas, B. Jackson, M. Persson, *J. Chem. Phys.* **107**, 6420 (1997). (Cited on page 4.)

[51] Z. B. Guvenc, X. Sha, B. Jackson, *J. Phys. Chem. B* **106**, 8342 (2002). (Cited on pages 4 and 39.)

[52] B. Jackson, M. Persson, *Surf. Sci.* **269**, 195 (1992). (Cited on page 4.)

[53] B. Jackson, D. Lemoine, *J. Chem. Phys.* **114**, 474 (2001). (Cited on page 4.)

[54] B. Jackson, X. Sha, Z. B. Guvenc, *J. Chem. Phys.* **116**, 2599 (2002). (Cited on page 4.)

[55] C. Kalyanaraman, D. Lemoine, B. Jackson, *Phys. Chem. Chem. Phys.* **1**, 1351 (1999). (Cited on pages 4 and 55.)

[56] P. Kratzer, W. Brenig, *Surf. Sci.* **254**, 275 (1991). (Cited on pages 4 and 55.)

[57] G. Lanzani, R. Martinazzo, G. Materzanini, I. Pino, G. F. Tantardini, *Theor. Chem. Acc.* **117**, 805 (2007). (Cited on page 4.)

[58] R. Martinazzo, S. Assoni, G. Marinoni, G. F. Tantardini, *J. Chem. Phys.* **120**, 8761 (2004). (Cited on pages 4, 5, and 35.)

[59] M. Persson, B. Jackson, *J. Chem. Phys.* **102**, 1078 (1995). (Cited on pages 4, 34, 37, 39, and 55.)

[60] J. G. Quattrucci, B. Jackson, D. Lemoine, *J. Chem. Phys.* **118**, 2357 (2003). (Cited on pages 4 and 35.)

[61] M. Rutigliano, M. Cacciatore, *Phys. Chem. Chem. Phys.* **13**, 7475 (2011). (Cited on pages 4 and 55.)

[62] D. V. Shalashilin, B. Jackson, *J. Chem. Phys.* **109**, 2856 (1998). (Cited on page 4.)

[63] H. K. Shin, *Chem. Phys. Lett.* **244**, 235 (1995). (Cited on page 4.)

[64] J. C. Tully, *J. Chem. Phys.* **73**, 6333 (1980). (Cited on page 4.)

[65] C. Stampfl, M. Scheffler, *Surf. Sci.* **433**, 119 (1999). (Cited on page 4.)

[66] W. K. Kim, J. Ree, H. K. Shin, *J. Phys. Chem. A* **103**, 411 (1999). (Cited on page 4.)

[67] M. Cacciatore, M. Rutigliano, G. D. Billing, *J. Thermophys. Heat Transfer* **13**, 195 (1999). (Cited on page 4.)

[68] D. Lemoine, J. G. Quattrucci, B. Jackson, *Phys. Rev. Lett.* **89**, 268302 (2002). (Cited on pages 4, 5, 39, and 63.)

[69] J. G. Quattrucci, B. Jackson, *J. Chem. Phys.* **122**, 074705 (2005). (Cited on pages 4, 5, 8, 40, and 63.)

[70] M. Blanco-Rey, *et al.*, *J. Phys. Chem. Lett.* **4**, 3704 (2013). (Cited on pages 4, 5, 39, 62, and 102.)

[71] E. Quintas-Sánchez, *et al.*, *J. Chem. Phys.* **137**, 064709 (2012). (Cited on pages 4, 39, 40, 41, 42, 47, 55, 58, 101, and 108.)

[72] E. Quintas-Sánchez, *et al.*, *J. Chem. Phys.* **138**, 024706 (2013). (Cited on pages 4, 39, 40, 41, 42, 52, 55, 101, and 108.)

[73] E. Quintas-Sánchez, P. Larrégaray, C. Crespos, *J. Phys. Chem. C* **118**, 12224 (2014). (Cited on pages 4, 39, 40, 55, 58, 101, and 108.)

[74] M. Persson, B. Jackson, *Chem. Phys. Lett.* **237**, 468 (1995). (Cited on pages 4 and 5.)

[75] M. Bonfanti, S. Casolo, G. F. Tantardini, R. Martinazzo, *Phys. Chem. Chem. Phys.* **13**, 16680 (2011). (Cited on pages 4 and 39.)

[76] R. Pétuya, P. Larrégaray, C. Crespos, H. F. Busnengo, A. E. Martínez, *J. Chem. Phys.* **141**, 024701 (2014). (Cited on pages 4, 22, 24, 25, 34, 39, 40, 41, 42, 43, 72, 73, 92, 96, 101, and 108.)

[77] R. Pétuya, C. Crespos, E. Quintas-Sánchez, P. Larrégaray, *J. Phys. Chem. C* **118**, 11704 (2014). (Cited on pages 4, 34, 39, 40, 55, 64, 73, 88, 92, 96, 101, and 108.)

[78] R. Pétuya, *et al.*, *J. Phys. Chem. C* **119**, 3171 (2015). (Cited on pages 4, 5, 25, 55, 71, 72, 73, 74, 78, 79, 92, and 93.)

[79] R. Pétuya, *et al.*, *J. Phys. Chem. C* **119**, 15325 (2015). (Cited on page 4.)

[80] O. Galparsoro, *et al.*, *J. Phys. Chem. C* **119**, 15434 (2015). (Cited on pages 4, 55, 56, and 64.)

[81] T. Kammler, J. Lee, J. Küppers, *J. Chem. Phys.* **106**, 7362 (1997). (Cited on pages 4, 5, and 83.)

[82] J. Y. Kim, J. Lee, *Phys. Rev. Lett.* **82**, 1325 (1999). (Cited on pages 4 and 5.)

[83] J. Y. Kim, J. Lee, *J. Chem. Phys.* **113**, 2856 (2000). (Cited on pages 4 and 55.)

[84] C. T. Rettner, D. J. Auerbach, *Phys. Rev. Lett.* **74**, 4551 (1995). (Cited on pages 4, 5, 39, and 63.)

[85] C. T. Rettner, *J. Chem. Phys.* **101**, 1529 (1994). (Cited on pages 4, 8, 39, 40, and 63.)

[86] C. T. Rettner, D. J. Auerbach, *Science* **263**, 365 (1994). (Cited on pages 4 and 5.)

[87] S. Wehner, J. Küppers, *J. Chem. Phys.* **108**, 3353 (1998). (Cited on page 4.)

[88] S. Wehner, J. Küppers, *J. Chem. Phys.* **109**, 294 (1998). (Cited on page 4.)

[89] T. Kammler, J. Küppers, *J. Chem. Phys.* **111**, 8115 (1999). (Cited on page 4.)

[90] C. T. Rettner, *Phys. Rev. Lett.* **69**, 383 (1992). (Cited on pages 4, 5, 39, and 63.)

[91] M. Cacciatore, E. Christoffersen, M. Rutigliano, *J. Chem. Phys. A* **108**, 8810 (2004). (Cited on pages 4 and 55.)

[92] H. Ueta, M. A. Gleeson, A. W. Kleyn, *J. Chem. Phys.* **135**, 074702 (2011). (Cited on pages 4 and 5.)

[93] L. Diekhöner, *et al.*, *J. Chem. Phys.* **117**, 5018 (2002). (Cited on page 4.)

[94] K. R. Lykke, B. D. Kay, *Proc. SPIE* **1208**, 18 (1990). (Cited on pages 4 and 5.)

[95] D. Kolovos-Vellianitis, J. Küppers, *J. Phys. Chem. B* **107**, 2559 (2003). (Cited on pages 4 and 83.)

[96] G. Krenn, *et al.*, *Surf. Sci.* **445**, 343 (2000). (Cited on page 4.)

[97] M. Kori, B. L. Halpern, *Chem. Phys. Lett.* **98**, 32 (1983). (Cited on page 4.)

[98] J. Libuda, H.-J. Freund, *Surf. Sci. Rep.* **57**, 157 (2005). (Cited on pages 5 and 6.)

[99] M. P. Schmid, P. Maroni, R. D. Beck, T. R. Rizzo, *Rev. Sci. Instrum.* **74**, 1 (2003). (Cited on page 5.)

[100] R. Beck, *et al.*, *Science* **302**, 98 (2003). (Cited on page 5.)

[101] P. Maroni, *et al.*, *Phys. Rev. Lett.* **94**, 246104 (2005). (Cited on page 5.)

[102] C. Rettner, D. Auerbach, J. Tully, A. Kleyn, *J. Phys. Chem.* **100**, 13021 (1996). (Cited on pages 5 and 63.)

[103] R. N. Zare, *Science* **279**, 1875 (1998). (Cited on page 5.)

[104] M. Ashfold, J. Howe, *Annu. Rev. Phys. Chem.* **45**, 57 (1994). (Cited on page 6.)

[105] J. Polanyi, *Journal of Quantitative Spectroscopy and Radiative Transfer* **3**, 471 (1963). (Cited on page 6.)

[106] J. L. Kinsey, *Annu. Rev. Phys. Chem.* **28**, 349 (1977). (Cited on page 6.)

[107] M. Dantus, M. J. Rosker, A. H. Zewail, *J. Chem. Phys.* **87**, 2395 (1987). (Cited on page 6.)

[108] M. R. Radeke, E. A. Carter, *Annu. Rev. Phys. Chem.* **48**, 243 (1997). (Cited on pages 6 and 106.)

[109] J. Kohanoff, *Electronic structure calculations for solids and molecules: theory and computational methods* (Cambridge University Press, 2006). (Cited on pages 6 and 106.)

[110] G.-J. Kroes, C. Díaz, *Chemical Society Reviews* (2016). (Cited on pages 7 and 106.)

[111] M. Kay, G. Darling, S. Holloway, J. White, D. Bird, *Chem. Phys. Lett.* **245**, 311 (1995). (Cited on page 7.)

[112] G. Kroes, E. Baerends, R. Mowrey, *Phys. Rev. Lett.* **78**, 3583 (1997). (Cited on page 7.)

[113] A. Groß, *Surf. Sci. Rep.* **32**, 291 (1998). (Cited on pages 7, 14, 27, and 28.)

[114] G.-J. Kroes, *Prog. Surf. Sci.* **60**, 1 (1999). (Cited on pages 7 and 27.)

[115] B. Gergen, H. Nienhaus, W. H. Weinberg, E. W. McFarland, *Science* **294**, 2521 (2001). (Cited on pages 7, 30, 39, 71, and 106.)

[116] B. Gergen, S. Weyers, H. Nienhaus, W. Weinberg, E. McFarland, *Surf. Sci.* **488**, 123 (2001). (Cited on pages 7, 30, 39, 71, and 106.)

[117] H. Nienhaus, *et al.*, *Appl. Phys. Lett.* **74**, 4046 (1999). (Cited on pages 7, 30, 39, 71, and 106.)

[118] H. Nienhaus, *et al.*, *Phys. Rev. Lett.* **82**, 446 (1999). (Cited on pages 7, 30, 39, 71, and 106.)

[119] E. Hasselbrink, *Surf. Sci.* **603**, 1564 (2009). (Cited on pages 7, 30, 39, 71, and 106.)

[120] E. Hasselbrink, *Curr. Opin. Solid St. M.* **10**, 192 (2006). (Cited on pages 7, 30, 39, 71, and 106.)

[121] B. Mildner, E. Hasselbrink, D. Diesing, *Chem. Phys. Lett.* **432**, 133 (2006). (Cited on pages 7, 30, 39, 71, and 106.)

[122] B. Kasemo, E. Törnqvist, L. Walldén, *Mater. Sci. and Eng.* **42**, 23 (1980). (Cited on pages 7, 30, 39, 71, and 106.)

[123] I. Rahinov, *et al.*, *Phys. Chem. Chem. Phys.* **13**, 12680 (2011). (Cited on pages 7, 30, 39, 71, and 106.)

[124] J. I. Juaristi, M. Alducin, R. Díez Muiño, H. F. Busnengo, A. Salin, *Phys. Rev. Lett.* **100**, 116102 (2008). (Cited on pages 7, 30, 43, 45, 52, 101, 106, and 107.)

[125] J. C. Tremblay, S. Monturet, P. Saalfrank, *Phys. Rev. B* **81**, 125408 (2010). (Cited on pages 7, 30, and 106.)

[126] M. Blanco-Rey, *et al.*, *Phys. Rev. Lett.* **112**, 103203 (2014). (Cited on pages 7, 8, 30, 46, 50, 71, 102, and 106.)

[127] L. Martin-Gondre, G. A. Bocan, M. Alducin, J. I. Juaristi, R. Díez Muiño, *Comp. Theor. Chem.* **990**, 126 (2012). (Cited on pages 7, 30, 71, and 104.)

[128] D. Novko, M. Blanco-Rey, J. I. Juaristi, M. Alducin, *Phys. Rev. B* **92**, 201411 (2015). (Cited on pages 7, 8, 30, 46, 71, 73, 93, 102, 104, and 106.)

[129] L. Martin-Gondre, M. Alducin, G. A. Bocan, R. Díez Muiño, J. I. Juaristi, *Phys. Rev. Lett.* **108**, 096101 (2012). (Cited on pages 7, 27, 30, 47, 50, and 107.)

[130] A. S. Muzas, *et al.*, *J. Chem. Phys.* **137**, 064707 (2012). (Cited on page 7.)

[131] I. Goikoetxea, J. I. Juaristi, M. Alducin, R. Díez Muiño, *J. Phys.: Condens. Matter* **21**, 264007 (2009). (Cited on pages 7, 30, 43, and 101.)

[132] X. Luo, B. Jiang, J. I. Juaristi, M. Alducin, H. Guo, *J. Chem. Phys.* **145**, 044704 (2016). (Cited on page 7.)

[133] B. Jiang, M. Alducin, H. Guo, *J. Phys. Chem. Lett.* **7**, 327 (2016). (Cited on page 7.)

[134] J. C. Tully, *J. Chem. Phys.* **73**, 1975 (1980). (Cited on pages 7, 32, 34, 52, and 107.)

[135] H. F. Busnengo, W. Dong, A. Salin, *Phys. Rev. Lett.* **93**, 236103 (2004). (Cited on pages 7, 32, 33, 34, 52, and 107.)

[136] D. Kolovos-Vellianitis, J. Küppers, *Surf. Sci.* **548**, 67 (2004). (Cited on pages 8, 71, 83, and 106.)

[137] D. Novko, M. Blanco-Rey, J. Juaristi, M. Alducin, *Nucl. Instr. Meth. B* **382**, 26 (2016). (Cited on pages 8, 30, 46, 71, 102, and 106.)

[138] M. A. D. Novko, M. Blanco-Rey, J. I. Juaristi, *Phys. Rev. B* **93**, 245435 (2016). (Cited on pages 8, 30, 46, 71, 102, 104, and 106.)

[139] I. Goikoetxea, *et al.*, *New J. Phys.* **14**, 013050 (2012). (Cited on pages 8 and 106.)

[140] V. Barabash, G. Federici, R. Matera, A. R. Raffray, I. H. Teams, *Phys. Scr.* **T81**, 74 (1999). (Cited on pages 8 and 107.)

[141] R. I. Hall, I. Čadež, M. Landau, F. Pichou, C. Schermann, *Phys. Rev. Lett.* **60**, 337 (1988). (Cited on pages 8, 55, and 107.)

[142] P. J. Eenshuistra, J. H. M. Bonnie, J. Los, H. J. Hopman, *Phys. Rev. Lett.* **60**, 341 (1988). (Cited on pages 8, 55, and 107.)

[143] S. Markelj, I. Čadež, *J. Chem. Phys.* **134**, 124707 (2011). (Cited on pages 8, 55, 79, 103, 104, and 107.)

[144] S. Béchu, D. Lemoine, M. Bacal, A. Bès, J. Pelletier, *AIP Conf. Proc.* **1097**, 74 (2009). (Cited on pages 8 and 107.)

[145] M. Born, R. Oppenheimer, *Ann. Physik* **389**, 457 (1927). (Cited on page 13.)

[146] P. Hohenberg, W. Kohn, *Phys. Rev.* **136**, B864 (1964). (Cited on page 14.)

[147] W. Kohn, L. J. Sham, *Phys. Rev.* **140**, A1133 (1965). (Cited on page 15.)

[148] W. Kohn, L. J. Sham, *Phys. Rev.* **140**, A1133 (1965). (Cited on page 15.)

[149] R. O. Jones, O. Gunnarsson, *Rev. Mod. Phys.* **61**, 689 (1989). (Cited on page 16.)

[150] J. P. Perdew, K. Burke, M. Ernzerhof, *Phys. Rev. Lett.* **77**, 3865 (1996). (Cited on page 16.)

[151] B. Hammer, L. B. Hansen, J. K. Nørskov, *Phys. Rev. B* **59**, 7413 (1999). (Cited on page 16.)

[152] R. M. Martin, *Electronic Structure: Basic Theory and Practical Methods*, vol. Vol 1 (Cambridge University Press, 2004). (Cited on page 17.)

[153] F. Bloch, *Zeitschrift für physik* **52**, 555 (1929). (Cited on page 17.)

[154] M. C. Payne, M. P. Teter, D. C. Allan, T. Arias, J. Joannopoulos, *Rev. Mod. Phys.* **64**, 1045 (1992). (Cited on page 18.)

[155] J. C. Phillips, *Phys. Rev.* **112**, 685 (1958). (Cited on page 18.)

[156] J. C. Phillips, L. Kleinman, *Phys. Rev.* **116**, 287 (1959). (Cited on page 18.)

[157] M. L. Cohen, V. Heine, *Solid State Phys.* **24**, 37 (1970). (Cited on page 18.)

[158] H. J. Monkhorst, J. D. Pack, *Phys. Rev. B* **13**, 5188 (1976). (Cited on pages 18 and 84.)

[159] L. Martin-Gondre, *et al.*, *Chem. Phys. Lett.* **471**, 136 (2009). (Cited on pages 21, 22, 25, 40, and 107.)

[160] L. Martin-Gondre, *et al.*, *J. Chem. Phys.* **132**, 204501 (2010). (Cited on pages 21, 25, 40, and 107.)

[161] L. Martin-Gondre, *et al.*, *Chem. Phys.* **367**, 136 (2010). (Cited on pages 21, 25, 40, and 107.)

[162] P. N. Abufager, C. Crespos, H. F. Busnengo, *Phys. Chem. Chem. Phys.* **9**, 2258 (2007). (Cited on pages 21, 23, 25, and 107.)

[163] F. London, *Zeitschrift für Elektrochemie und angewandte physikalische Chemie* **35**, 552 (1929). (Cited on page 21.)

[164] S. Glasstone, K. J. Laidler, H. Eyring, *The theory of rate processes : the kinetics of chemical reactions, viscosity, diffusion and electrochemical phenomena* (New York : McGraw-Hill, 1941), first edn. Bibliographical foot-notes. (Cited on page 21.)

[165] S. Sato, *J. Chem. Phys.* **23**, 592 (1955). (Cited on page 21.)

[166] S. Sato, *J. Chem. Phys.* **23**, 2465 (1955). (Cited on page 21.)

[167] J. Connor, *Comput. Phys. Commun.* **17**, 117 (1979). (Cited on page 21.)

[168] D. G. Truhlar, R. Steckler, M. S. Gordon, *Chem. Rev.* **87**, 217 (1987). (Cited on page 21.)

[169] J. H. McCreery, G. Wolken, *J. Chem. Phys.* **67**, 2551 (1977). (Cited on page 22.)

[170] M. Somers, S. Kingma, E. Pijper, G. Kroes, D. Lemoine, *Chem. Phys. Lett.* **360**, 390 (2002). (Cited on page 22.)

[171] S. Nave, D. Lemoine, M. Somers, S. Kingma, G. Kroes, *J Chem Phys* **122**, 1 (2005). (Cited on page 22.)

[172] L. Martin-Gondre, *et al.*, *Chem. Phys.* **367**, 136 (2010). (Cited on pages 22 and 23.)

[173] L. Martin-Gondre, *et al.*, *J. Chem. Phys.* **132**, 204501 (2010). (Cited on pages 22 and 23.)

[174] E. Quintas-Sánchez, Descripción teórica de la dinámica de recombinación Eley–Rideal de moléculas de nitrógeno sobre superficies de tungsteno(100), Ph.D. thesis, Instituto Superior de Tecnologías y Ciencias Aplicadas, La Habana, Cuba (2013). (Cited on page 23.)

[175] G. A. Bocan, R. Díez Muiño, M. Alducin, H. F. Busnengo, A. Salin, *J. Chem. Phys.* **128**, 154704 (2008). (Cited on pages 23 and 40.)

[176] C. Díaz, *et al.*, *Science* **326**, 832 (2009). (Cited on page 23.)

[177] A. Lozano, A. Gross, H. Busnengo, *Phys. Chem. Chem. Phys.* **11**, 5814 (2009). (Cited on page 24.)

[178] M. Luppi, R. Olsen, E. Baerends, *Phys. Chem. Chem. Phys.* **8**, 688 (2006). (Cited on page 24.)

[179] D. V. Shalashilin, B. Jackson, M. Persson, *Faraday Discuss.* **110**, 287 (1998). (Cited on page 25.)

[180] D. Woodruff, *Surface Dynamics*, The Chemical Physics of Solid Surfaces 11 (Academic Press, Elsevier, 2003). (Cited on pages 27, 28, and 30.)

[181] H. Busnengo, *et al.*, *Chem. Phys. Lett.* **356**, 515 (2002). (Cited on page 27.)

[182] G. Darling, Z. Wang, S. Holloway, *Phys. Chem. Chem. Phys.* **2**, 911 (2000). (Cited on page 27.)

[183] B. Bransden, C. Joachain, *Physics of Atoms and Molecules*, Pearson Education (Prentice Hall, 2003). (Cited on page 28.)

[184] P. Schofield, *Comput. Phys. Commun.* **5**, 17 (1973). (Cited on page 29.)

[185] H. Nienhaus, *Surf. Sci. Rep.* **45**, 1 (2002). (Cited on page 30.)

[186] A. J. B. Robertson, *Int. J. Electron.* **51**, 607 (1981). (Cited on pages 30, 39, and 71.)

[187] M. Lindenblatt, E. Pehlke, *Phys. Rev. Lett.* **97**, 216101 (2006). (Cited on page 30.)

[188] N. Shenvi, S. Roy, J. C. Tully, *Science* **326**, 829 (2009). (Cited on page 30.)

[189] N. Shenvi, S. Roy, J. C. Tully, *J. Chem. Phys.* **130**, 174107 (2009). (Cited on page 30.)

[190] M. Timmer, P. Kratzer, *Phys. Rev. B* **79**, 165407 (2009). (Cited on page 30.)

[191] J. Meyer, K. Reuter, *New J. Phys.* **13**, 085010 (2011). (Cited on page 30.)

[192] M. Grotemeyer, E. Pehlke, *Phys. Rev. Lett.* **112**, 043201 (2014). (Cited on page 30.)

[193] P. Echenique, R. Nieminen, R. Ritchie, *Solid State Commun.* **37**, 779 (1981). (Cited on pages 30, 31, and 45.)

[194] B. Hellsing, M. Persson, *Phys. Scr.* **29**, 360 (1984). (Cited on page 30.)

[195] P. M. Echenique, R. M. Nieminen, J. C. Ashley, R. H. Ritchie, *Phys. Rev. A* **33**, 897 (1986). (Cited on page 30.)

[196] M. Head-Gordon, J. C. Tully, *J. Chem. Phys.* **103**, 10137 (1995). (Cited on page 30.)

[197] S. P. Rittmeyer, J. Meyer, J. I. Juaristi, K. Reuter, *Phys. Rev. Lett.* **115**, 046102 (2015). (Cited on page 30.)

[198] O. Bünermann, *et al.*, *Science* **350**, 1346 (2015). (Cited on page 30.)

[199] J. Juaristi, A. Arnau, P. Echenique, C. Auth, H. Winter, *Phys. Rev. Lett.* **82**, 1048 (1999). (Cited on page 30.)

[200] L. Bönig, K. Schönhammer, *Phys. Rev. B* **39**, 7413 (1989). (Cited on page 30.)

[201] K. Schönhammer, *Phys. Rev. B* **37**, 7735 (1988). (Cited on pages 30 and 31.)

[202] A. Salin, A. Arnau, P. Echenique, E. Zaremba, *Phys. Rev. B* **59**, 2537 (1999). (Cited on pages 30 and 31.)

[203] E. Zaremba, J. H. Rose, L. M. Sander, H. B. Shore, *J. Phys. F* **7**, 1763 (1977). (Cited on page 31.)

[204] R. D. Muiño, A. Salin, *Phys. Rev. B* **62**, 5207 (2000). (Cited on page 32.)

[205] M. Dohle, P. Saalfrank, *Surf. Sci.* **373**, 95 (1997). (Cited on page 32.)

[206] J. Manson, *Phys. Rev. B* **43**, 6924 (1991). (Cited on page 32.)

[207] S. A. Adelman, *J. Chem. Phys.* **71**, 4471 (1979). (Cited on pages 32 and 34.)

[208] M. Dohle, P. Saalfrank, T. Uzer, *J. Chem. Phys.* **108**, 4226 (1998). (Cited on page 32.)

[209] J. C. Polanyi, R. J. Wolf, *J. Chem. Phys.* **82**, 1555 (1985). (Cited on page 32.)

[210] H. Busnengo, M. Di Césare, W. Dong, A. Salin, *Phys. Rev. B* **72**, 125411 (2005). (Cited on page 34.)

[211] J. B. Keller, *Ann. Phys.* **4**, 180 (1958). (Cited on page 34.)

[212] W. H. Miller, *Science* **233**, 171 (1986). (Cited on page 34.)

[213] G. J. Kroes, E. Pijper, A. Salin, *J. Chem. Phys.* **127**, 164722 (2007). (Cited on page 37.)

[214] L. Bonnet, J. Rayez, *Chem. Phys. Lett.* **277**, 183 (1997). (Cited on page 38.)

[215] V. Krishna, J. C. Tully, *J. Chem. Phys.* **125**, 054706 (2006). (Cited on pages 39 and 71.)

[216] A. M. Wodtke, *Chem. Soc. Rev.* **45**, 3641 (2016). (Cited on page 39.)

[217] S. Shimokawa, A. Namiki, M. N. Gamo, T. Ando, *J. Chem. Phys.* **113**, 6916 (2000). (Cited on page 39.)

[218] M. Rutigliano, M. Cacciatore, *Chem. Phys. Chem.* **9**, 171 (2008). (Cited on page 39.)

[219] T. Kammler, J. Küppers, *J. Chem. Phys.* **111**, 8115 (1999). (Cited on page 39.)

[220] B. F. Hansen, G. D. Billing, *Surf. Sci.* **373**, L333 (1997). (Cited on page 39.)

[221] M. Cacciatore, E. Christoffersen, M. Rutigliano, *J. Chem. Phys. A* **108**, 8810 (2004). (Cited on page 39.)

[222] H. F. Busnengo, A. E. Martínez, *J. Phys. Chem. C* **112**, 5579 (2008). (Cited on pages 40, 79, and 84.)

[223] H. J. Ernst, E. Hulpke, J. P. Toennies, *Phys. Rev. B* **46**, 16081 (1992). (Cited on page 40.)

[224] S. Titmuss, A. Wander, D. A. King, *Chem. Rev.* **96**, 1291 (1996). PMID: 11848790. (Cited on page 40.)

[225] M. Balden, S. Lehwald, H. Ibach, *Phys. Rev. B* **53**, 7479 (1996). (Cited on pages 41 and 72.)

[226] M. Balden, S. Lehwald, H. Ibach, D. L. Mills, *Phys. Rev. Lett.* **73**, 854 (1994). (Cited on pages 41 and 72.)

[227] M. R. Barnes, R. F. Willis, *Phys. Rev. Lett.* **41**, 1729 (1978). (Cited on pages 41 and 85.)

[228] W. Ho, R. Willis, E. Plummer, *Phys. Rev. B* **21**, 4202 (1980). (Cited on pages 41 and 85.)

[229] W. Ho, R. F. Willis, E. W. Plummer, *Phys. Rev. Lett.* **40**, 1463 (1978). (Cited on pages 41 and 85.)

[230] M. C. Wheeler, C. T. Reeves, D. C. Seets, C. B. Mullins, *J. Chem. Phys.* **108**, 3057 (1998). (Cited on page 55.)

[231] E. K. Rideal, *Math. Proc. Cambridge* (Cambridge Univ Press, 1939), vol. 35, pp. 130–132. (Cited on page 55.)

[232] D. D. Eley, *P. Roy. Soc. A-Math. Phy.* (The Royal Society, 1941), vol. 178, pp. 452–464. (Cited on page 55.)

[233] C. Schermann, F. Pichou, M. Landau, I. Čadež, R. I. Hall, *J. Chem. Phys.* **101**, 8152 (1994). (Cited on pages 55, 79, 103, and 104.)

[234] B. Jackson, M. Persson, *J. Chem. Phys.* **96**, 2378 (1992). (Cited on page 55.)

[235] J. Juaristi, *et al.*, *Catal. Today* **244**, 115 (2015). (Cited on pages 62 and 102.)

[236] C. T. Rettner, D. J. Auerbach, *Surf. Sci.* **357**, 602 (1996). (Cited on page 63.)

[237] T. Zaharia, A. W. Kleyn, M. A. Gleeson, *Phys. Rev. Lett.* **113**, 053201 (2014). (Cited on page 63.)

[238] V. V. Gonchar, O. V. Kanash, A. G. Naumovets, A. G. Fedorus, *JETP Lett.* **28**, 330 (1978). (Cited on page 72.)

[239] V. V. Gonchar, Y. M. Kagan, O. V. Kanash, A. G. Naumovets, A. G. Fedorus, *Sov. Phys. JETP* **57**, 142 (1983). (Cited on page 72.)

[240] Y. Yamada, K. H. Rieder, W. Theis, *Phys. Rev. Lett.* **99**, 196105 (2007). (Cited on pages 79, 103, and 104.)

[241] T. Biederer, T. Kammler, J. Küppers, *Chem. Phys. Lett.* **286**, 15 (1998). (Cited on page 83.)

[242] A. Perrier, L. Bonnet, D. Liotard, J.-C. Rayez, *Surf. Sci.* **581**, 189 (2005). (Cited on page 84.)

[243] J. P. Perdew, P. Ziesche, H. Eschrig, *Electronic structure of solids*, vol. 11 (Akademie Verlag, Berlin, 1991). (Cited on page 84.)

[244] J. P. Perdew, Y. Wang, *Phys. Rev. B* **46**, 12947 (1992). (Cited on page 84.)

[245] G. Kresse, J. Hafner, *Phys. Rev. B* **47**, 558 (1993). (Cited on page 84.)

[246] G. Kresse, J. Hafner, *Phys. Rev. B* **49**, 14251 (1994). (Cited on page 84.)

[247] G. Kresse, J. Hafner, *J. Phys. Condens. Mat.* **6**, 8245 (1994). (Cited on page 84.)

[248] G. Kresse, J. Furthmüller, *Comut. Mater. Sci.* **6**, 15 (1996). (Cited on page 84.)

[249] G. Kresse, J. Furthmüller, *Phys. Rev. B* **54**, 11169 (1996). (Cited on page 84.)

[250] D. Vanderbilt, *Phys. Rev. B* **41**, 7892 (1990). (Cited on page 84.)

[251] K. C., *Introduction to Solid State Physics* (Wiley, 1953). (Cited on page 84.)

[252] H. Busnengo, A. Salin, W. Dong, *J. Chem. Phys.* **112**, 7641 (2000). (Cited on page 85.)

[253] R. A. Olsen, *et al.*, *J. Chem. Phys.* **116**, 3841 (2002). (Cited on page 85.)

[254] H. Froitzheim, H. Ibach, S. Lehwald, *Phys. Rev. Lett.* **36**, 1549 (1976). (Cited on page 85.)

[255] U. Jayasooriya, *et al.*, *Surf. Sci.* **93**, 526 (1980). (Cited on page 85.)

[256] H.-J. Herlt, E. Bauer, *Surf. Sci.* **175**, 336 (1986). (Cited on page 85.)

[257] P. Estrup, J. Anderson, *J. Chem. Phys.* **45**, 2254 (1966). (Cited on page 85.)

[258] R. Biswas, D. Hamann, *Phys. Rev. Lett.* **56**, 2291 (1986). (Cited on page 85.)

[259] L. Lou, D. Langreth, P. Nordlander, *Surf. Sci.* **234**, 412 (1990). (Cited on page 85.)

[260] J. Woods, J. Erskine, *J. Vac. Sci. Technol. A* **4**, 1414 (1986). (Cited on page 85.)

[261] M. Pavanello, *et al.*, *J. Phys. Chem. Lett.* **4**, 3735 (2013). (Cited on page 102.)

[262] G.-J. Kroes, M. Pavanello, M. Blanco-Rey, M. Alducin, D. J. Auerbach, *J. Chem. Phys.* **141**, 054705 (2014). (Cited on page 102.)